Numéro d'ordre :

Université des Sciences et Technologies de Lille
Laboratoire de Mécanique de Lille (UMR CNRS 8107)
Ecole Doctorale Sciences Pour l'Ingénieur - Université Lille Nord de France

THESE

Pour obtenir le grade de

Docteur de l'Université Lille 1 Sciences et Technologies

Discipline : Mécanique, Energétique, Matériaux

Présentée et soutenue publiquement

par

Hemin ABDULHAMEED

20 Juillet 2015

Réponse viscoélastique-viscoplastique en grandes déformations du polyéthylène : Observations expérimentales, modélisation constitutive et simulation

Large-strain viscoelastic-viscoplastic response of polyethylene: Experimental observations, constitutive modeling and simulation

Jury

Z. AZARI	Professeur	Université de Metz	Rapporteur
N. AIT-HOCINE	Professeur	INSA Centre Val de Loire	Rapporteur
R. ESTEVEZ	Professeur	Université de Grenoble	Examinateur
G. AYOUB	Maître de Conférences	Texas A&M University at Qatar	Examinateur
T. MESSAGER	Maître de Conférences	Université Lille 1	Codirecteur de thèse
F. ZAIRI	Professeur	Université Lille 1	Codirecteur de thèse
M. NAIT-ABDELAZIZ	Professeur	Université Lille 1	Directeur de thèse

Table of contents

General introduction

This PhD dissertation focuses on the large-strain viscoelastic-viscoplastic response of polyethylene by combining experimental observations, constitutive modeling and simulations.

Polyethylene-based materials are used in a wide range of engineering applications, especially in the aerospace, automotive and biomechanical industries. Polyethylene materials are semi-crystalline systems consisting of both amorphous and crystalline phases interacting in a rather complex manner. When the amorphous phase is in the rubbery state, the mechanical behavior is strongly dependent on the crystal fraction, therefore leading to essentially thermoplastic or elastomeric responses. Above the glass transition temperature, polyethylene materials can behave like an elastomer or a stiff polymer according to the crystal content. For a reliable design of such polymeric materials, it is of prime importance to develop a unified constitutive modeling able to capture the transition from thermoplastic-like to elastomeric-like mechanical response, as the crystal content changes.

This PhD dissertation is divided into three chapters.

In chapter one, experimental observations on large-strain time-dependence mechanical response of polyethylene are reported. The aim is to provide a fruitful database on the mechanical behavior under large deformation of different polyethylene materials, covering a large spectrum of the crystallinity, in order to elaborate a constitutive modeling able to capture the general trends.

Chapter two deals with the formulation and identification of a large-strain viscoelastic-viscoplastic constitutive model able to capture the polyethylene response. In a first approach, the polyethylene materials are considered as homogeneous media; for each crystal content, the polyethylene material is thus considered as a new material. In a second approach, the polyethylene materials are seen as two-phase composites and the effective contribution of the crystalline and amorphous phases to the overall mechanical response is integrated in the intermolecular resistance. In the aim to minimize the number of model parameters, an extended version of the constitutive model is then proposed by integrating the crystal effects in both intermolecular and network resistances. In order to identify the model parameters, an analytical deterministic scheme and a numerical tool, based on an optimization scheme using a genetic algorithm, are developed.

Chapter three is dedicated to the model implementation into a finite element code and to applications. The simulations focus on monolitic specimens in polyethylene and multi-layered polyethylene specimens at different cystal fractions.

General conclusions are presented at the end of the document.

Chapter one

EXPERIMENTAL OBSERVATIONS ON LARGE-STRAIN TIME DEPENDENT MECHANICAL RESPONSE OF POLYETHYLENE

This chapter aims to experimentally investigate the crystal content effects on the large-strain time-dependent mechanical response of polyethylene at room temperature (RT). A large spectrum of the crystallinity, implying thermoplastic-like and elasomeric-like mechanical responses, is considered. Observations are reported for monotonic loading, cyclic loading-unloading and stress relaxation.This chapter is organized as follows: Part I presentmaterials and methods. The results are presented and discussed in part II. Concluding remarks are given in part III.

I. Materials and methods

I.1. Materials

Three semi-crystalline polyethylene materials are considered. They consist of a Ziegler-Natta high density ethylene-hexene copolymer (HDPE) from Total Petrochemicals, a linear low density ethylene-octene copolymer (LDPE), and an ultra low density ethylene-octene copolymer (ULDPE) from DOW Chemicals, both issued from metallocene catalysis.

Isotropic polyethylene plates were obtained by compression molding at 180°C into 0.5 and 1 mm thick sheets and slowly cooled to RT in order to avoid residual thermal stresses generated during cooling.

The molecular and physical characteristics of the three polyethylene materials, provided by the manufacturers, are given in **Table 1.1.** The co-unit concentration ξ is the major factor that controls the crystallinity, and thereby the density.

Materials	M_n (kDa)	M_w (kDa)	ξ (mole%) †	ρ (g/cm^3) *
ULDPE	75	150	12 (60)	0.870
LDPE	50	104	5.0 (25)	0.902
HDPE	14	174	0.1 (0.5)	0.959

Table 1.1. Molecular characteristics and density of polyethylene materials: number-average molar weight, M_n; weight-average molar weight, M_w; counit content, ξ; density, ρ.
† hexene for HDPE; octene for LDPE and ULDPE; between brackets is the SCB/1000 C atoms in the backbone.
* density of compression-moulded sheets.

Fig. 1.1 presents the differential scanning calorimetry (DSC) heating traces of the three polyethylene materials[1]. The endotherm of the HDPE materiel is typical of a high crystallinity polymer. The very broad melting endotherm, displayed by the LDPE and ULDPE materials, is indicative of a non-uniform chemical composition distribution. The extent of the melting endotherm far below RT for the ULDPE copolymer is relevant to the presence of highly co-unit rich chains that crystallize upon cooling below RT.

[1]DSC measurements were achieved on a Q100-apparatus from TA Instruments at a scanning rate of 10°C/min from -50°C to 180°C under nitrogen atmosphere. The temperature and heat flow scale were calibrated using high purity indium and zinc samples according to standard procedures at the same heating rate as for materials analysis. Samples of about 8 mg inserted into aluminium pans were submitted to heating and cooling cycles, holding the samples for 3 min at each temperature limit. At least three different samples were analyzed. The first heating scan was aimed at erasing the thermo-mechanical history. The second heating scan was recorded for further analysis.

The crystal weight fraction χ_{cw} was calculated by normalizing the experimental melting heat ΔH_f by the melting heat ΔH_f^0 of a perfect PE orthorhombic crystal[2]:

$$\chi_{cw} = \frac{\Delta H_f}{\Delta H_f^0} \tag{1.1}$$

Note that ΔH_f^0 is temperature-dependent and since the T_f values are quite different for the three polyethylene materials, the ΔH_f^0 decrease with the melting temperature decrease is taken into account (Wunderlich, 1980).

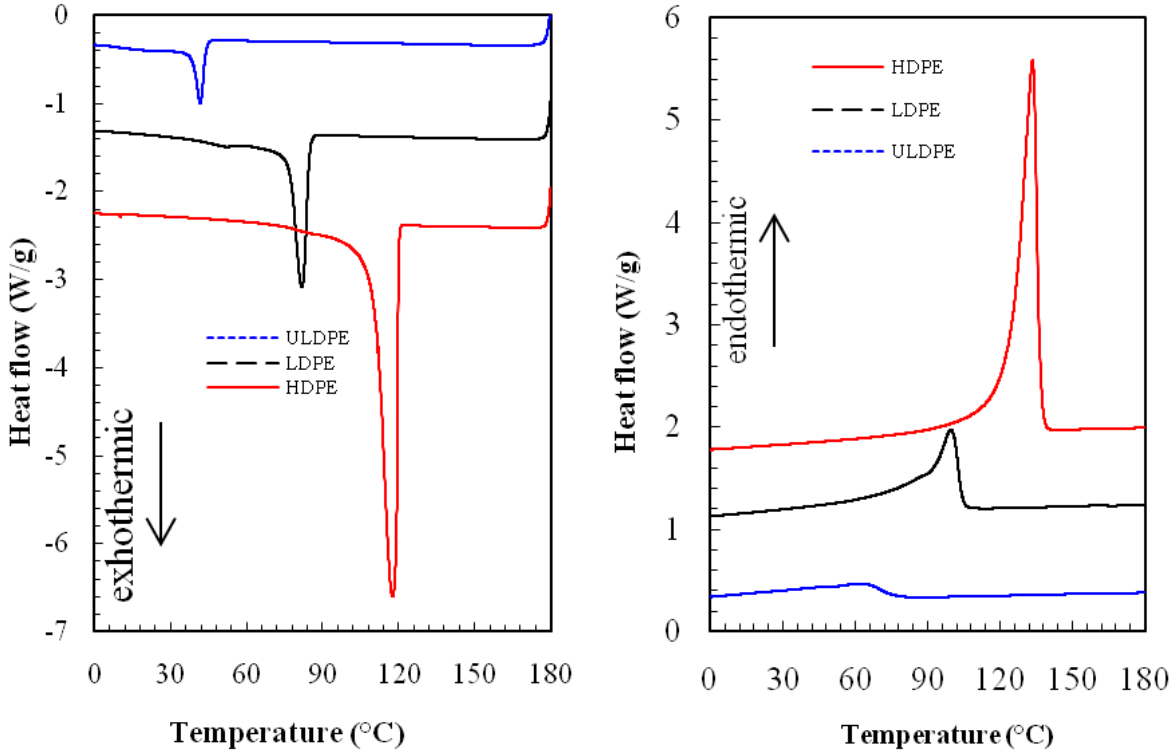

Fig. 1.1. DSC traces of exhothermic and endothermic for the polyethylene materials.

The thermal characteristics of the three polyethylene materials, determined by DSC analysis, are reported in **Table 1.2**.

[2]The overall crystal volume fraction χ_{cv}, a direct input data of the micromechanical model, is calculated by the following formula: $\chi_{cv} = \rho/\rho_c \chi_{cw}$, in which ρ is the density of the whole material and ρ_c = 1.00 g/cm³ is the density of the crystalline phas

Materials	T_f (°C)	ΔH_f^0 (J/g)	χ_{cw} (%)
ULDPE	60.9 ± 0.1	~ 290.3	17.4 ± 0.3
LDPE	99.8 ± 0.5	~ 299.3	33.3 ± 0.8
HDPE	133.5 ± 0.2	~ 296.5	75.5 ± 0.8

Table 1.2. Thermal characteristics of PE materials:
T_f : Melting temperature taken at the extremum of the melting endotherm.
ΔH_f^0 : Melting heat of a perfect PE orthorhombic crystal.
χ_{cw} : Crystal weight fraction at RT.

Atomic force microscopy images are shown in **Fig. 1.2** for the three polyethylene materials[3]. The crystallinity affects significantly the morphology in terms of shape, size and distribution of crystal lamellae. The ULDPE morphology is not so well defined and displays fussy crystallites akin to fringed micelles. The crystal lamellae are obviously presented in the case of HDPE and LDPE materials. The distribution seems isotropic in both morphologies, but a difference in the lamellae size.

I.2. Methods

Dynamic mechanical analysis (DMA) in tensile mode was carried out for the three polyethylene materials using a RSA3 apparatus (TA Instruments, Wilmington DE, USA). Parallelepipedic samples (10 mm in gauge length, 4 mm wide and 0.5 mm thick) were cut from compression-molded plates. Measurements were performed with dynamic strain amplitude of 0.1 %, the static stress being 10% greater than the dynamic stress amplitude in order to prevent buckling.

Large-strain mechanical measurements were conducted at RT on an electromechanical Instron-5800 testing machine equipped with a video-extensometer

[3]AFM characterizations were performed at RT on a Dimension 3100 apparatus from Digital Instruments operated in Tapping Mode. The set-point amplitude ratio was $0.75 < r_{sp} < 0.85$ in order to control the penetration depth of the sensor tip with regard to the size of the crystalline and amorphous layers and thus optimize the phase contrast. The film samples were prepared by slow cooling from the melt with free upper surface in order to generate a natural crystallization-induced morphology. Due to the sample preparation conditions, phase images turned out to be more relevant than height images for revealing morphological features from the surface.

enabling to record the local strains. Dumbbell-shaped specimens were cut from 1 mm-thick plates for the nominal tests. For the video-extensometer measurements and in order to localize the deformation in the central part of the specimen, the specimens with a curvature shape in the gauge section, were cut from the 1 mm-thick plates (120 mm curvature radius, 28 mm long and 8 mm wide).

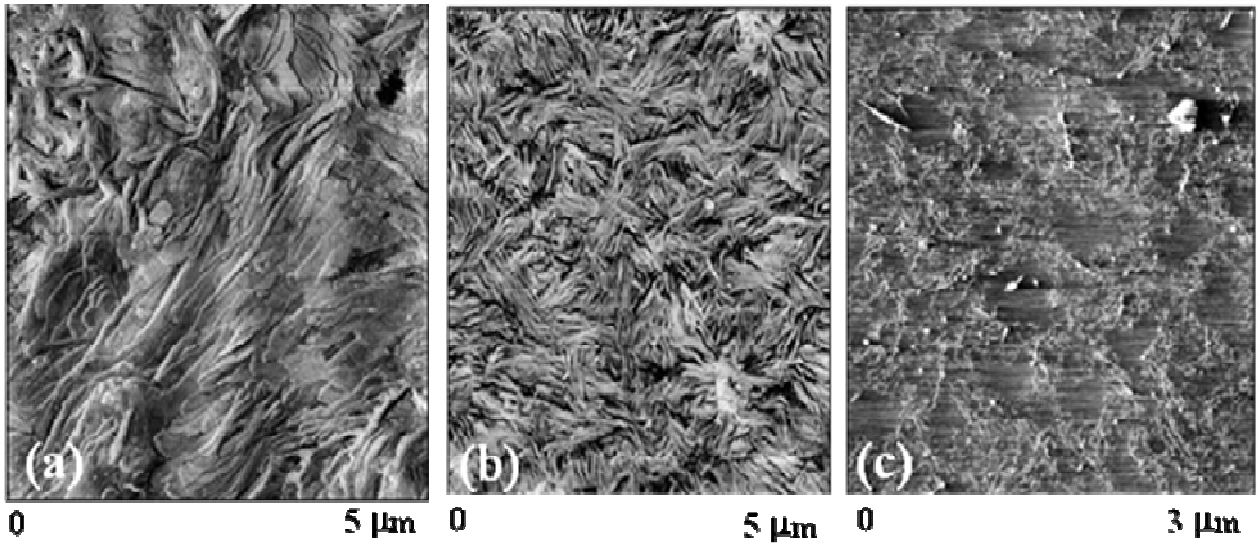

Fig. 1.2. AFM images in phase contrast of the three polyethylene materials: (a) HDPE, (b) LDPE and (c) ULDPE.

II. Results

II.1. DMA results

The storage modulus E' is plotted as a function of frequency at RT in **Fig. 1.3-a** and as a function of temperature in **Fig. 1.3-b** for the three polyethylene materials. The loss factor $\tan\delta(\theta)$ is plotted in **Fig. 1.4.** The analysis of the $E'(\theta)$ and $\tan\delta(\theta)$ plots allow to observe the three typical relaxations of polyethylene. The γ relaxation that clearly appears in the temperature range (-140 to -110°C) of the $\tan\delta(\theta)$ plots is very similar for the three polyethylene materials. Regarding the β relaxation in the temperature range (-60 to -40°C), the marked $E'(\theta)$ drop clearly reveals a cooperative process that can be assigned to the main relaxation in the amorphous

phase (Hoffman et al., 1966). The β relaxation amplitude is important in the case of the ULDPE, noticeably reduced in the LDPE and almost unseen for the HDPE. A possible reason in the latter case is that the continuity of the largely predominant crystalline phase makes the minor amorphous phase unable to express its damping capabilities due to too low stress transfer from the matrix in which it is embedded. The α relaxation assigned to the activation of molecular motions in the crystal, probably combined with a mobility of the chain folds, appears over a wide temperature range beyond 20°C. If crystallinity is a major contributor to the amplitude of the α relaxation, the prime factor to its temperature dependence is the crystal thickness (Popli et al., 1984), which intervenes in the framework of the chain kink defect migration (Boyd, 1985). Worth noticing is the fact that the ULDPE copolymer does not display any visible signs of damping in this temperature range. An explanation analogous to the one regarding the β relaxation of the HDPE copolymer can be proposed: the dispersed crystal phase is unable to express its damping capabilities due to deficient stress transfer from the rubber matrix in which it is embedded (Ayoub et al., 2011).

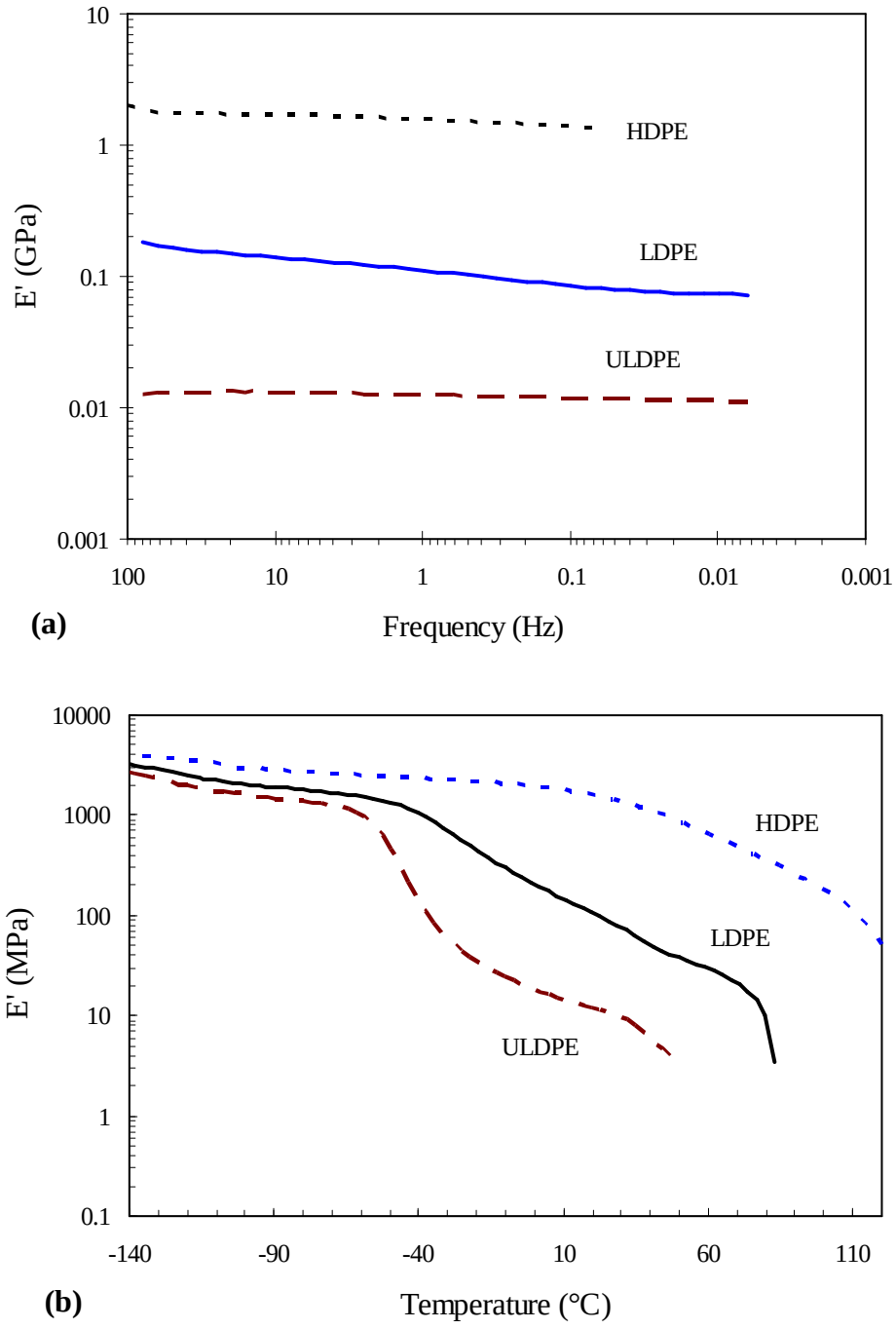

Fig. 1.3. Storage modulus *E′* as a function of: (a) frequency at RT and (b) temperature.

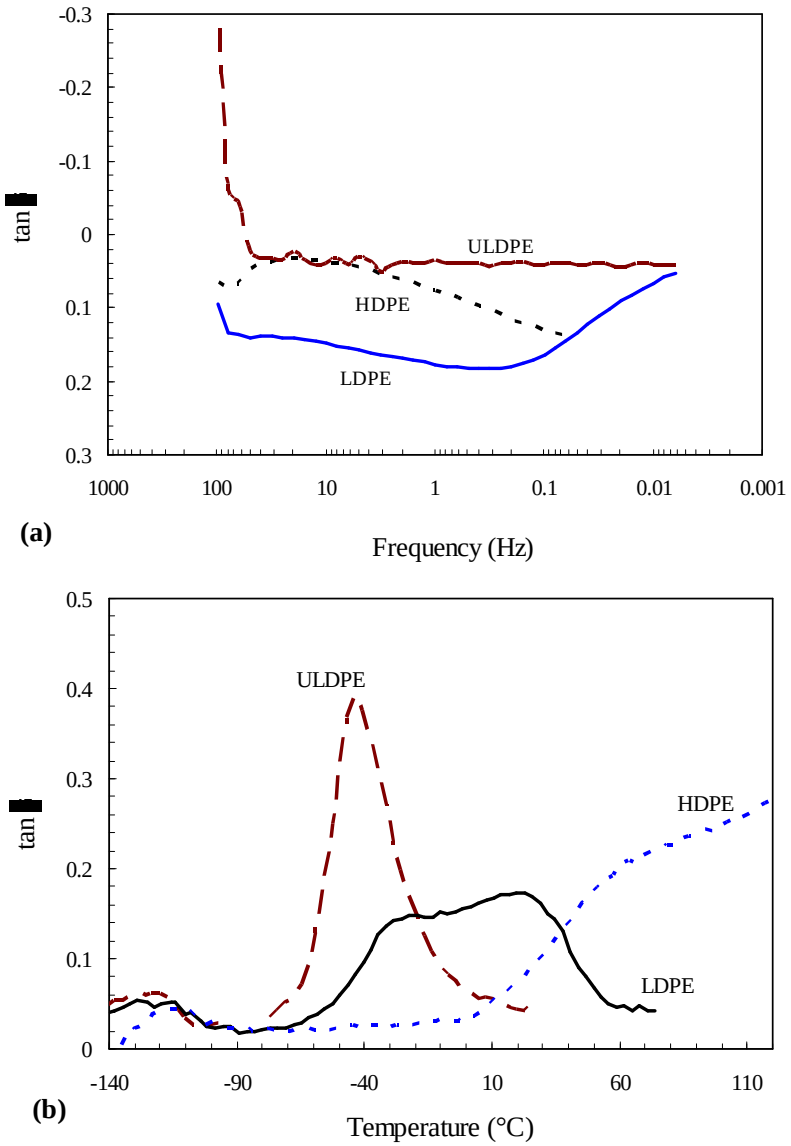

Fig. 1.4. Loss factor tanδ as a function of: (a) frequency at RT and (b) temperature.

II.2. Nominal stress-strain relationship

The nominal stress-strain relationship is presented in **Fig. 1.5** for the three polyethylene materials stretched under large-strain deformation at an initial strain rate of 0.001 s^{-1}. Under the crystal content effect, a wide range of mechanical response is highlighted: from elastomeric-like behavior for ULDPE, with no clear yield point, to stiff thermoplastic-like behavior for HDPE, with strong presence of yield point and post-yield strain-softening.

Pictures, taken at different stages of deformation are reported in **Fig. 1.5**. The LDPE and ULDPE materials exhibit stable plastic deformation, while unstable plastic deformation, manifested by a neck, is noticed in the HDPE material. The latter is characterized by a rapid decrease in specimen cross-section resulting in the observed strain-softening in the HDPE stress-strain curve. The plateau corresponds to the neck stabilization and propagation along its shoulders.

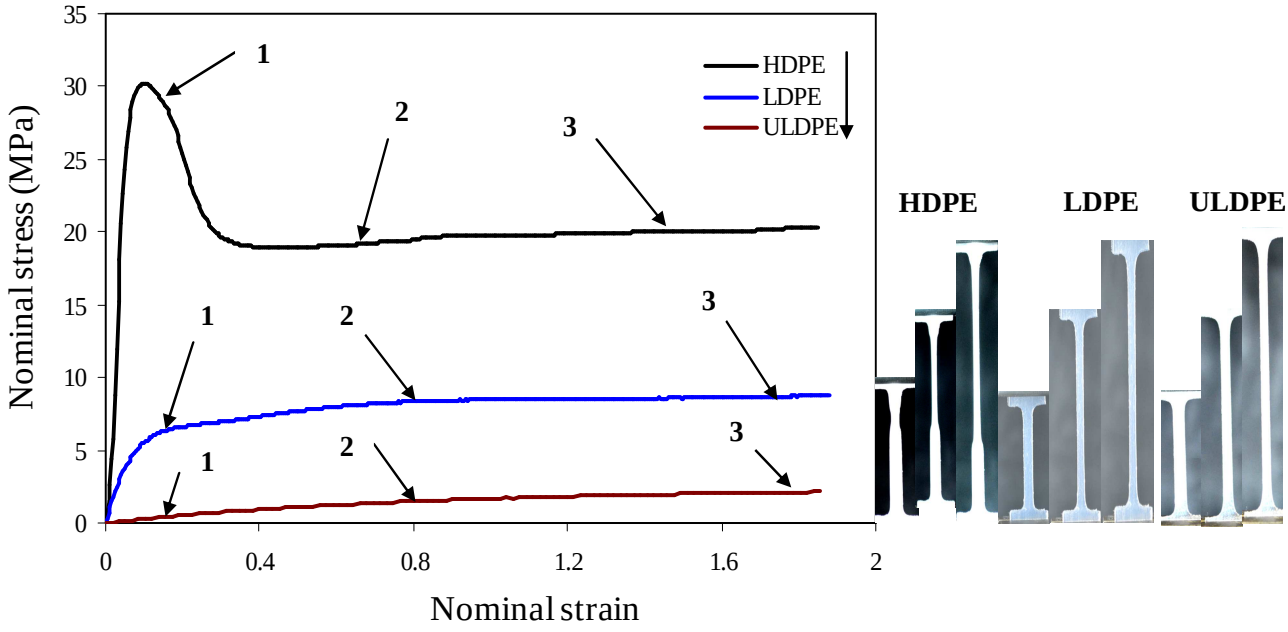

Fig. 1.5. Nominal stress-strain curves of the three polyethylene materials stretched at an initial true strain rate of 0.001 s^{-1}.

II.3. True stress-strain relationship

The three polyethylene materials have been stretched at different local true axial strain rates and the results, in terms of true stress-strain curves[4], are presented in **Fig. 1.6**. Whatever the polyethylene material, the true stress-strain relationship is highly nonlinear, strongly depends on crystal content.

The HDPE material, highest crystal content among the examined polyethylene materials, shows a significant initial stiffness and a clear frontier of elastic behavior in comparison with the other two materials. Beyond the elastic limit, HDPE flows at a

[4]The true (Cauchy) axial stress was calculated by dividing the value of the force, measured with a standard load cell, with the actual sample cross-section measured by the video-extensometer.

relatively constant stress followed by small strain hardening which increases dramatically at large elongations. The disappearance of the strain-softening observed in the HDPE nominal response of **Fig. 1.6** is a consequence of the maintaining constant the local strain rate in the gauge section of the specimen during the deformation. The dramatic strain hardening is due to chains that are impeded to align in crystallographic blocks or that try to align in the direction of the applied load. The ULDPE material, lowest crystal content among the examined polyethylene materials, shows an elastomeric material behavior with no significant initial stiffness, i.e. ULDPE undergoes large deformation when subjected to small loads. Note that a dramatic strain hardening is not observed in ULDPE. The LDPE material has no intermediate behavior between ULDPE and HDPE. For small deformations, it behaves more or less like ULDPE; however, it has higher elastic limit and initial stiffness than ULDPE. At large deformations, stress increases rapidly until it reaches the same level of HDPE stress. This behavior evidences that the morphology evolution of LDPE is not proportionally intermediate of the morphology evolution between HDPE and ULDPE.

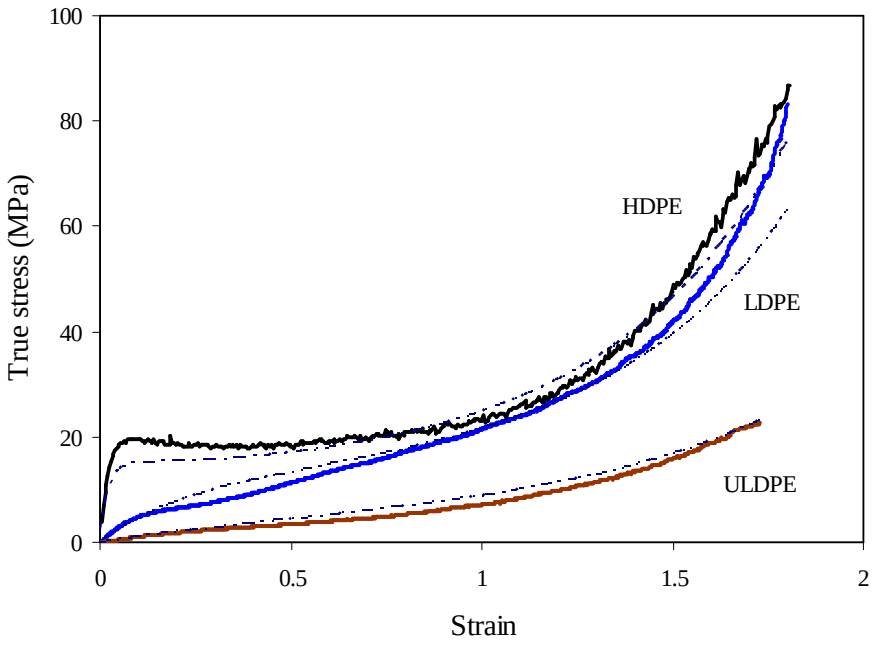

Fig. 1.6. True stress-strain curves of the three polyethylene materials stretched at a true strain rate of $0.001s^{-1}$; the dot lines correspond to the G'Sell and Marques-Lucero (1993) analytical relationship.

II.4. Strain rate effect on the stress-strain relationship

Fig. 1.7 illustrates the strong dependence of HDPE mechanical responce on strain rate. Besides, it can be observed that initial stiffness, elastic limit, viscoplastic flow and strain hardening are influenced by the rate of deformation. Note that, in contrast to HDPE, both LDPE and ULDPE seem to be less sensitive to strain rate. In order to illustrate the effect of strain rate on true stress at different levels of deformation for the three polyethylene materials, the strain rate sensitivity has been examined over two ranges of deformation: elastic limit and beyond elastic limit.

At the elastic limit deformation range, the effect of strain rate, regarding the evolution of the yield point, was examined. In **Fig. 1.8**, the yield stress as a function of the strain rate is plotted for each polyethylene material. It can be noticed that the yield stress increases with the strain rate. Besides, the strain rate sensitivity coefficient is the exponent of the fitting equation and, evidently, higher values are related with higher strain rate dependence. The results clearly demonstrate the rate dependent mechanical behavior of the studied polyethylene materials. It can also be noticed that the yield stress and the strain rate sensitivity coefficient increase with increasing crystal content.

Fig. 1.9 shows the influence of strain rate on true stress at different strain levels. The results reveal the rate dependent mechanical behavior of polyethylene materials, as mentioned above. It is evident that the strain rate at different elongation levels is strongly influenced by the crystal content.

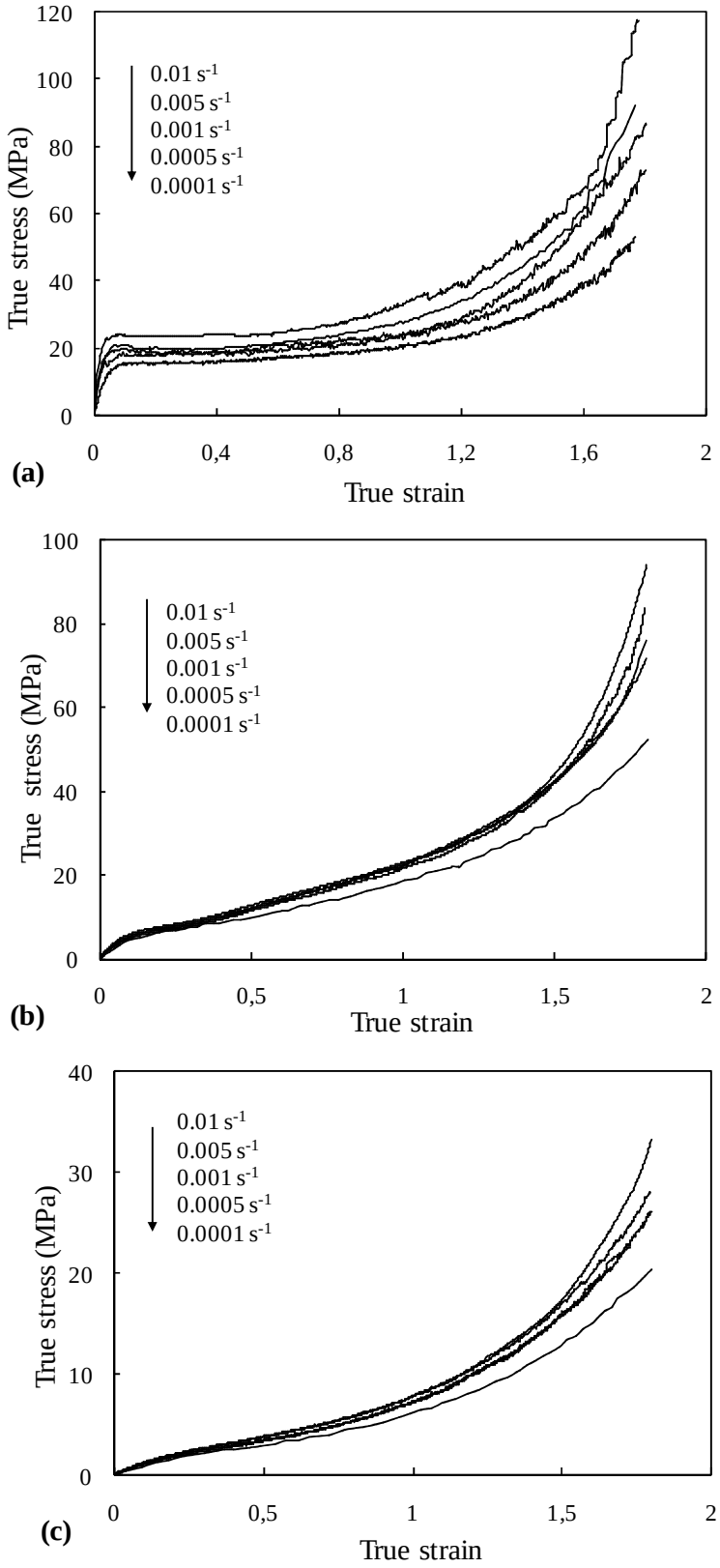

Fig. 1.7. Experimental true stress-strain curves at different true stain rates: (a) HDPE, (b) LDPE, (c) ULDPE.

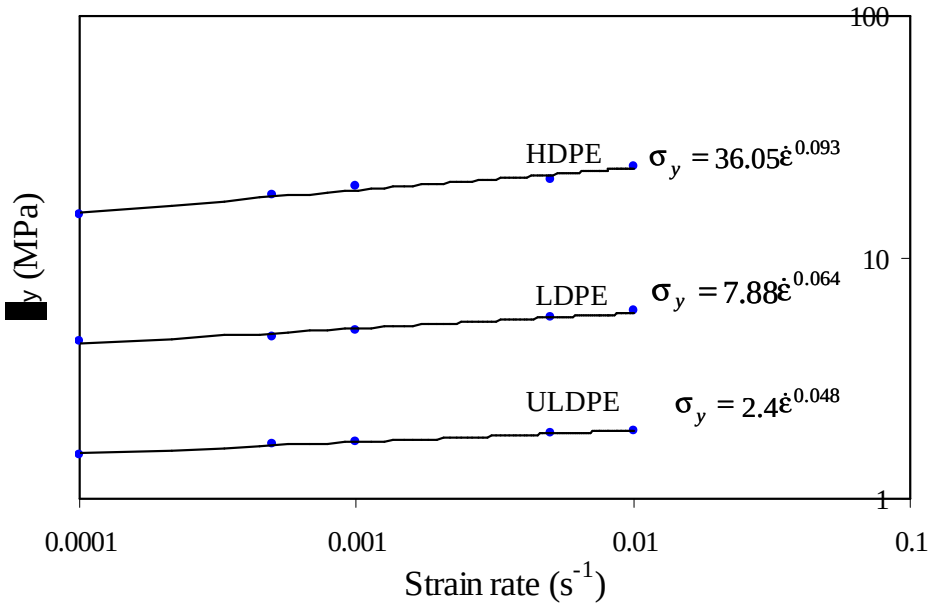

Fig. 1.8. Effect of strain rate on yield stress for the three polyethylene materials.

Table 1.3 presents the values of the strain rate sensitivity coefficient for different polyethylene materials at different strain levels. The average values reveal that the evolution of this coefficient is not monotonic with crystal content.

Strain	HDPE	LDPE	ULDPE
0.4	0.077	0.045	0.049
0.8	0.074	0.046	0.049
1.2	0.106	0.042	0.047
1.6	0.123	0.058	0.067
Average	0.095	0.047	0.053

Table 1.3. Strain rate sensitivity coefficient for the three polyethylene materials at different strain levels.

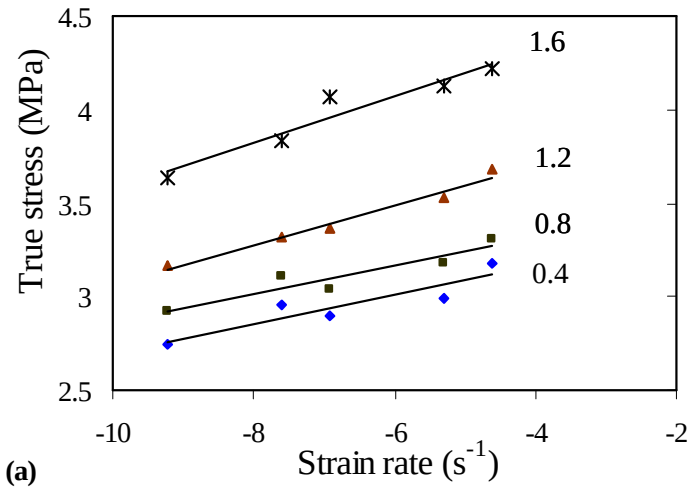

(a)

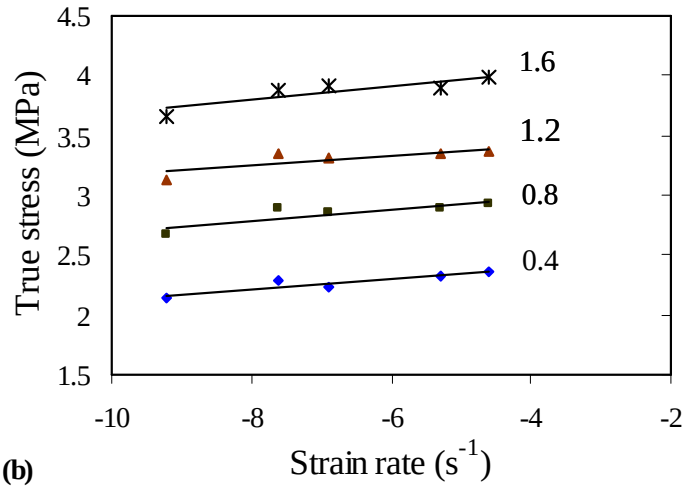

(b)

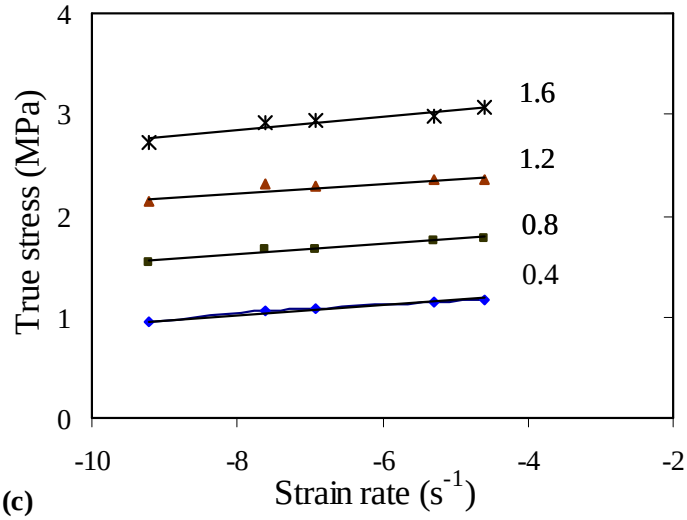

(c)

Fig. 1.10. Effect of strain rate on stress at different strain levels: (a) HDPE, (b) LDPE, (c) ULDPE.

The basic mathematical relationship, introduced by G'Sell and Marques-Lucero (1993), is employed to reproduce the true stress-strain response of the three polyethylene materials. The equation is given by:

$$\sigma = \mathrm{K}_f Y(\varepsilon) \exp(H\varepsilon^2) \left[\frac{\dot{\varepsilon}}{\dot{\varepsilon}_e}\right]^{m_a} \tag{1.2}$$

where K_f is a scaling factor, $Y(\varepsilon)$ is a yield transient function, H is the hardening coefficient, m_a is the average strain rate sensitivity coefficient, $\dot{\varepsilon}$ is the true strain rate and $\dot{\varepsilon}_o$ is an initial strain rate conventionally fixed at 1 s^{-1}. By neglecting strain softening effects, the $Y(\varepsilon)$ parameter can be written as:

$$Y(\varepsilon) = \left[1 - \exp(w\varepsilon)\right] \tag{1.3}$$

where w is a fitting coefficient calculated from the expression:

$$2H\varepsilon + w + 1 = \exp(w\varepsilon) \tag{1.4}$$

The above mathematical expressions are able to reproduce in a satisfactory extent the tensile stress-strain behavior of the three polyethylene materials as shown in **Fig. 1.7**. The identified coefficients of the G'Sell and Marques-Lucero (1993) model are reported in **Table 1.4** and the hardening coefficients involve according to the crystal content as follows:

$$\begin{aligned} \mathrm{K}_f &= 10.8 \ln\left(\chi_{cv}\right) + 32.4 \\ H &= 0.074 \ln\left(\chi_{cv}\right) + 0.53 \\ w &= 0.54 \exp\left(6.3\chi_{cv}\right) \end{aligned} \tag{1.6}$$

	K_f (MPa)	H	w	m
HDPE	29	0.5	50	0.095
LDPE	19	0.47	4	0.047
ULDPE	12	0.38	1.3	0.053

Table 1.4. G'Sell and Marques-Lucero (1993) model coefficients for the three polyethylene materials.

II.5. Cyclic stress-strain relationship

In this section, the mechanical behavior of the three polyethylene materials under cyclic loading was examined. The experimental protocol involved cyclic tests performed at three different levels of local strain at a constant true strain rate of $0.001s^{-1}$. After reaching a specific level of local strain, the specimen was completely unloaded and then reloaded n times to the same level of strain. Note that the loading-unloading condition was performed at the same constant true strain rate. Cyclic tests were achieved RT and performed, each time, on a new specimen. Results have shown that the polyethylene materials are time-dependent. Furthermore, under cyclic loading the materials have exhibited a continuous degradation of the mechanical properties with a rate of degradation dependent on the maximum encountered strain and on the crystal content.

The mechanical response of the three polyethylene materials under cyclic loading are presented in **Fig. 1.10**. Under cyclic loading, the mechanical behavior of the three polyethylene materials exhibits three specific features: (i) nonlinear response during unloading with the appearance of hysteresis during reloading, (ii) continuous strain-softening when cycling at a given maximum strain, (iii) permanent deformation appearing at the zero stress state evolving with cycling.

On the other hand, it can be observed that the evolution of the dissipated energy (the hysteresis area), the maximum stress at a given strain and the residual deformation are dependent on both the maximum strain and the crystal content. In what follows, a quantitative estimation of these evolutions is discussed.

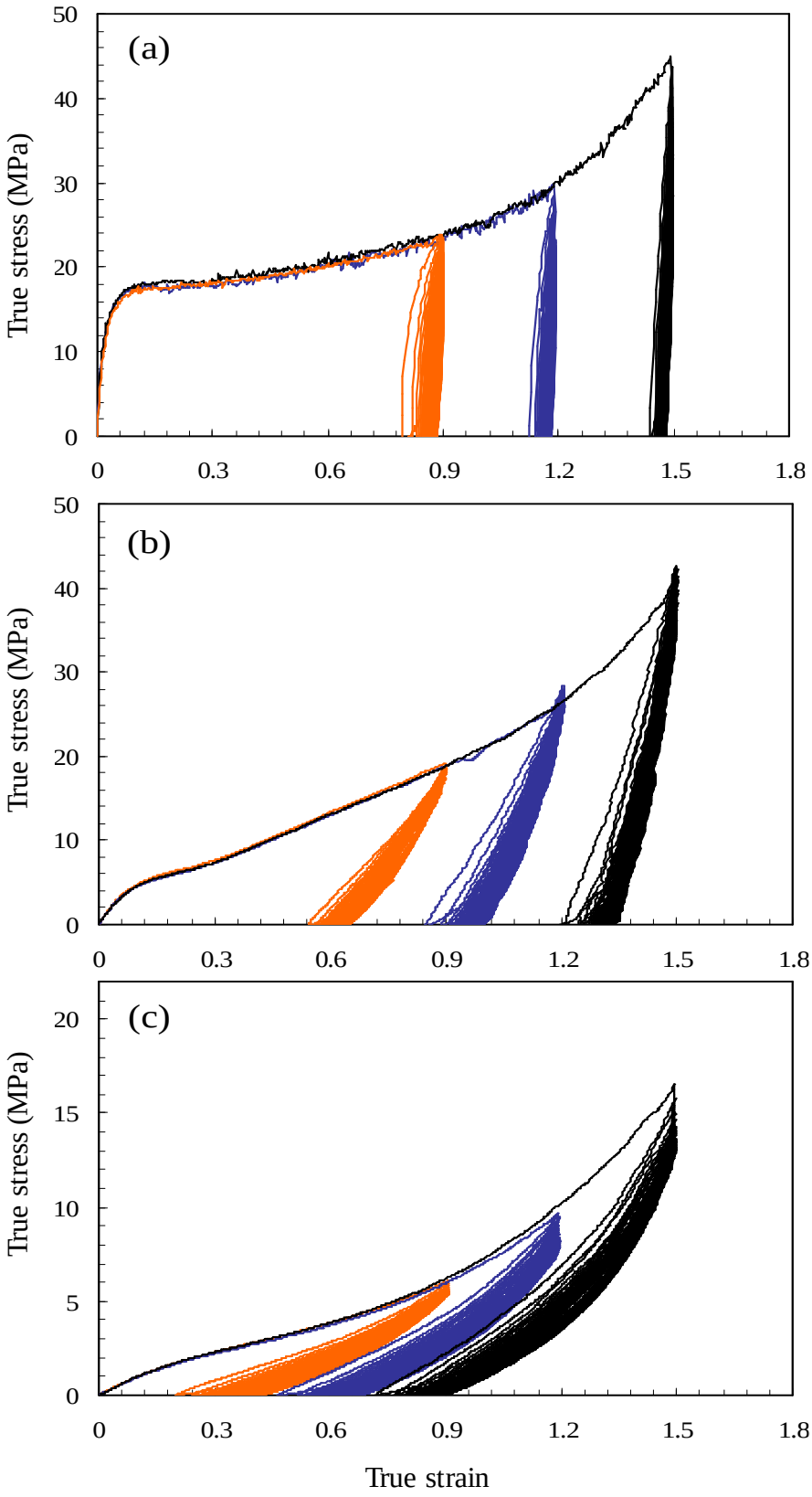

Fig. 2.10. Experimental cyclic true stress-strain curves: (a) HDPE, (b) LDPE, (c) ULDPE.

II.5.1. Dissipated energy vs. cycle number

The dissipated energy was estimated at every cycle for each of the three polyethylene materials subjected to uniaxial cyclic loading at different maximum strains. The dissipated energy was then normalized regarding the value at the first cycle of each test. The evolution of the normalized dissipated energy as a function of the number of cycles is plotted in **Fig. 1.11**. As a general observation, it is shown that the dissipated energy decreases with increasing cycle number until it reaches a steady state. The rate, at which the dissipated energy decreases, depends on both the maximum strain and the crystal content. It can be observed that increasing the maximum strain contributes to increase the rate at which the dissipated energy decreases. Furthermore, increasing the crystal content leads to accelerate the rate at which the dissipated energy decreases.

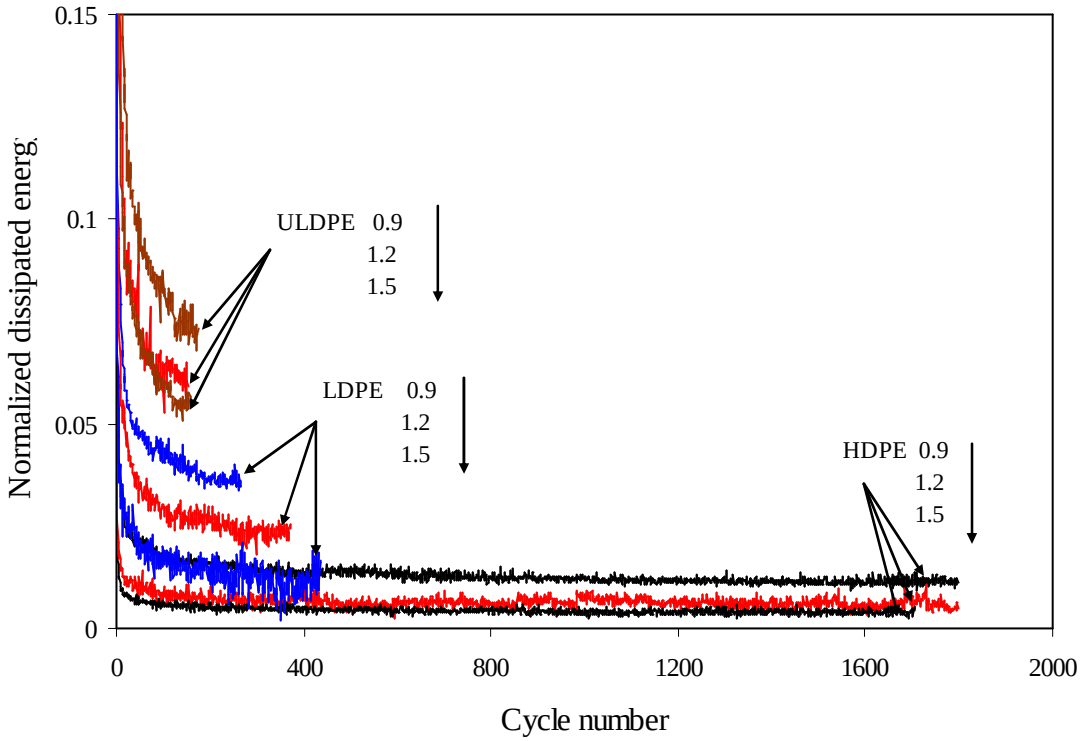

Fig. 1.11. Normalized dissipated energy for the three polyethylene materials.

II.5.2. Maximum stress vs. cycle number

The normalized maximum stress is plotted in **Fig. 1.12** as a function of the cycle number. The maximum stress is normalized over the value at the first cycle. The maximum stress decreases with increasing cycle number until it reaches a steady state. On the other hand, the rate of maximum stress decrease depends on both the maximum strain and the crystal content. Furthermore, it can be observed that increasing the maximum strain contributes to increase the rate at which the maximum stress decreases. Moreover, increasing the crystal content leads to an increasing of the rate at which the maximum stress decreases. However, this last statement is appropriate only HDPE and ULDPE as LDPE has no intermediate behavior.

II.5.3. Residual strain vs. cycle number

The normalized residual strain is plotted in **Fig. 1.13** as a function of the cycle number**.** The residual strain of each cycle was normalized over the value at the first cycle. The results show that the residual strain increases with increasing cycle number until it reaches a steady state. Besides, the residual strain depends on both the maximum strain and the crystal content. It can be observed that increasing the maximum strain contributes to slowdown the increasing-rate of residual strain while decreasing the crystal content leads to accelerate the increasing-rate of residual strain.

II.6. Stress relaxation

The stress relaxation is another test allowing giving an indication of the polyethylene viscous response. During the relaxation test, the specimen is deformedup to a predetermined local strain reduceconstant true strain rate. The local strain is then kept constant for a prescribed delay during which the true stressis. All relaxation tests are conducted for duration of at least one hour.

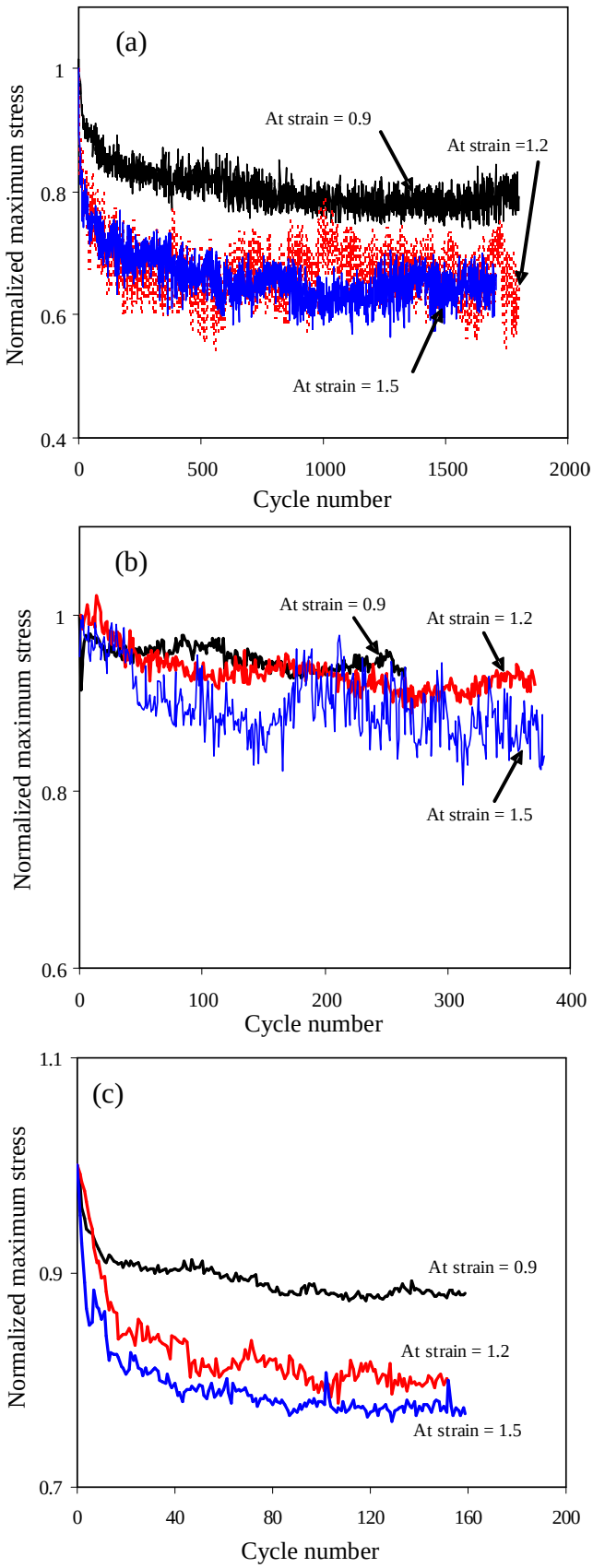

Fig. 1.12. Normalized maximum stress: (a) HDPE, (b) LDPE, (c) ULDPE.

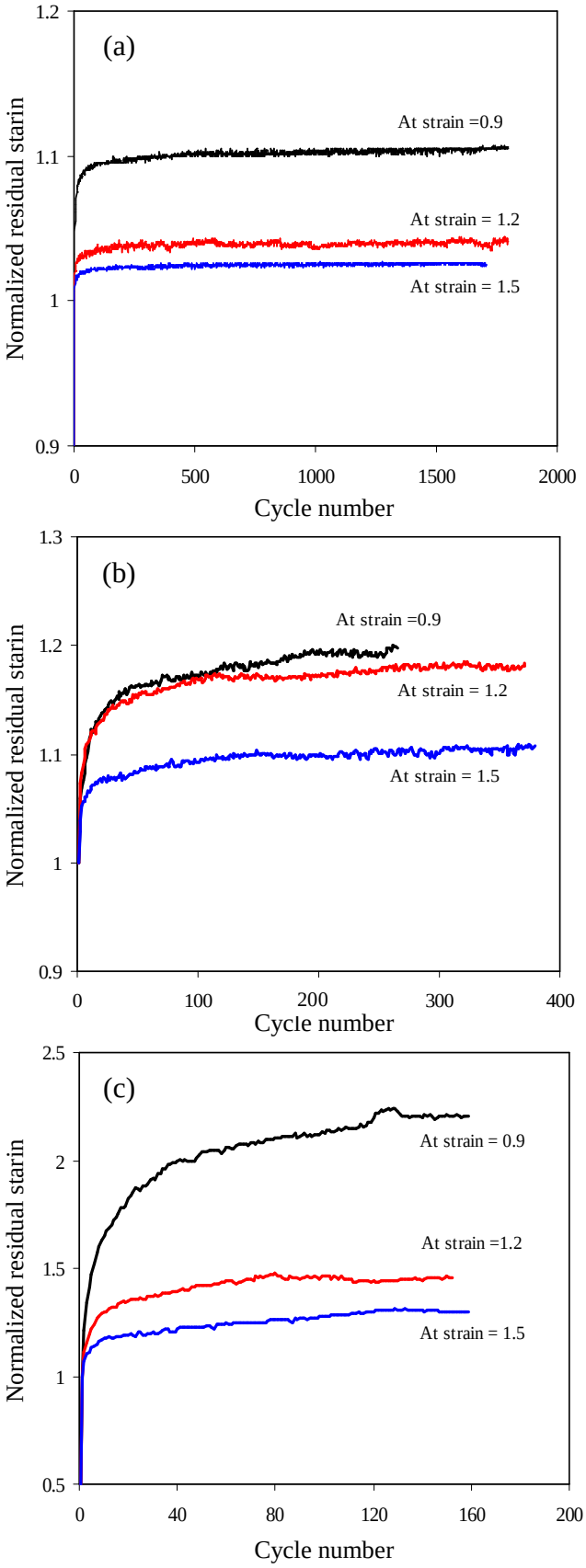

Fig. 1.13. Normalized residual strain: (a) HDPE, (b) LDPE, (c) ULDPE.

The normalized stress relaxation vs. time is plotted in **Fig. 1.14** for three polyethylene materials. A strong stress decrease can be observed at the beginning of the relaxation, followed by a slowdown of the stress rate decreasing with time.
It can be notice that stress relaxation is influenced by crystal content. The normalized stress relaxation rate of HDPE is higher than in the two other polyethylene materials. Furthermore, the normalized stress relaxation rate of ULDPE is higher than in LDPE. Note that, LDPE does not exhibit an intermediate, between HDPE and ULDPE, stress relaxation behavior.

The stress relaxation curves are fitted using the following formula:

$$\sigma(t) = \sigma(\infty) + \left(\sigma(0) - \sigma(\infty)\right)\exp\left(-(t/\tau)^b\right) \tag{1.6}$$

where $\sigma(0)$ is the instantaneous stress, $\sigma(\infty)$ is the equilibrium stress, b is a parameter related to the spread of the initial relaxation time, τ is the average relaxation time parameter, and t is the relaxation time. The coefficients b and τ are plotted as a function of the crystal content **Fig. 1.15.** The two coefficients can be according to the following formula.

$$\begin{aligned} b &= 0.48\chi_{cv}^{-0.347} \\ \tau &= 381.56\exp\left(-1.6949\chi_{cv}\right) \end{aligned} \tag{1.7}$$

Both the average relaxation time τ and b coefficient decrease with the crystal fraction. The stress relaxation behavior is partially determined by the mobility of the macromolecular chains in the crystalline and amorphous regions. In crystal regions, the mobility of macromolecular chain segments are limited by crystals, e.g. when the crystal rate increases then the mobility of macromolecular chain segments in the crystal and amorphous regions are restricted. On the other hand, tied chains connecting crystal and amorphous regions are formed by macromolecular chains which exist in both crystalline and amorphous phase and act as physical cross-links (Ying Lu et al., 2010).

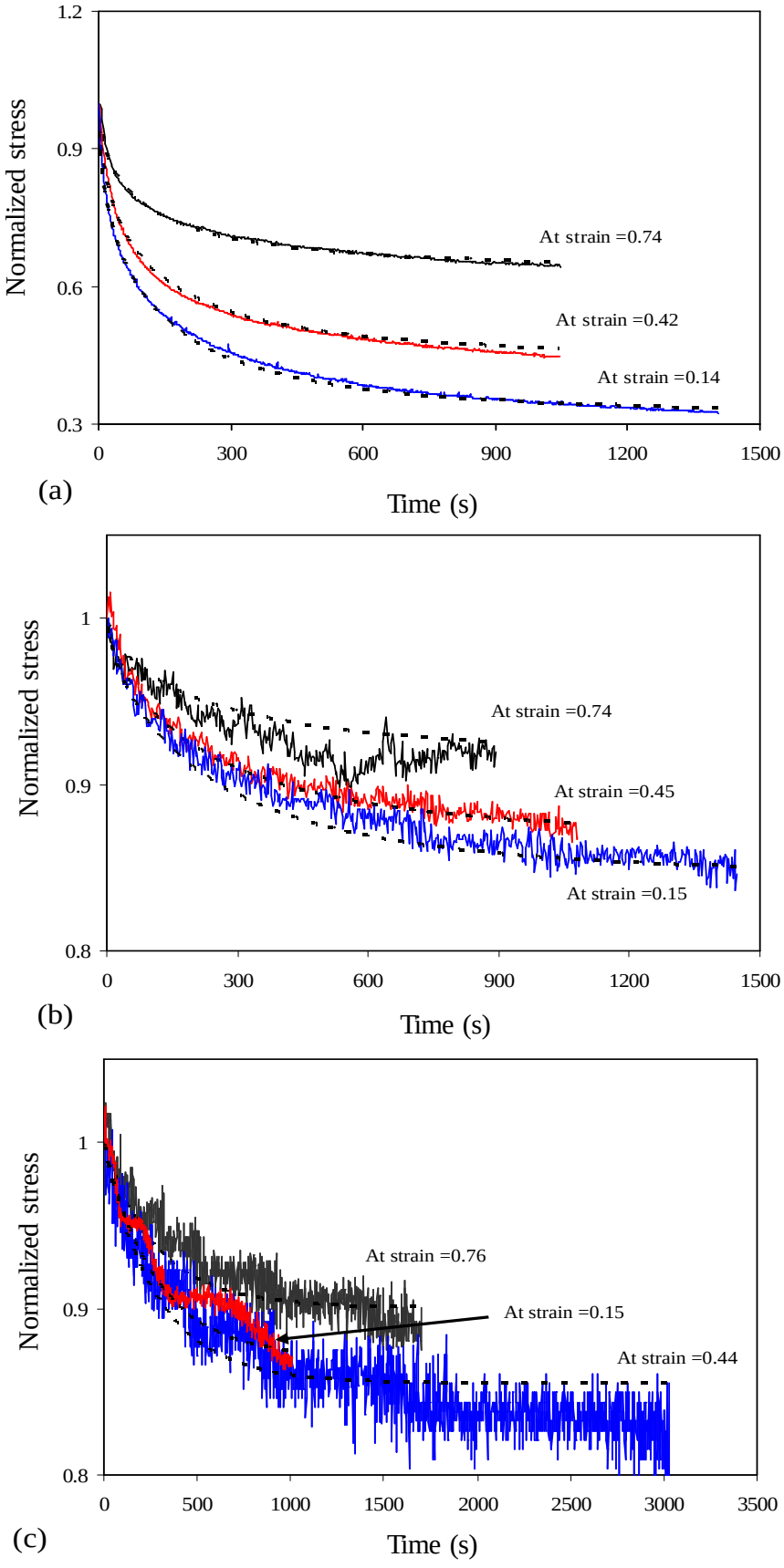

Fig. 2.14. Normalized stress relaxation: (a) HDPE, (b) LDPE, (c) ULDPE

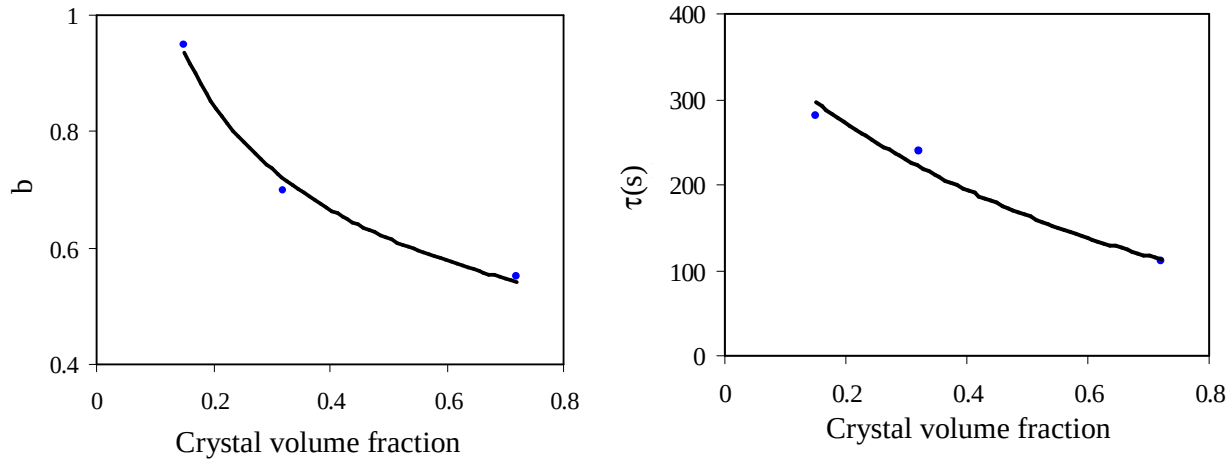

Fig. 2.15. Stress relaxation parameters evolution.

III. Partial conclusions

The time-dependent mechanical characteristics of polyethylene were experimentally examined: The rate-dependent yield strength and strain hardening, the cyclic stress-softening, the hysteresis, the remaining strain and the stress relaxation are all strongly influenced by the crystal content.

This first chapter constitutes a fruitful database for the development of a constitutive modeling able to capture the general trends of the polyethylene mechanical response. This is the aim of the next chapter.

REFERENCES:

Ayoub, G., Zaïri, F., Fréderix, C., Gloaguen, J.M., Naït-Abdelaziz, M., Seguela, R., Lefebvre, J.M., 2011. Effects of crystal content on the mechanical behaviour of polyethylene under finite strains: Experiments and constitutive modelling. International Journal of Plasticity. 27, 492-511.

Ayoub, G., Zaïri, F., Naït-Abdelaziz, M., Gloaguen, J.M., 2010. Modelling large deformation behaviour under loading–unloading of semicrystalline polymers: Application to a high density polyethylene. International Journal of Plasticity. 26, 329-347.

Boyd, R.H., 1985. Relaxation processes in crystalline polymers: molecular interpretation – a review. Polymer. 26, 1123-1133.

G'Sell C., Marquez-Lucero A., 1993. Determination of the intrisic stress/strain equation of thin polymer films from stretching expriments under plane-strain tension. Polymer. 34, 2740-2749.

G'Sell, C., Hiver, J.M., Dahoun, A., Souahi, A., 1992. Video-controlled tensile testing of polymers and metals beyond the necking point. Journal of Materials Science. 27, 5031-5039.

Ferreiro, V., Coulon, G., 2004. Shear banding in strained semicrystalline polyamide 6 films as revealed by atomic force microscopy: role of the amorphous phase. Journal of Polymer Science, Part B: Polymer Physics. 42, 687–701.

Popli, R., Glotin, M., Mandelkern, L., Benson, R.S., 1984. Dynamic mechanical studies of a and b relaxations of polyethylenes. Journal of Polymer Science, Part B: Polymer Physics. 22, 407- 448.

Soares, J.B.P., Kim, J.D., Rempel, G.L., 1997. Analysis and control of the molecular weight and chemical composition distributions of polyolefins made with metallocene and Ziegler–Natta catalysts. Industrial and Engineering Chemistry Research. 36, 1144-1150.

Lu, Y. Yang, W., Zhang, K., Yang, M., 2010. Stress relaxation behavior of high density polyethylene (HDPE) articles molded by gas-assisted injection molding. Polymer Testing. 29, 866-871.

Wunderlich, B., 1980. Macromolecular Physics. Crystal Melting, vol. 3. Academic Press, New York.

Chapter two

FORMULATION AND IDENTIFICATION OF A CONSTITUTIVE MODEL FOR POLYETHYLENE MECHANICAL RESPONSE

This chapter includes parts. Part I deals with formulation and identification of a large-strain viscoelastic-viscoplastic model. To identify the model parameters, an analytical deterministic scheme and a practical, "engineering-like", numerical tool, based on a genetic algorithm are developed. Large-strain viscoelastic-viscoplastic approaches are adopted to describe the mechanical response of polyethylene. In a first approach, the polyethylene materials are considered as homogeneous media; at each crystal content, the polyethylene material is thus considered as a new material and a new set of model parameters is provided. In this approach the Boyce-Socrate-Llana (BSL) model has been employed. In a second approach, the polyethylene materials are seen as a two-phase composite and the effective contributions of the crystalline and amorphous phases to the overall mechanical response are integrated in the intermolecular resistance of BSL constitutive model. This model is referred to the MBSL1 model for modified BSL model (in a 1st version).

In part II, further modification are achieved to the BSL model and referred to the MBSL2 model for modified BSL model (in a 2nd version). In this modification, the effective contributions of the crystalline and amorphous phases to the overall mechanical response are incorporated in both intermolecular and network resistances of the BSL constitutive model. This improvement provides insight into the role of the crystalline and amorphous phases on macro-behavior of material deformation resistance, i.e. intermolecular and network resistances. The aim of this expansion is also to minimize the constitutive model

parameters, which allows simulating the transition from thermoplastic-like to elastomeric-like mechanical response.

I. Formulation and identification of a large-strain viscoelastic-viscoplastic model

Nowadays, thermoplastic polymers are widely used for engineering applications. However, the prediction of their mechanical behavior remains a complex task since these materials have a highly non-linear stress-strain relationship depending on several external (strain rate, temperature) and structural (entanglement, cross-linking, crystal content, crystalline lamellae size, lamellae distribution) factors. Besides, large plastic strains may be locally reached in polymer components. Over decades many constitutive models have emerged to predict the stress-strain behavior of amorphous thermoplastic polymers both in the glassy and rubbery states and many works have been done to improve the constitutive models to adapt and respond to different material types under different conditions, as reviewed in many works (Boyce et al., 1988; Arruda et al., 1993; Buckley and Jones, 1995; Wu and van der Giessen, 1995, Bardenhagen et al., 1997; Tervoort et al., 1997; Boyce et al., 2000 ; Frank and Brockman, 2001; Anand and Gurtin, 2003; Zaïri et al., 2005-a; Anand and Ames, 2006; Richeton et al., 2007; Pyrz and Zaïri, 2007; Zaïri et al., 2010; Belbachir et al., 2010; Ayoub et al., 2011). The physically-based constitutive models for the glassy amorphous polymers are inspired from the early work of Haward and Thackray (Haward and Thackray, 1968) founded on the observation of a large recoverable extension under glass transition points. In these constitutive models, a viscoplastic dashpot for the intermolecular interactions is connected to a non-linear spring to simulate the alignment of the polymer chains at large strains. To predict the stress-strain behavior of semi-crystalline polymers, many authors (Drozdov, 2011; Colak, 2005; Dusunceli and Colak, 2008; Zaïri et al. 2006; Ben Hadj Hamouda, 2007) used purely phenomenological constitutive models. Inherent to the structure of these

models is the absence of linking to the microstructure which prevents the understanding and prediction of crystal content effects on the overall mechanical response (Lee at al., 1993a; Lee et al., 1993b; Ahzi et al., 2003; van Dommelen et al., 2003; Makradi et al., 2005; Dupaix and Krishnan, 2006; Regrain et al., 2009; Ayoub et al., 2010, 2011). Recently, Ayoub et al. (2011) proposed a physically-based constitutive model for semi-crystalline polymers integrating explicitly the crystal content in the mathematical formulation. The constitutive model is based on the Boyce et al. (2000) approach, the latter extended by Ahzi et al. (2003) to capture the strain-induced crystallization of the initially amorphous polyethylene terephthalate. Inherent to the model structure is the assumption that the resistance in the semi-crystalline polymer to deformation is the sum of elastic-viscoplastic crystalline and amorphous intermolecular resistances and a visco-hyperelastic network resistance. The Ayoub et al. (2011) constitutive model was able to capture the transition from thermoplastic-like to elastomeric-like mechanical response of polyethylene, as the crystal content changes. The authors identified the model parameters using an analytical deterministic scheme. The deterministic procedure uses a precise algorithm of identification and calculates a unique set of model parameters (Pyrz and Zaïri, 2007). However, the application of this method demands an advanced expertise in model formulation and wide experience in the understanding of experimental material behavior. Moreover, during the cycle of model-experiments comparison and model (re)formulation, the complexity of material response leads often to an excessive number of model parameters which do not necessarily all have the reason for their existence.

The identification procedure is the main barrier of handling the constitutive models. The difficulty of model parameters identification is proportional with the complexity of the constitutive model itself; it is time wasting. An efficient technique of parameters identification is vital to a utility of constitutive models. Thus, developing a software solution for model parameters identification allows time and cost effective solution and keeps constitutive models much more useful

(Goldberg, 1989; Michalewicz, 1999; Melanie, 1999; Miettinen et al., 1999; Harth et al., 2004; Andrade-Campos et al., 2007; Chaparro et al., 2008; Franulovic et al., 2009, 2010; Mahmoudi et al., 2011; Lee, 1969). In this part, we intend to develop and evaluate a numerical tool which allows identifying the overall constitutive model variable sets, directly from stress-strain curves, to contrast with the analytical deterministic approach. Moreover, such identification procedures should be reliable, useful and convenient for a large number of users. The numerical tool proposed in this work is dedicated to non-specialists of mathematical optimization heuristics, thus to exhibiting a practical "engineering-like" tool design. A great deal of researches have been conducted on the model parameters identification for metals, but few researches have been carried out to determine the model parameters for polymers, especially at large deformation.

This part is focused on the constitutive modeling of semi-crystalline polymers but also on the problem of model parameters identification. A genetic algorithm (GA) based optimization procedure is designed to determine the parameters of large-strain viscoelastic-viscoplastic constitutive models, and the results determined by GA compared to results of an analytical deterministic scheme. The application is performed on polyethylene with a wide range of crystal fractions including thermoplastic elastomer and stiff thermoplastic polymer mechanical responses. To illustrate the interest, reliability and usefulness of the proposed numerical identification tool, two constitutive models are retained. One (Boyce et al., 2000) supposes the semi-crystalline material as homogeneous and the other (Ayoub et al., 2011) considers it as heterogeneous. The robustness of both constitutive models is examined. A secondary objective is to revise the Ayoub et al. (2011) constitutive model in order to reduce the required model parameters. This part is organised as follows: In Section I.1, we review two large-strain viscoelastic-viscoplastic constitutive modeling approaches. In Section I.2, we present the analytical deterministic scheme. In Section I.3, we present the computational formulations of the problem and GA-based identification tool has been designed.

In addition the robustness, reproducibility and uniqueness of the solutions are discussed. In Section I.4, the identification results are presented and discussed. In Section I.5, concluding remarks are presented for reviewed models.

I.1. Large-strain viscoelastic-viscoplastic constitutive models

In this section, the main elements of two developed constitutive models for thermoplastic polymers are summarized. The first one (referred to the BSL model for "Boyce-Socrate-Llana model") considers the material as homogeneous while the second one (referred to the MBSL1 model for "modified BSL model") treats the material as heterogeneous by distinguishing amorphous and crystalline phases of intermolecular resistance of the BSL model. These constitutive models satisfy the continuum mechanics rules within the context of the large-strain viscoelastic-viscoplastic framework. A common point of these constitutive models is that the resistance to deformation in the semi-crystalline polymers is the sum of a resistance *A* describing the intermolecular interactions and a resistance *B* describing the molecular network stretching and orientation process. The intermolecular resistance is composed of a linear elastic spring in series with a viscoplastic damper and the molecular network resistance is composed of a non-linear spring in series with a viscous damper.

As a point of departure, a summary of the finite strain kinematic framework is given. The key quantity is the deformation gradient defined by: $\mathbf{F} = \partial \mathbf{x} / \partial \mathbf{X}$ where $\mathbf{x}$ is the position of a material point in the deformed configuration and $\mathbf{X}$ is the position of this material point in the reference configuration. Note that all tensors are denoted by bold-face symbols.

Due to the model structure, the Taylor assumption prevails, i.e. the intermolecular deformation gradient $\mathbf{F}_A$ and the network deformation gradient $\mathbf{F}_B$ are equal to the total deformation gradient $\mathbf{F}$:

$$\mathbf{F} = \mathbf{F}_A = \mathbf{F}_B \tag{2.1}$$

Note that for the MBSL1 constitutive model the effective contribution of the crystalline and amorphous phases to the overall intermolecular resistance are also integrated with the Taylor assumption:

$$\mathbf{F}_A = \mathbf{F}_A^a = \mathbf{F}_A^c \tag{2.2}$$

where the superscripts *a* and *c* denote the amorphous and crystalline phases, respectively.

Following the Lee (1969) decomposition, schematically illustrated in **Fig. 2.1**, the deformation gradient tensors can be further decomposed multiplicatively into elastic (network) and viscoplastic (flow) parts as:

$$\mathbf{F}_A = \mathbf{F}_A^e \mathbf{F}_A^p \tag{2.3}$$

$$\mathbf{F}_B = \mathbf{F}_B^N \mathbf{F}_B^F \tag{2.4}$$

where the superscripts *e*, *p*, *N* and *F* denote the elastic, viscoplastic, network and flow parts, respectively. Note that the decomposition given in Eq. (2.3) is also applicable to crystalline and amorphous phases in the case of the MBSL1 constitutive model.

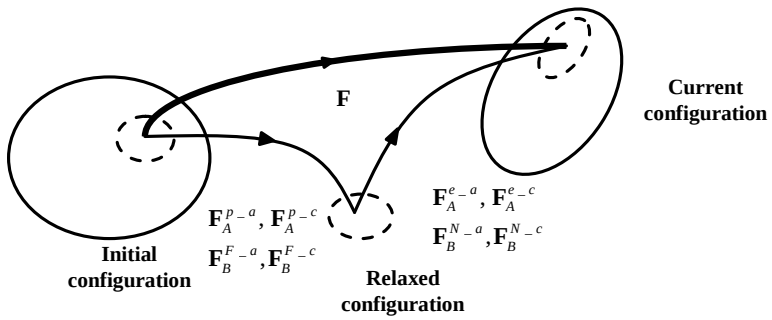

Fig. 2.1. Schematic illustration of the strain multiplicative decomposition.

According to the polar decomposition, the deformation gradient tensors can be further decomposed into stretch and rotation movements:

$$\mathbf{F}_A = \mathbf{V}_A^e \mathbf{R}_A^e \mathbf{V}_A^p \mathbf{R}_A^p \tag{2.5}$$

$$\mathbf{F}_B = \mathbf{V}_B^N \mathbf{R}_B^N \mathbf{V}_B^F \mathbf{R}_B^F \tag{2.6}$$

The rate kinematics $\mathbf{L}_A = \dot{\mathbf{F}}_A \mathbf{F}_A^{-1}$ for resistance A and $\mathbf{L}_B = \dot{\mathbf{F}}_B \mathbf{F}_B^{-1}$ for resistance B are described by the velocity gradients:

$$\mathbf{L}_A = \dot{\mathbf{F}}^e \mathbf{F}_A^{e^{-1}} + \mathbf{F}_A^e \dot{\mathbf{F}}_A^p \mathbf{F}_A^{p^{-1}} \mathbf{F}_A^{e^{-1}} = \mathbf{L}_A^e + \mathbf{L}_A^p \tag{2.7}$$

$$\mathbf{L}_B = \dot{\mathbf{F}}^N \mathbf{F}_B^{N^{-1}} + \mathbf{F}_B^N \dot{\mathbf{F}}_B^F \mathbf{F}_B^{F^{-1}} \mathbf{F}_B^{N^{-1}} = \mathbf{L}_B^N + \mathbf{L}_B^F \tag{2.8}$$

in which the dot expresses the time derivative. The plastic and flow parts $\mathbf{L}_A^p$ and $\mathbf{L}_B^F$ of the velocity gradients may be written as:

$$\mathbf{L}_A^p = \mathbf{F}_A^e \dot{\mathbf{F}}_A^p \mathbf{F}_A^{p^{-1}} \mathbf{F}_A^{e^{-1}} = \mathbf{D}_A^p + \mathbf{W}_A^p \tag{2.9}$$

$$\mathbf{L}_B^F = \mathbf{F}_B^N \dot{\mathbf{F}}_B^F \mathbf{F}_B^{F^{-1}} \mathbf{F}_B^{N^{-1}} = \mathbf{D}_B^F + \mathbf{W}_B^F \tag{2.10}$$

where $\mathbf{D}_A^p$ and $\mathbf{D}_B^F$ are the rates of inelastic deformation and, $\mathbf{W}_A^p$ and $\mathbf{W}_B^F$ are the inelastic spins which are assumed, without loss of generality, equal to zero. In addition to be irrotational, the viscoplastic flow is assumed incompressible, i.e. $\det \mathbf{F}_A^p = \det \mathbf{F}_B^F = 1$.

The plastic and flow deformation gradients $\mathbf{F}_A^p$ and $\mathbf{F}_B^F$ are computed by integrating the following formula derived from Eqs. (2.9) and (2.10):

$$\dot{\mathbf{F}}_A^p = \mathbf{F}_A^{e^{-1}} \mathbf{D}_A^p \mathbf{F}_A^e \mathbf{F}_A^p \tag{2.11}$$

$$\dot{\mathbf{F}}_B^F = \mathbf{F}_B^{N^{-1}} \mathbf{D}_B^F \mathbf{F}_B^N \mathbf{F}_B^F \tag{2.12}$$

in which the rates of inelastic deformation $\mathbf{D}_A^p$ and $\mathbf{D}_B^F$ must be prescribed.

In the case of the MBSL1 constitutive model, two rates of inelastic deformation $\mathbf{D}_A^{p-c}$ and $\mathbf{D}_A^{p-a}$ must be specified for the crystalline and amorphous domains, leading to two distinct viscoplastic and elastic deformation gradients for the two phases. The elastic and network deformation gradients $\mathbf{F}_A^e$ and $\mathbf{F}_B^N$ are obtained using Eqs. (2.3) and (2.4).

I.1.1. Boyce-Socrate-Llana (BSL) constitutive model

The first constitutive model presented in this section, is that proposed by Boyce et al. (2000). This model is based on two basic resistances, as can be seen in **Fig. 2.2**.

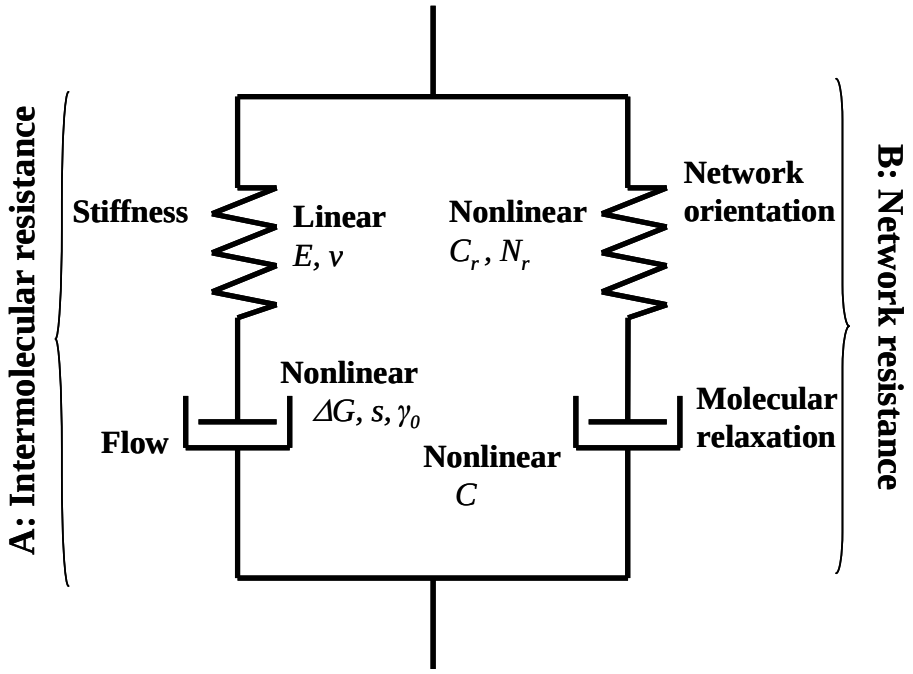

Fig. 2.2. Schematic representation of the BSL constitutive model.

I.1.1.1. Resistance A: intermolecular interactions

The intermolecular resistance is constituted by a linear spring in series with a viscoplastic dumper. The intermolecular Cauchy stress $\mathbf{T}_A$ is related to the stretch part of the elastic deformation gradient $\mathbf{V}_A^e$ by the following constitutive relationship:

$$\mathbf{T}_A = \frac{1}{J_A^e}\mathbf{C}_A^e \ln\left(\mathbf{V}_A^e\right) \tag{2.13}$$

in which $J_A^e = \det \mathbf{F}_A^e$ is the elastic volume change, $\ln\left(\mathbf{V}_A^e\right)$ is the Hencky strain and $\mathbf{C}_A^e$ is the fourth-order elastic stiffness tensor expressed, in the isotropic case, as follows:

$$\left(C_A^e\right)_{ijkl} = \frac{E}{2(1+\nu)}\left[\left(\delta_{ik}\delta_{jl}+\delta_{il}\delta_{jk}\right)+\frac{2\nu}{1-2\nu}\delta_{ij}\delta_{kl}\right] \tag{2.14}$$

in which two parameters are involved: the Young's modulus E and the Poisson's ratio ν. The term δ represents the Kronecker-delta symbol.

The viscoplastic strain rate tensor $\mathbf{D}_A^p$ is described by the following flow rule:

$$\mathbf{D}_A^p = \dot{\gamma}_A^p \frac{\mathbf{T}_A'}{\sqrt{2}\tau_A} \tag{2.15}$$

where $\mathbf{T}_A' = \mathbf{T}_A - \text{trace}(\mathbf{T}_A)/3\mathbf{I}$ is the deviatoric part of $\mathbf{T}_A$, $\tau_A = (\mathbf{T}_A'.\mathbf{T}_A'/2)^{1/2}$ is the effective stress and $\dot{\gamma}_A^p$ is the viscoplastic shear strain rate:

$$\dot{\gamma}_A^p = \gamma_0 \exp\left[-\frac{\Delta G}{k\theta}\left(1-\frac{\tau_A}{s}\right)\right] \tag{2.16}$$

in which three parameters are involved: the pre-exponential factor γ_0, the activation energy ΔG and the thermal shear strength s. The terms k and θ denote the Boltzmann's constant and the absolute temperature, respectively.

I.1.1.2. Resistance B: network stretching and orientation process

The molecular network resistance is constituted by a non-linear spring in series with a viscous dumper. The molecular network Cauchy stress $\mathbf{T}_B$ is expressed as a function of the elastic deformation gradient $\mathbf{F}_B^N$ using a relationship involving an inverse Langevin function L^{-1} (Boyce et al., 2000):

$$\mathbf{T}_B = \frac{1}{J_B^N}\frac{C_r}{3}\frac{\sqrt{N_r}}{\bar{\lambda}_B^N}\text{L}^{-1}\left(\frac{\bar{\lambda}_B^N}{\sqrt{N_r}}\right)\left[\bar{\mathbf{B}}^N - \left(\bar{\lambda}_B^N\right)^2\mathbf{I}\right] \tag{2.17}$$

in which two parameters are involved: the initial hardening modulus C_r and the limiting chain extensibility $\sqrt{N_r}$. The term $J_B^N = \det \mathbf{F}_B^N$ is the network volume change, $\mathbf{I}$ is the identity tensor, $\bar{\lambda}_B^N$ and is given by: $\bar{\lambda}_B^N = \left[\text{trace}\left(\bar{\mathbf{B}}^N\right)/3\right]^{1/2}$ in which $\bar{\mathbf{B}}^N = \left(J_B^N\right)^{-2/3}\mathbf{F}_B^N\left(\mathbf{F}_B^N\right)^T$.

The flow strain rate tensor $\mathbf{D}_B^F$ is described by the following flow rule:

$$\mathbf{D}_B^F = \dot{\gamma}_B^F \frac{\mathbf{T}_B'}{\sqrt{2}\tau_B} \tag{2.18}$$

where $\mathbf{T}_B' = \mathbf{T}_B - \text{trace}(\mathbf{T}_B)/3\mathbf{I}$ is the deviatoric part of $\mathbf{T}_B$, $\tau_B = (\mathbf{T}_B'.\mathbf{T}_B'/2)^{1/2}$ is the effective stress and $\dot{\gamma}_B^F$ is the flow shear strain rate:

$$\dot{\gamma}_B^F = C\left(\lambda_B^F - 1\right)^{-1}\tau_B \tag{2.19}$$

in which one parameter is involved: the viscous parameter C. The term λ_B^F is given by: $\lambda_B^F = \left[\text{trace}\left(\mathbf{B}^F\right)/3\right]^{1/2}$ in which $\mathbf{B}^F = \mathbf{F}_B^F \left(\mathbf{F}_B^F\right)^T$.

The overall Cauchy stress tensor $\mathbf{T}$ is the sum of the intermolecular Cauchy stress tensor $\mathbf{T}_A$ and the network Cauchy stress tensor $\mathbf{T}_B$:

$$\mathbf{T} = \mathbf{T}_A + \mathbf{T}_B \tag{2.20}$$

The intermolecular part of the BSL model involves five parameters and its network part three parameters, totalling eight parameters.

I.1.2. Modified Boyce-Socrate-Llana (MBSL1) constitutive model

Semi-crystalline materials may be considered as heterogeneous materials which comprise both amorphous and crystalline domains coupled in a rather complex manner. In order to treat the large-strain viscoelastic-viscoplastic response of polyethylene materials containing a wide range of crystal fractions and a rubbery amorphous phase, Ayoub et al. (2011) proposed a micromechanical approach inspired from that initially proposed by Ahzi et al. (2003) for the strain-induced crystallization of initially amorphous polyethylene terephthalate above the glass transition temperature. The constitutive model proposed by Ayoub et al. (2011) introduces the crystal volume fraction as variable and is able to capture the transition from thermoplastic-like to elastomeric-like response of polyethylene when the crystal content χ_{cv} decreases. This material characteristic is illustrated in **Fig. 2.3-a** in which it can be observed that a decrease in crystal content leads to a decrease in initial elastic stiffness, a more gradual rollover to yield a decrease in both yield, stress and in strain hardening slope. From a micromechanical point of view, the semi-crystalline material may be modeled as a two-phase composite, as depicted in **Fig. 2.3-b**, constituted by crystalline and rubbery amorphous domains. The micromechanics homogenization scheme will allow reaching the macro-scale behavior. Both crystalline and amorphous domains are supposed to

participate to intermolecular interactions by acting in parallel. The rheological representation of the model is given in **Fig. 2.4**.

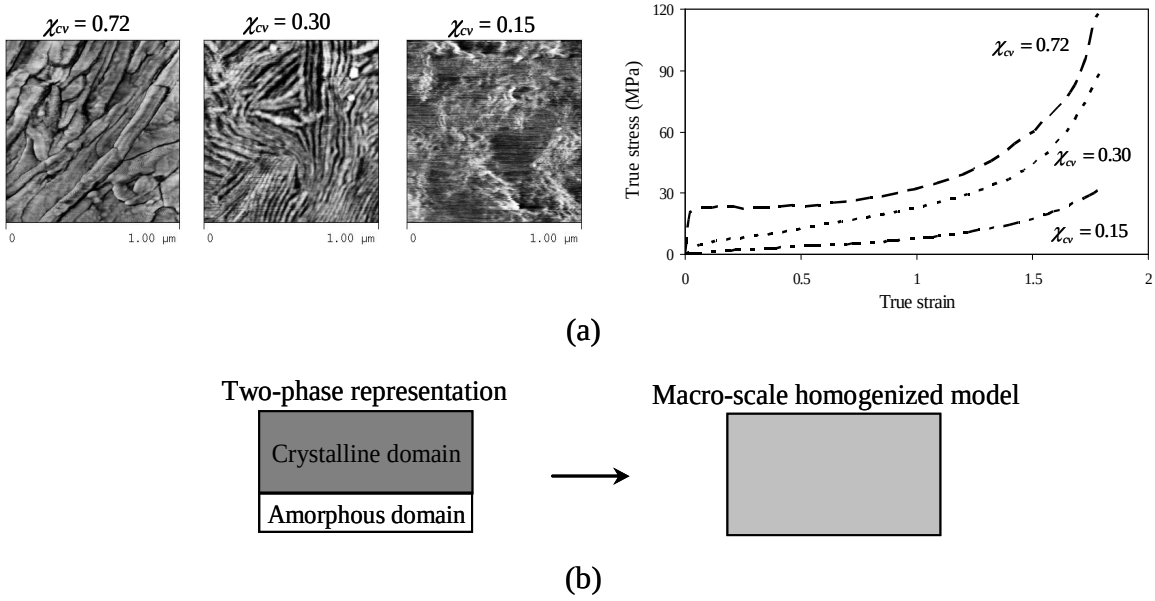

Fig. 2.3. Structure-response relationship and micromechanics-based modeling: (a) Microstructure of semi-crystalline polyethylene materials and corresponding large-strain mechanical response above the glass transition temperature, (b) micromechanical treatment using the volume fraction concept.

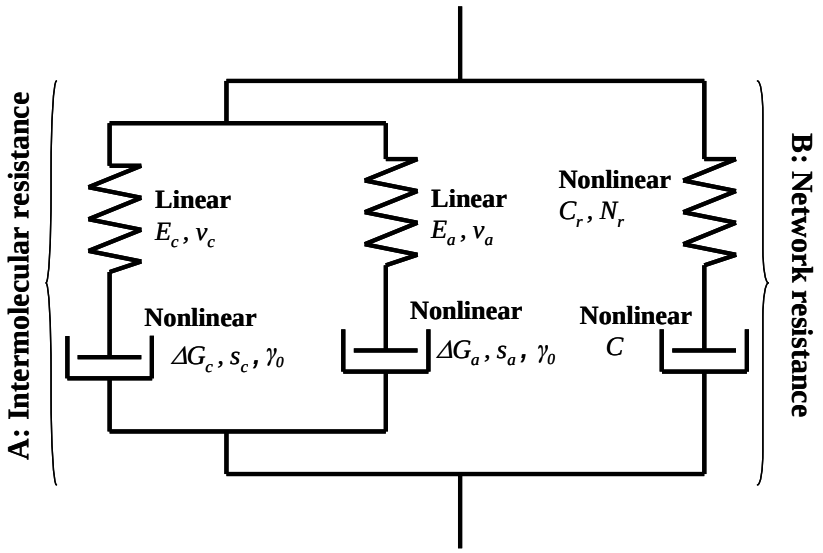

Fig. 2.4. Schematic representation of the MBSL1 constitutive model.

I.1.2.1. Resistance A: intermolecular interactions

The resistance A represents the contribution of both crystalline and amorphous phases and the effect of both phases can be treated in a composite framework. The overall intermolecular Cauchy stress $\mathbf{T}_A$ is given by (Ayoub et al. 2011):

$$\mathbf{T}_A = \left(\chi_{cv}\right)^{\beta} \mathbf{T}_A^c + \left(1-\chi_{cv}\right)^{\beta} \mathbf{T}_A^a \tag{2.21}$$

where χ_{cv} is the crystal volume fraction, and β is a material constant to account for interaction phenomena. The β constant has been estimated in (Ayoub et al. 2011) by inverse method using polyethylene systems over a wide range of crystal fractions and a value of 3.8 has been found. $\mathbf{T}_A^c$ and $\mathbf{T}_A^a$ are the crystalline and amorphous Cauchy stresses, respectively, related to the corresponding stretch part of the elastic deformation gradient $\mathbf{V}_A^{e-c}$ and $\mathbf{V}_A^{e-a}$ by the following constitutive relationships:

$$\mathbf{T}_A^c = \frac{1}{J_A^{e-c}} \mathbf{C}_A^{e-c} \ln\left(\mathbf{V}_A^{e-c}\right) \tag{2.22}$$

$$\mathbf{T}_A^a = \frac{1}{J_A^{e-a}} \mathbf{C}_A^{e-a} \ln\left(\mathbf{V}_A^{e-a}\right) \tag{2.23}$$

in which $J_A^{e-i} = \det \mathbf{F}_A^{e-i}$ is the elastic volume change, $\ln\left(\mathbf{V}_A^{e-i}\right)$ is the Hencky strain and $\mathbf{C}_A^{e-i}$ is the fourth-order elastic stiffness tensor of the crystalline and amorphous phases; the exponent i denotes the phase under consideration (crystalline c or amorphous a). Assuming both phases isotropic $\mathbf{C}_A^{e-i}$ can be expressed as:

$$\left(C_A^{e-c}\right)_{ijkl} = \frac{E_c}{2\left(1+\nu_c\right)}\left[\left(\delta_{ik}\delta_{jl}+\delta_{il}\delta_{jk}\right)+\frac{2\nu_c}{1-2\nu_c}\delta_{ij}\delta_{kl}\right] \tag{2.24}$$

$$\left(C_A^{e-a}\right)_{ijkl} = \frac{E_a}{2\left(1+\nu_a\right)}\left[\left(\delta_{ik}\delta_{jl}+\delta_{il}\delta_{jk}\right)+\frac{2\nu_a}{1-2\nu_a}\delta_{ij}\delta_{kl}\right] \tag{2.25}$$

in which four parameters are involved: the Young's moduli E_c and E_a, and the Poisson's ratios ν_c and ν_a.

The viscoplastic strain rate tensors of the crystalline portion $\mathbf{D}_A^{p-c}$ and the amorphous portion $\mathbf{D}_A^{p-a}$ are given by:

$$\mathbf{D}_A^{p-c} = \dot{\gamma}_A^{p-c} \frac{\mathbf{T}'^{-c}_A}{\sqrt{2}\tau_A^c} \tag{2.26}$$

$$\mathbf{D}_A^{p-a} = \dot{\gamma}_A^{p-a} \frac{\mathbf{T}'^{-a}_A}{\sqrt{2}\tau_A^a} \tag{2.27}$$

where $\mathbf{T}'^{-c}_A$ and $\mathbf{T}'^{-a}_A$ are the deviatoric parts of $\mathbf{T}_A^c$ and $\mathbf{T}_A^a$, respectively, $\tau_A^c = \left(\mathbf{T}'^{-c}_A . \mathbf{T}'^{-c}_A / 2\right)^{1/2}$ and $\tau_A^a = \left(\mathbf{T}'^{-a}_A . \mathbf{T}'^{-a}_A / 2\right)^{1/2}$ are the effective stresses and, $\dot{\gamma}_A^{p-c}$ and $\dot{\gamma}_A^{p-a}$ are the flow shear strain rates which follow the same expressions:

$$\dot{\gamma}_A^{p-c} = \gamma_0 \exp\left[-\frac{\Delta G_c}{k\theta}\left(1 - \frac{\tau_A^c}{\kappa s_c}\right)\right] \tag{2.28}$$

$$\dot{\gamma}_A^{p-a} = \gamma_0 \exp\left[-\frac{\Delta G_a}{k\theta}\left(1 - \frac{\tau_A^a}{s_a}\right)\right] \tag{2.29}$$

in which five parameters are involved: the pre-exponential factor γ_0, the activation energies ΔG_c and ΔG_a, and the athermal shear strengths s_c and s_a. The couple of parameters ΔG_a and s_a capture barrier to molecular chain segment rotation in the amorphous phase whereas the couple of parameters ΔG_c and s_c capture barrier to crystallographic shear in the crystalline phase. The term κ, introduced in Eq. (2.28), is a scale factor taking into account the effect of crystal morphology (depending on crystal content) on the crystal flow shear strain rate. In order to reduce the number of model parameters, it is worth noticing that the shear strengths s_c and s_a are considered to be constant with the plastic stretch, which constitutes a valuable difference with the MBSL1 constitutive model initially proposed by Ayoub et al. (2011).

I.1.2.2. Resistance B: network stretching and orientation process

It is assumed that the strain hardening response is dominated by molecular orientation rather than crystallographic orientation. The resistance *B* is also

constituted by a non-linear spring in series with a viscous damper and the same equations listed earlier in Section I.1.1.2 are used. The sum of the intermolecular Cauchy stress and the network Cauchy stress gives the overall Cauchy stress in the semi-crystalline polymer. The MBSL1 model requires ten input data for its intermolecular part and three others for its network part, totalling thirteen parameters.

I.2. Deterministic identification of model parameters

In this section, the methodology to identify the BSL and MBSL1 parameters following a classical analytical deterministic method is detailed: the approach consists of identifying successively the different branches of the constitutive model following a "step-by-step" methodology. The application is performed on polyethylene materials at different crystal volume fractions, and stretched at different strain rates. The details of the experiments (microscopic and macroscopic mechanical characterizations) can be found elsewhere (Ayoub et al., 2011).

I.2.1. Identification of BSL model parameters

The initial elastic stiffness E is obtained from the initial slope of the stress-strain curve. The pre-exponential factor $\dot{\gamma}_0$ is prescribed to a value of 1.75×10^6 s^{-1} (Boyce et al., 2000) which will be taken in all what follows. Fixing $\dot{\gamma}_0$ to this value, the activation energy ΔG and the shear strength s are determined using the following relation:

$$\tau_{y,A} = \frac{sk\theta}{\Delta G}\ln\left(\frac{\dot{\gamma}_A^p}{\dot{\gamma}_0}\right) + s \tag{2.30}$$

in which $\dot{\gamma}_A^p$ and $\tau_{y,A}$ were approximated as $\sqrt{3}\dot{\varepsilon}$ and $\sigma_y/\sqrt{3}$, respectively, $\dot{\varepsilon}$ being the applied strain rate and σ_y the experimentally measured yield stress. The shear yield stress being plotted as a function of the normalized strain rate for the three polyethylene materials (**Fig. 2.5**), the parameters ΔG and s are

simultaneously determined by a linear regression method using Eq. (2.30). The network parameters C_r, N_r and C, are the outcome of a fitting procedure on the strain hardening. The parameter values determined by this method are listed in **Table 2.1**. The comparison between experimental and simulated stress-strain curves can be found in **Fig. 2.6**. The BSL model is able to capture the experimental observations, over the range of crystallinities and strain rates under investigation, to a satisfactory extent.

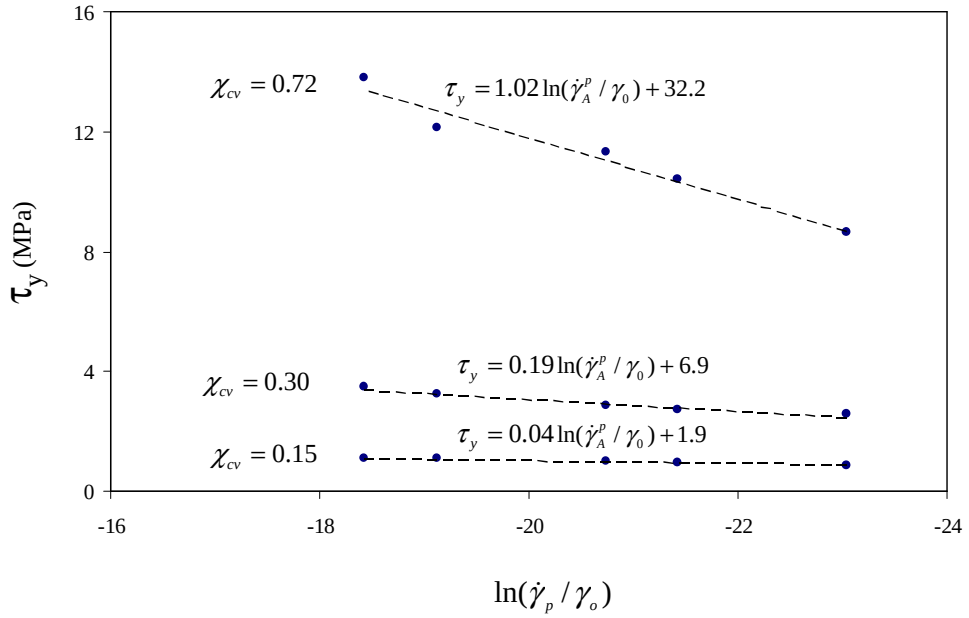

Fig. 2.5. Shear yield stress as a function of the normalized strain rate.

	E (MPa)	ΔG (J)	s (MPa)	C (MPa.s)$^{-1}$	C_r (MPa)	N_r
$\chi_{cv} = 0.72$	1250	1.28×10^{-19}	32.29	9.00×10^{-08}	2.7	26
$\chi_{cv} = 0.30$	65	1.46×10^{-19}	6.91	1.00×10^{-08}	2.7	54
$\chi_{cv} = 0.15$	6.4	1.68×10^{-19}	1.98	5.00×10^{-09}	1.0	110

Table 2.1. Identified parameters by deterministic approach for the BSL constitutive model.

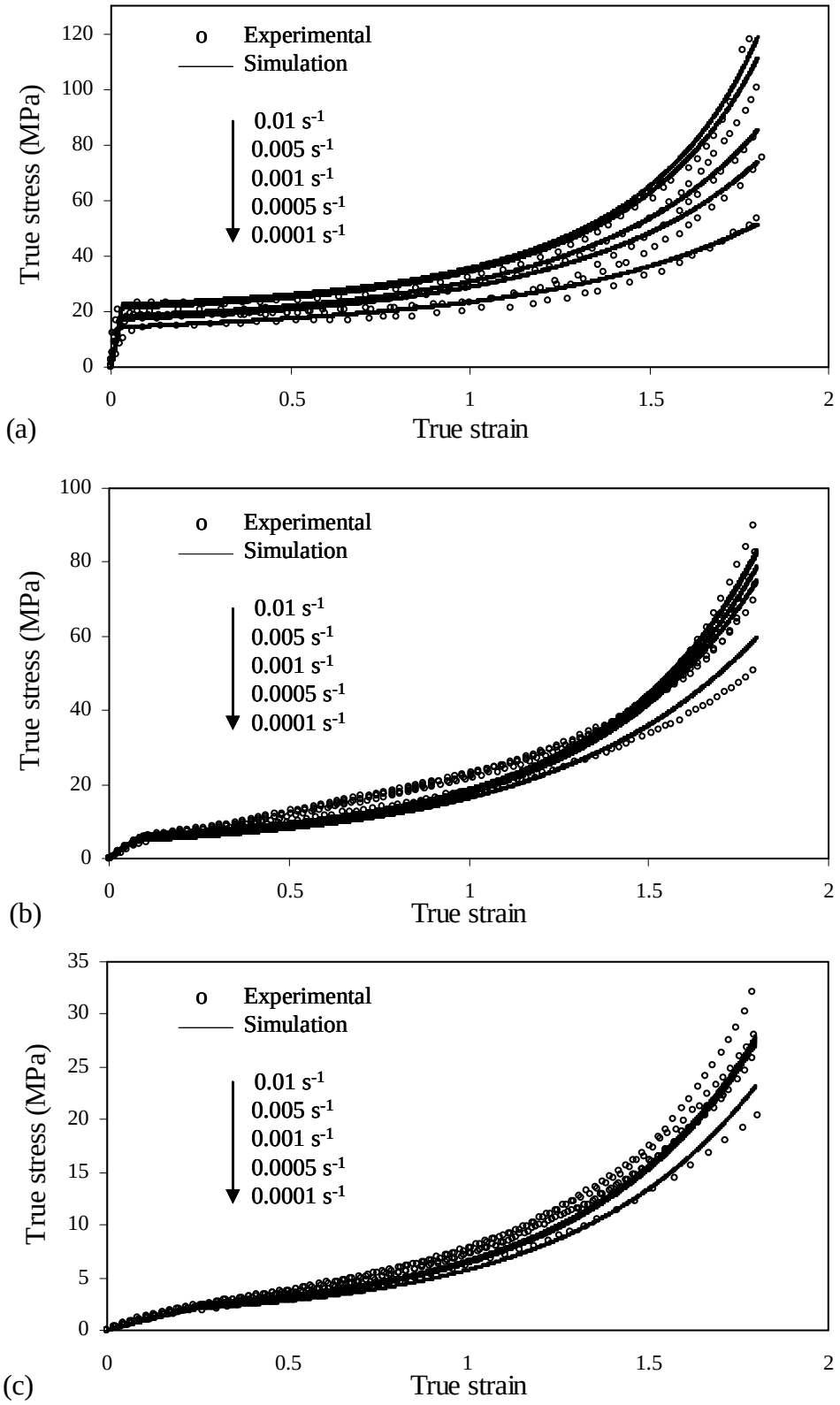

Fig. 2.6. Stress-strain curves of the BSL constitutive model following the deterministic identification parameter results for different crystal volume fractions: (a) HDPE, (b) LDPE, (c) ULDPE.

I.2.2. Identification of MBSL1 model parameters

Fig. 2.7 presents the parameters E, ΔG, κ and s as a function of the crystal volume fraction, the trends being captured by non-linear regressions. Following the MBSL1 decomposition of amorphous and crystalline domains, it is possible to focus on the specific corresponding parameters:

$$\begin{aligned} &\{E_a, \Delta G_a, s_a\} \quad \text{for } \chi_c = 0 \\ &\{E_c, \Delta G_c, s_c\} \quad \text{for } \chi_c = 1 \end{aligned} \tag{2.31}$$

The parameter values of amorphous and crystal domains are given in **Table 2.2**. Keep in mind that a key assumption of this approach is that the properties of crystalline and amorphous domains are the same whatever the crystal content. That is a consequence of the micromechanics homogenization concepts which see the semi-crystalline materials as two-phase composites. An important difference between crystalline and amorphous parameters may be observed. The network parameters C_r, N_r and C follow a monotonic evolution with the crystal volume fraction as shown in **Fig. 2.7**. The comparison between the model and the experimental data is shown in **Fig. 2.8**. It can be observed that the two-phase MBSL1 constitutive model stays in good agreement with the experimental data.

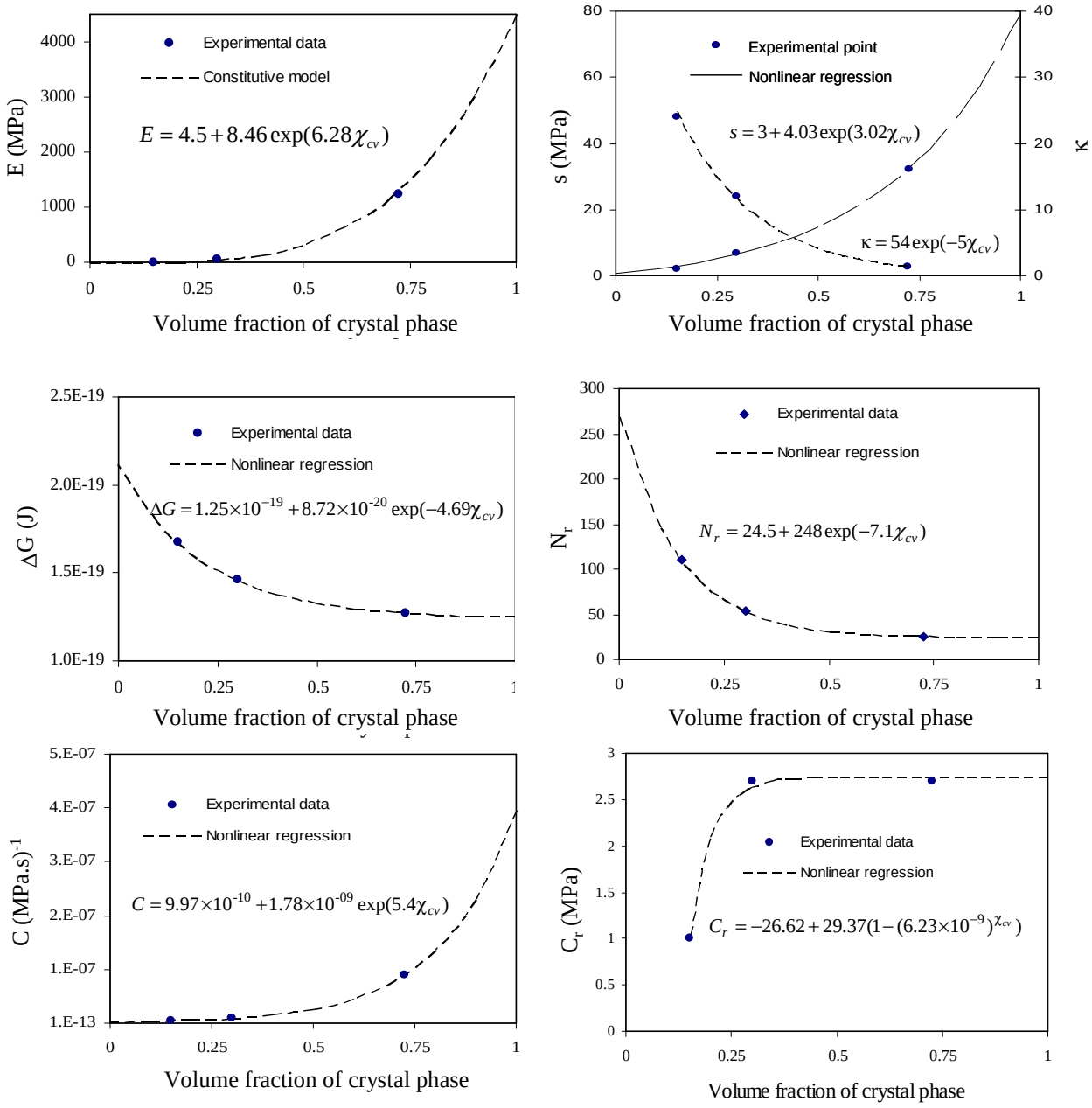

Fig. 2.7. Parameter evolutions plotted as a function of the crystal volume fraction.

E_c (MPa)	E_a (MPa)	ΔG_c (J)	ΔG_a (J)	s_c (MPa)	s_a (MPa)
4490	4.7	1.25×10^{-19}	2.12×10^{-19}	78.84	0.55

Table 2.2. Identified parameters by deterministic approach for the MBSL1 constitutive model.

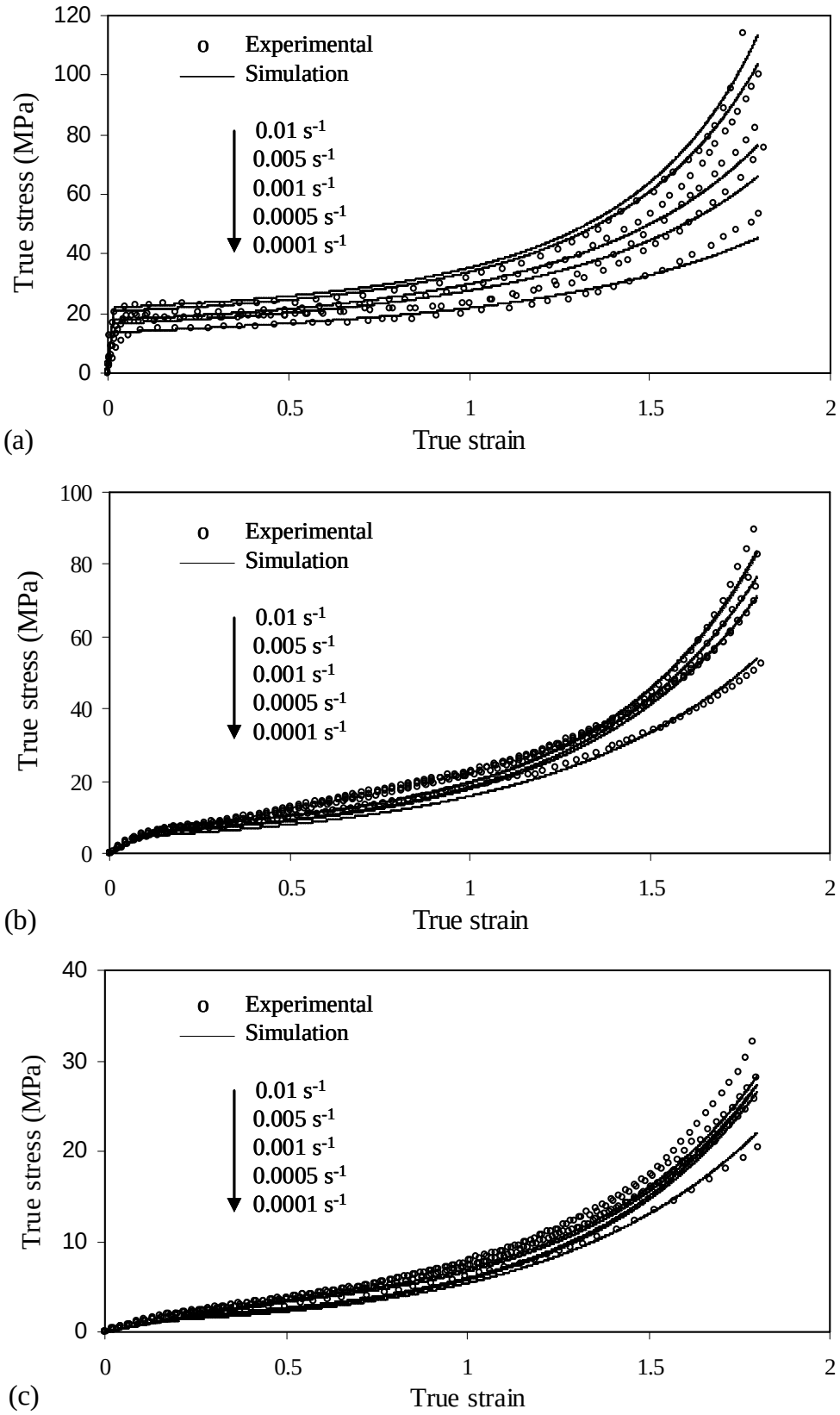

Fig. 2.8. Stress-strain curves of the MBSL1 constitutive model following the deterministic identification parameter results for different crystal volume fractions: (a) HDPE, (b) LDPE, (c) ULDPE.

I.3. Numerical strategy of direct parameter identifications

Contrary to the deterministic approach consisting in a "step-by-step" identification method, the present section details the direct analysis of the whole stress-strain data, and enabling the direct determination of the overall model parameter sets. The experimental curve fitting problem can be then formulated as an optimization search (Pyrz and Zaïri, 2007): as discussed afterwards, it thus consists in minimizing the discrepancies between experimental and numerical overall stress-strain results. Such optimization search problems manipulating mixed variables involves local optima and then require global robust search procedures: a GA identification tool has thus been developed for the present work.

I.3.1. Formulation of the optimization problem

In this section, the experimental data available for a specific material consists of N_V stress-strain curves, N_V being the number of applied strain rates. Each of these curves is deducted from a given number of experimental points, number noticed $N_{P,L}$ for the L^{th} velocity, i.e. $1 \le L \le N_V$. Hence, the behavior of a tested material is described by a database of experimental stress values noticed $T_{L,K}^{Exp}$, where $1 \le L \le N_V$ and $1 \le K \le N_{P,L}$.

Then, let us call $T_{L,K}^{Num} = T_{L,K}^{Num}(X)$ the corresponding stress values, deducted from a constitutive model. These numerical values depend on the corresponding constitutive model variables set, i.e. $X = \{E; \Delta G; s; C_r; N_r; C\}$ for the BSL constitutive model and $X = \{E_c; E_a; \Delta G_c; \Delta G_a; s_c; s_a; C_r; N_r; C\}$ for the MBSL1 constitutive model. X can be viewed as a design parameter set to optimize. In that way, the identification problem taken into consideration consists to minimize the gap between the experimental $T_{L,K}^{Exp}$ and numerical $T_{L,K}^{Num}$ stresses, measured at the same strain rate. Following the approach presented by Pyrz and Zaïri (2007), the identification problem consists to minimize the average discrepancy,

normalized with respect to the $N_{P,L}$ points of the N_V experimental stress-strain curves. By this means, a reasonable objective function, to be minimized, can be formulated as:

$$f(X) = \frac{1}{N_V} \sum_{L=1}^{N_V} \left(\frac{1}{N_{P,L}} \sum_{K=1}^{N_{P,L}} \left\| T_{L,K}^{Num} - T_{L,K}^{Exp} \right\| \right) \tag{2.32}$$

It may be noticed that, as for the large majority of practical engineering optimization problems (Melanie, 1999; Miettinen et al. 1999), this non-linear formulation implies inter-dependent real and integer (i.e. continuous and discrete) variables.

I.3.2. Genetic algorithm identification tool

First, it could be underlined that the experimental databases considered for the identification of material parameters induce large number of experimental points. Moreover, the mechanical behaviors of the studied materials are strongly non-linear. Furthermore, the constitutive model parameters considered as design variables X are both real and integer parameters, leading thus to a "mixed-variables" optimization problem. At last, and due to the material model formulations detailed in Section 1, these variables are strongly inter-dependent.

By this mean, such identification problems imply local optima and non-convexity and large cardinality of the design space as mentioned by previous works of the literature (Pyrz and Zairi, 2007; Chaparro et al., 2008; Mahmoudi et al., 2001). Such practical difficulties are largely responsible for the interest granted to global stochastic methods in engineering sciences from the last decades (Goldberg, 1989; Michalewicz, 1999; Melanie, 1999; Miettinen et al., 1999). Indeed, evolutionary search, commonly used today in engineering sciences, is naturally suited and convenient to treat with mixed variables and solve multi-modal and large optimization problems. Many works (Miettinen et al., 1999) have demonstrated the reliability, the usefulness and efficiency of such procedures, allow to dealing with difficult, big size, high cardinality, continuous or discrete and non-convex

"engineering-like" search problems. In that way, such allows designing numerical tool handy and dedicated to non-specialists of mathematical optimization heuristics (Melanie, 1999; Miettinen et al., 1999). A genetic algorithm based optimization procedure has been thus designed and computed for this study.

As can be reminded, GA belongs to the general class of evolutionary algorithms (EA): they are general purpose, stochastic search methods inspired by natural evolution (Goldberg, 1989). The main idea of such optimization procedures consists in processing at a time a fixed number of potential solutions X, called population. Each of these individuals is characterized by its corresponding objective function value $f(X)$, called fitness. According to evolutionary theories, the fittest (i.e. leading to the lowest fitness) individuals are likely to form a new generation of solutions by recombining their features using a set of biologically inspired stochastic operators (Goldberg, 1989; Michalewicz, 1999). First, the selection step allows high probability to the fittest individuals among the whole population to become parents. Next, the crossover operator recombines the genetic characteristics (i.e. the optimization parameters) of selected parents, thus producing children individuals expected to improve the optimization search. Some of the children are then arbitrary transformed by the mutation operator, preventing the population to become a homogenous and to focus on a local optimum (Melanie, 1999). This simulated reproduction procedure is renewed for a fixed number of generations. At last, the GA yields the best individual (of minimal fitness) which found during this evolution process.

Numerous works of the literature, especially for optimization with discrete parameters, use binary encodings to represent the optimization parameter set X (Miettinen et al., 1999). The developed GA manipulates directly real and integer variables. The corresponding genetic operators have been chosen following recommendations of the literature (Michalewicz, 1999; Miettinen et al., 1999). Their principles are schematically illustrated in **Fig. 2.9**. As can be seen, the starting population of individuals X is randomly created. The fitness evaluation

is allowed by coupling the GA process with the experimental database and the considered constitutive model. Next, the selection step operates by tournaments between randomly chosen individuals. Besides, this selection is elitist: the best individual of the current population is automatically chosen in the following generation. The whole arithmetical crossover and the random uniform mutation are applied.

The genetic operators depend on probability levels, as reminded by the flowchart of **Fig. 2.9**. Accordingly to recommendations of the literature and preliminary tests, crossover and mutation probability of $P_{Cross} = 75$ and $P_{Mut} = 5$, respectively, have been considered in this study. The random point of crossover has been chosen to be $0 \leq \rho \leq 1.5$, using the boundary rebound technique literature (Michalewicz, 1999; Miettinen et al., 1999). For the numerical applications, the numbers of individuals and generations have been chosen accordingly to the cardinalities of each of the treated identification problems and preliminary tests. The corresponding values N_X and N_G are detailed in the following paragraphs. Besides, it should be underlined that, due to the stochastic nature of the GA process, each identification problem studied thereafter in this work has been analyzed by performing a minimum of 10 successive runs of the numerical tool depicted in **Fig. 2.9**.

I.4. Numerical identification results and discussion

The identification of constitutive model parameters has been then performed using the numerical approach, based on evolutionary optimization, detailed in the previous section.

I.4.1. Preliminary numerical tests

First, in order to validate the developed numerical identification tool, preliminary numerical tests have been carried out. The stress-strain curves under

consideration have been numerically generated using the BSL model: the objective is to re-identify the prescribed model parameters.

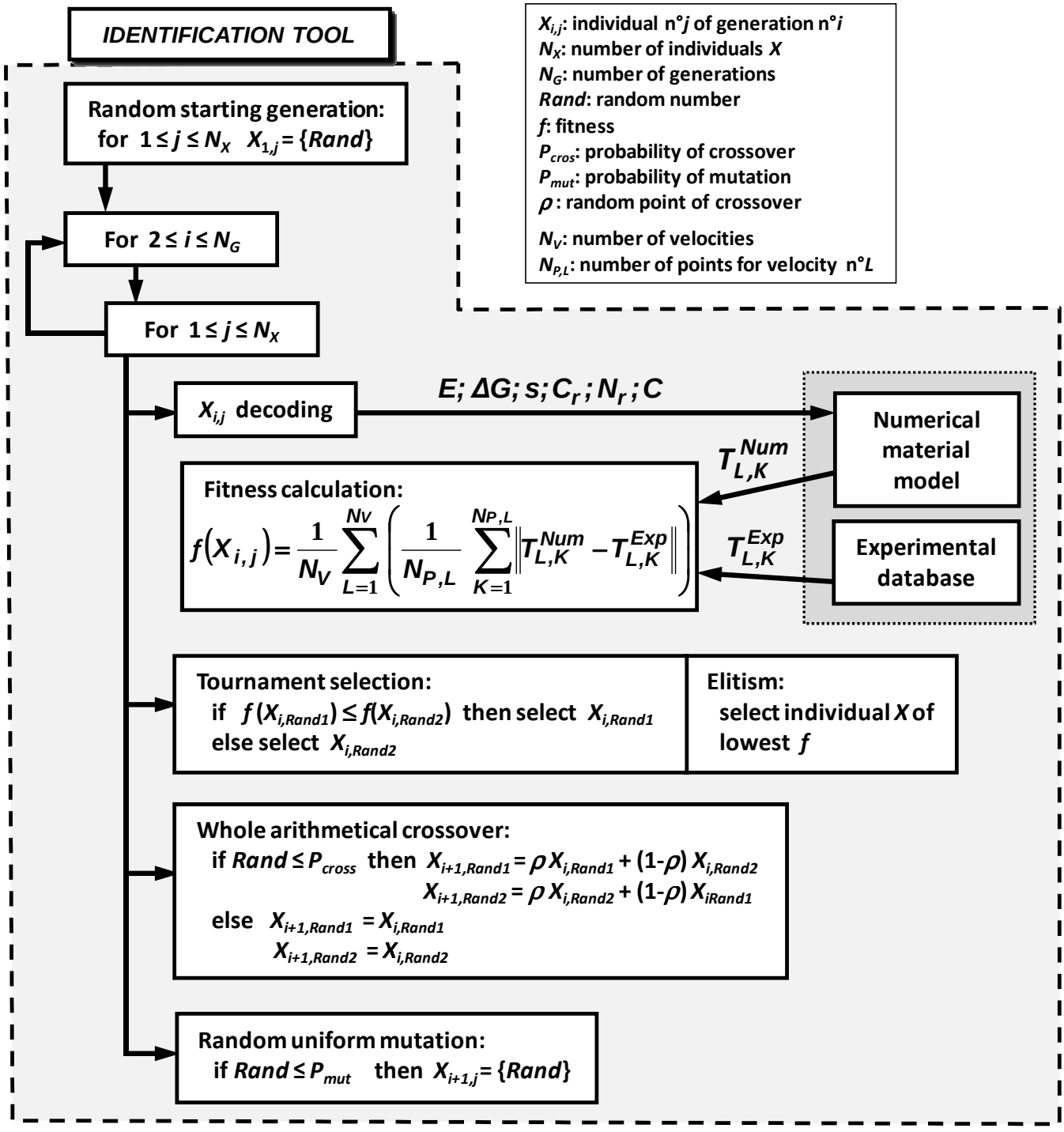

Fig. 2.9. Flowchart of the numerical identification process.

I.4.1.1. Parameter identification for static loading

The first preliminary numerical tests performed take into consideration the BSL constitutive model (see Section **I.1.1**) to re-identify the related model parameters for a given material but considering a static condition; the effect of viscosity in both intermolecular and network resistances have been then neglected. It thus allows minimizing the interdependence effects between material parameters. In that way, the material behavior is depending only on four parameters: E , s , C_r and N_r .

The prescribed fictive parameter values are presented in **Table 2.3**. Considering these parameters, a corresponding stress-strain curve has been thus numerically generated from the reduced BSL constitutive model, as previously mentioned. This curve comprising $N_{P,L}$ =400 points, plotted in **Fig. 2.10**. As mentioned previously, the effect of strain rate is hence neglected, therefore $N_V = 1$.

The robustness of the developed numerical identification tool (see **Fig. 2.9**) has been then evaluated by "re-identifying" the constitutive model parameters using this numerical stress-strain curve depicted in **Fig. 2.10**. For each material parameter, the intervals of search have been chosen. These intervals are detailed in **Table 2.4**. The numbers of generations and individuals of the GA process have been fixed to N_G =5000 and N_X =400, respectively.

For this evaluation, 100 successive runs of GA have been carried out. **Table 2.4** details the obtained results: first, the best solution, leading to the lowest fitness value f observed during the 100 runs. Moreover, the whole 100 identification results have been analyzed in terms of average values (and corresponding standard deviations), for each material parameter, as presented in **Table 2.4**.

As can be seen in **Table 2.4**, the identification procedure exhibits a perfect reproducibility: the material parameters (E , s , C_r , N_r) obtained (both for the best solution and for the average values) equate the chosen values detailed in **Table**

2.4. The corresponding standard deviations appear to be negligible. It thus demonstrates both the efficiency of the identification tool proposed and the uniqueness of the optimization solution. Moreover, it should be mentioned that all of the stress-strain curves deducted from the GA-identified parameter sets are identical and match exactly the initial one generated by using the BSL model as shown in **Fig. 2.10**.

E (MPa)	s (MPa)	C_r (MPa)	N_r
1700	27	1.8	300

Table 2.3. Preset model parameter values.

	E (MPa)	s (MPa)	C_r (MPa)	N_r	Fitness f
Best solution	1700.003174	26.99999698	1.800000087	300	1.004534495
Average value	1700.003174	26.99999684	1.800000089	300	1.004534498
Standard deviation	7.94869×10^{-7}	8.55143×10^{-7}	1.04967×10^{-8}	0	2.0179×10^{-7}
Upper limit of search	3000	200	4	500	
Lower limit of search	200	10	0.2	20	

Table 2.4. Interval of search and re-identified values of the constitutive model parameters.

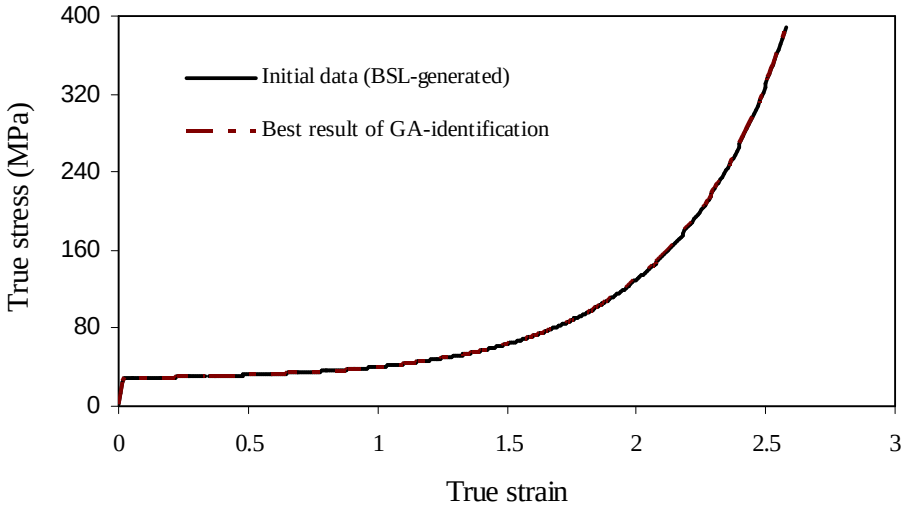

Fig. 2.10. Initial (BSL-generated) and GA-identified numerical stress-strain curves.

I.4.1.2. BSL overall parameter identification

For the second preliminary test set, the BSL constitutive model has also been considered. However, the effects of viscosity have been henceforth analyzed, unlike the previous tests discussed in Section **I.4.1.1** even the purpose being however similar: it consists to re-identify model parameters using numerical stress-strain curves generated by the BSL model. The constitutive model parameters to be re-identified are E, ΔG, s, C_r, N_r and C. It could be mentioned that the intermolecular parameters ΔG and s (see Eq. (2.16)) are interdependent with the parameter γ_0. In addition, network parameters C_r and N_r are interdependent, as can be seen in Eq. (2.17), but both are related to the viscous parameter C.

Preset of constitutive model parameters are presented in **Table 2.5**. Considering these values, corresponding stress-strain curves have been thus numerically generated using the BSL model. In order to take into account the viscosity effects, three strain rates have been considered (i.e. $N_V = 3$): 0.05, 0.005 and 0.0005 s^{-1}. These curves, plotted in **Fig. 2.12**, comprise $N_{P,L} = 400$ points. The robustness of the developed numerical identification tool (see **Fig. 2.9**) has been anew evaluated by "re-identifying" the constitutive model parameters using the stress-strain curves depicted in **Fig. 2.11**. For each material parameter, the ranges of search have been chosen sufficiently wide, as detailed in **Table 2.6**. The numbers of generations and individuals of the GA process have been settled to $N_G = 15000$ and $N_X = 450$, respectively.

20 successive runs of GA have been carried out. **Table 2.6** details the obtained results. For each material variable, the whole 20 identification results have been also analyzed in terms of best solution (exhibiting the lowest fitness value *f*), average values (and corresponding standard deviations), as presented in **Table 2.6**. The result shows non-uniqueness of identified parameters due to interdependence of parameters above mentioned. However, and for the whole

parameter solutions, the corresponding stress-strain curves are always in very good agreement with the initial ones, as the example depicted in **Fig. 2.11**.

E (MPa)	ΔG (MPa)	s (MPa)	C (MPa.s)$^{-1}$	C_r (MPa)	N_r
796	9.20×10^{-20}	71	1.3×10^{-10}	1.73	20

Table 2.5. Preset model parameter values.

	E (MPa)	ΔG (MPa)	s (MPa)	C (MPa.s)$^{-1}$	C_r (MPa)	N_r	Fitness f
Best solution	803.567	9.20×10^{-20}	72.094	2.20×10^{-9}	1.733	19	1.00349961
Average value	790.861	9.27×10^{-20}	70.971	3.92×10^{-9}	1.728	18	1.01287686
Standard deviation	129.6805	2.02×10^{-20}	23.504	2.546×10^{-9}	7.3×10^{-9}	0.99	0.00709278
Upper limit of search	1500	3×10^{-19}	150	1.00×10^{-4}	15	500	
Lower limit of search	100	10×10^{-20}	2	1.30×10^{-15}	0.1	15	

Table 2.6. Interval of search and re-identified values of the constitutive model parameters.

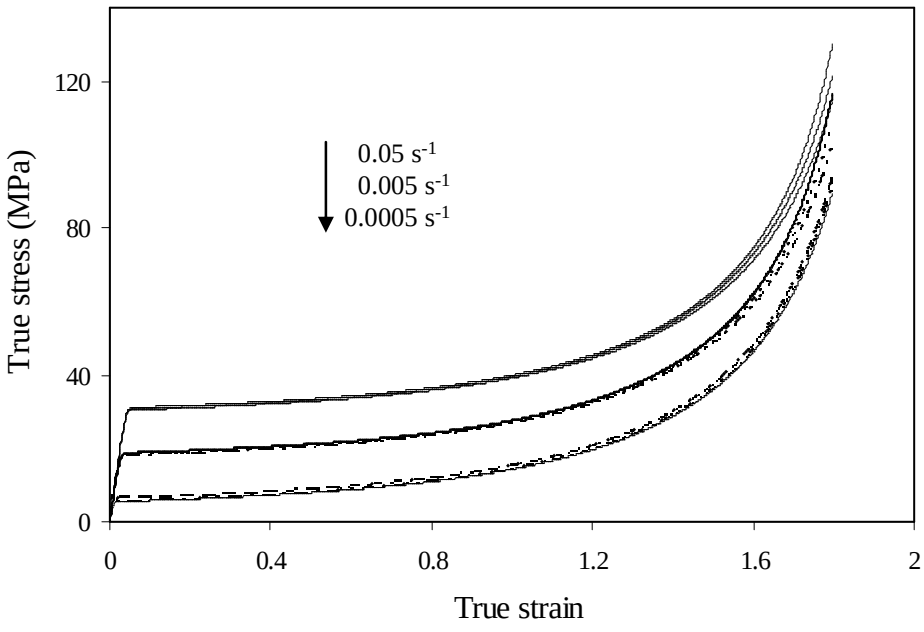

Fig. 2.11. Initial (BSL-generated), best and average solution of GA-identified numerical stress-strain curves for different strain rates.

I.4.2. Identification of BSL model parameters

The BSL constitutive model treats materials as homogenous media. Thus, each polyethylene material parameter must be identified separately; for each considered crystal contents, a set of BSL model parameters was found by using the developed numerical identification tool. The variables of the BSL constitutive model to be identified are then $X = \{E; \Delta G; s; C_r; N_r; C\}$. The model parameters to be identified and their corresponding optimization ranges (i.e. upper and lower search limits) are listed in **Table 2.7**. Numbers of generations and individuals are $N_G = 15000$ and $N_X = 490$, respectively. For each of crystal content considered, ten successive runs were also performed. As noticed previously in Section **I.4.1**, the identification tool appears to be robust, allowing an excellent reproducibility of the results: for each run, the parameter sets obtained are leading to similar fitness values. The best solutions of identified variable values are detailed in **Table 2.7** for each crystal volume fraction considered.

	E (MPa)	ΔG (J)	s (MPa)	C (MPa.s)$^{-1}$	C_r (MPa)	N_r
$\chi_{cv} = 0.72$	1188	1.25×10^{-19}	29.90	5.97×10^{-8}	2.5	20
$\chi_{cv} = 0.30$	65.3	2.83×10^{-19}	7.00	2.02×10^{-8}	2.6	44
$\chi_{cv} = 0.15$	6.4	1.29×10^{-19}	1.57	4.26×10^{-8}	1.2	70
Upper limit of search	1500	3.45×10^{-19}	50	1.0×10^{-3}	3.1	100
Lower limit of search	4	8.9×10^{-20}	0.5	1.0×10^{-10}	0.1	15

Table 2.7. Identified parameters for the BSL constitutive model and ranges of optimization search.

Fig. 2.12 presents the simulated stress-strain curves, obtained using the identified parameters, and the experimental stress-strain curves. A good agreement between experiments and BSL constitutive model can be observed. It is worth noticing that all the GA-identified material parameters do not evolve monotonically with respect to the crystal content, due to unrestricted limit of

research. Thus, the numerical identification tool allows optimizing parameters led to best fit with the experimental data compared to the deterministic method.

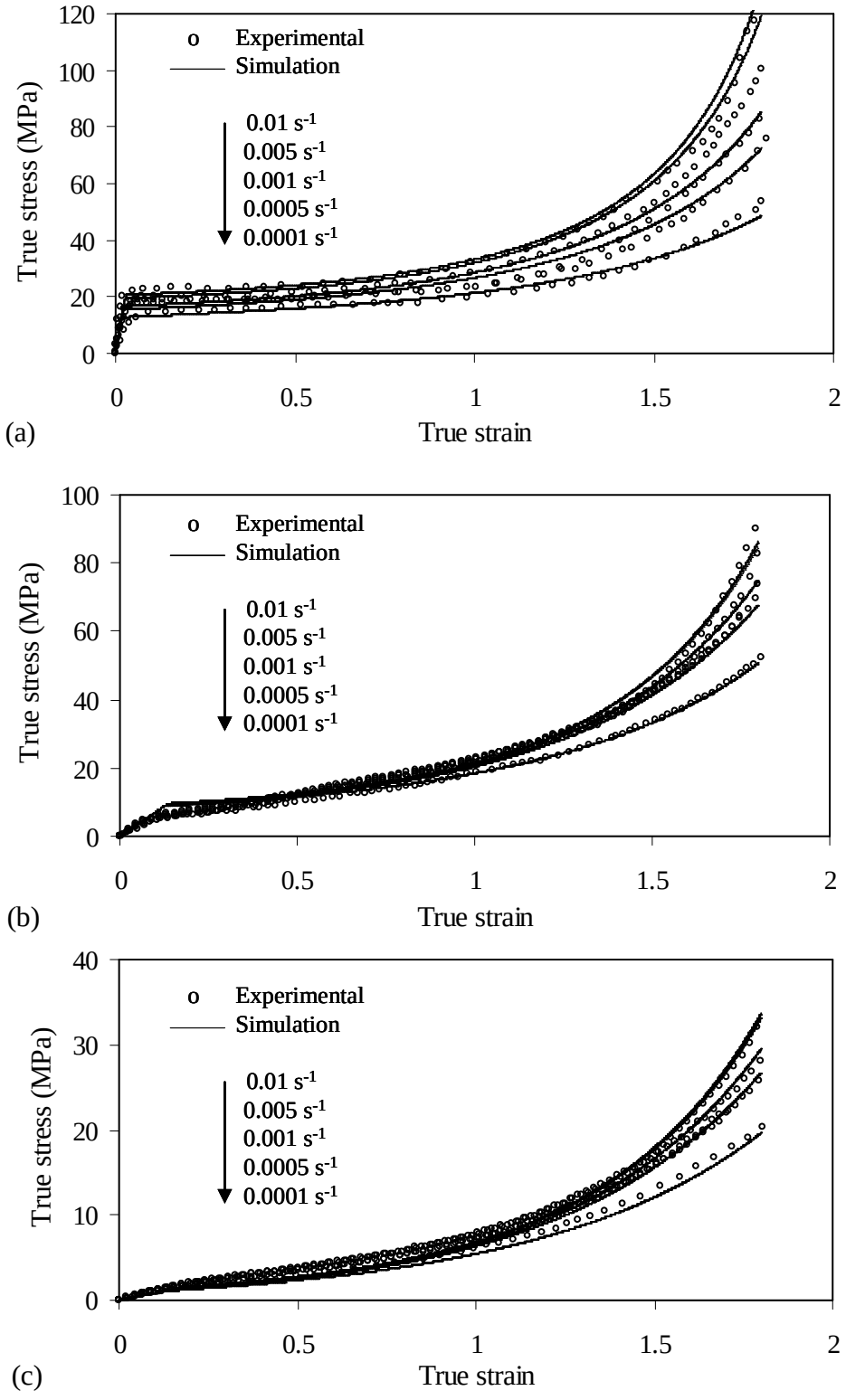

Fig. 2.12. Stress-strain curves of the BSL constitutive model following the GA identification parameter results for different crystal volume fractions: (a) HDPE, (b) LDPE, (c) ULDPE.

I.4.3. Identification of MBSL1 model parameters

As can be reminded, the MBSL1 constitutive model considers semi-crystalline materials as heterogeneous media by taking the crystal volume fraction as unique variable. Similarly at the approach detailed in the previous Section **I.4.2**, the MBSL1 material parameter set X has been identified using the proposed identification procedure. The crystalline and amorphous Young's moduli, E_c and E_a, and the interaction parameter κ were not numerically identified but fixed according to deterministic values. Thus, the optimization problem consists to identify the parameter set $X = \{\Delta G_c; \Delta G_a; s_c; s_a; C_r; N_r; C\}$.

The inter-dependencies between crystalline and amorphous phases play in different ways in the branches *A* and *B* of the MBSL1 model (see **Fig. 2.4**). The effect of the crystal volume fraction χ_{cv} can be identified and then adjusted for the viscoplastic behavior (branch *A*) by opposition to the visco-hyperelastic response (branch *B*) where only macroscopic data can be analyzed. The parameters of the viscoplastic branch *A* $\{\Delta G_c; \Delta G_a; s_c; s_a\}$ and of the visco-hyperelastic branch *B* $\{C_r; N_r; C\}$ have been identified using merely the experimental data of polyethylene with 0.72 crystal volume fraction. **Table 2.8** indicates the upper and lower bounds of the search of each corresponding parameter. Note that the parameters $\{C_r; N_r; C\}$ evolve according to the deterministic kinetics given in **Fig. 2.7**. Numbers of generations and individuals are N_G = 15000 and N_X = 490, respectively. 10 successive runs of the identification tool have been performed. **Table 2.8** provides the fittest result obtained for the parameter set $X = \{\Delta G_c; \Delta G_a; s_c; s_a; C_r; N_r; C\}$. **Fig. 2.13** presents the identification result in terms of stress-strain curves on the polyethylene material containing 72 % of crystal phase, and the model predictions for the two other crystal volume fractions (0.30 and 0.15). The global response is well reproduced by the model but

it may be also remarked that the strain rate dependence is not well captured for the lowest crystal volume fractions.

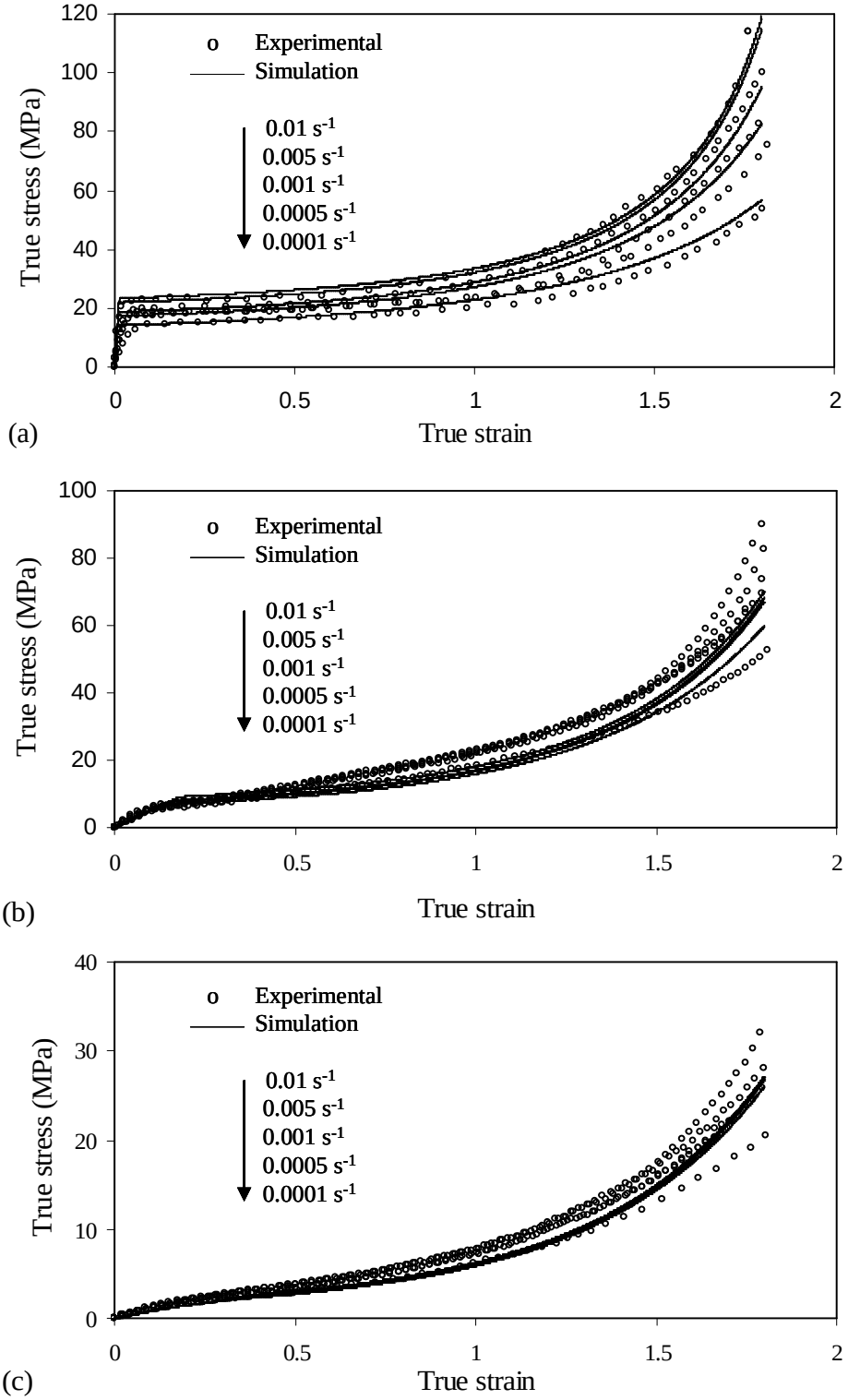

Fig. 2.13. Stress-strain curves of the MBSL1 constitutive model following the GA identification parameter results for different crystal volume fractions: (a) HDPE, (b) LDPE, (c) ULDPE.

	ΔG_c (J)	ΔG_a (J)	s_c (MPa)	s_a (MPa)	C (MPa.s)$^{-1}$	C_r (MPa)	N_r
Identified values	1.51×10^{-19}	3.59×10^{-19}	84.45	0.5	1.88×10^{-08}	2	20
Upper limit of search	2.76×10^{-19}	2.76×10^{-19}	150	90	1×10^{-03}	15	600
Lower limit of search	6.90×10^{-20}	9.66×10^{-20}	20	0.1	1×10^{-15}	0.1	15

Table 2.8. Identified parameters of the MBSL1 constitutive model and ranges of search. The identification is performed using the polyethylene experimental data of with 0.72 crystal volume fraction (HDPE).

I.5. Partial conclusions

This part is dedicated to the constitutive modeling of semi-crystalline polymers and to strategies of parameters identification. The large-strain viscoelastic-viscoplastic framework was used to capture the thermoplastic/ elastomeric transition of the polyethylene mechanical response. Two modeling strategies were used. In the first one, the semi-crystalline material was considered as a homogeneous medium, and a set of model parameters were associated at each crystal fraction. In the second one, a two-phase representation of the semi-crystalline material was considered by distinguishing the amorphous and the crystalline domains, the only one set of model parameters was required. The model parameters were identified by providing two strategies: (i) the classical analytical deterministic method, proceeding by "step-by-step" parameter analysis; (ii) the numerical identification tool, enabling to directly identify the whole parameter sets following an evolutionary optimization approach. For the two constitutive models, the identified parameter sets obtained led to stress-strain evolutions correctly matching the experimental data.

The numerical identification tool developed appears to be a useful, simple and reliable technique. Indeed, the process allowed us to directly obtain the whole

parameter sets, in contrast to the deterministic one, which processes "step-by-step" to determine successively the different parameters.

Moreover, using the MBSL1 constitutive model, the numerical identification approach appears to be predictive: the polyethylene mechanical response with different crystallinities can be deducted from the parameters identification of only one material crystal fraction.

In the next part, we propose to incorporate the crystal rate effect into the intermolecular and network resistance of the BSL constitutive model. The resulting model is referred to MBSL2 constitutive model.

II. Formulation and identification of an improved model

This part is organised as follows: In Section **II.1**, the MBSL2 constitutive model is peresented. In Section **II.2**, the numerical identification results are given. In Section **II.3**, the results of the MBSL2 constitutive model are compared with experimental data. In Section **II.4**, concluding remarks are given.

II.1. MBSL2 constitutive model

Considering that plastic flow as well microstructure alignment in semi-crystalline polymers can be attributed to overcome resistances in both amorphous and crystalline phases. We propose in this section a further extension of the BSL constitutive model, as shown in **Fig. 2.14**. The constitutive model eferred to MBSL2 constitutive model considers essentially the stress-strain behavior as a result of resistances acting in parallel: (A) two (amorphous and crystalline) intermolecular resistances and (B) two (alignment and fragmentation) network resistances. A coupling between the crystalline and the amorphous phases is explicitly considered in both resistances, which makes a valuable difference with the previous model. The intermolecular resistances are represented by linear springs in series with nonlinear dashpots. The linear springs depict the initial

elastic response of the amorphous and the crystalline phases, whereas the viscoplastic behavior is described by the viscous elements. The amorphous network resistance is represented by a Langevin spring in series with a nonlinear dashpot. The Langevin spring corresponds to the amorphous network resistance whereas the viscous element reproduces the amorphous relaxation processes. The crystalline phase contribution in the microstructure alignment resistance is introduced by using a high stiff spring.

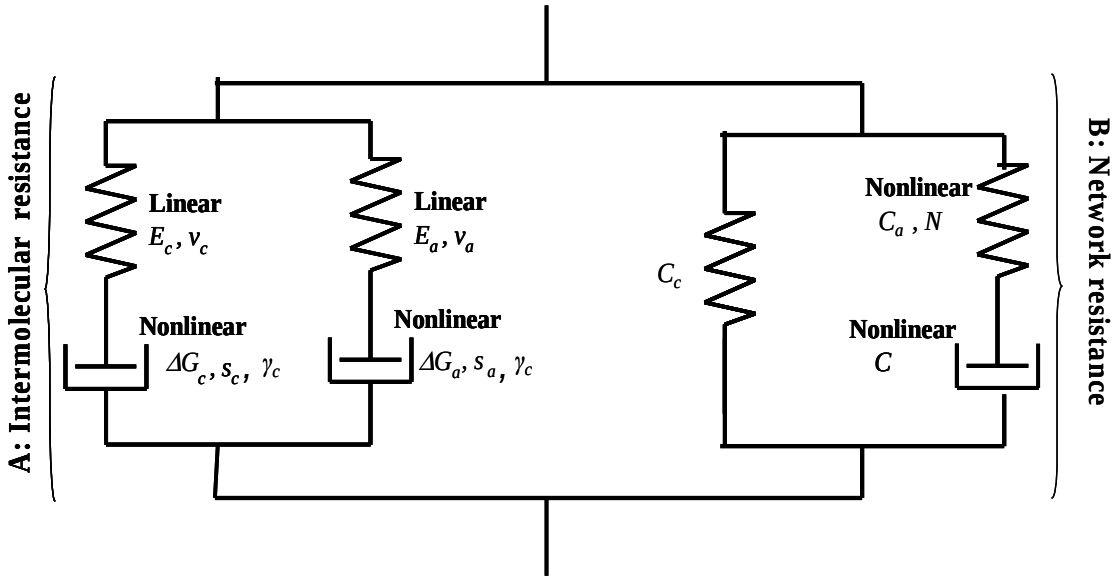

Fig. 2.14. Rheological representation of the MBSL2 constitutive model.

II.1.1. Resistance A: intermolecular resistance

The resistance A in MBSL2, as depicted in **Fig. 2.14,** is the same as the resistance A of MBSL1. The β parameter in Eq. (2.21) is replaced by β_I. In addition, we neglect the κ parameter in Eq. (2.28).

II.1.2. Resistance B: network resistance

The strain hardening response may be attributed to both molecular and crystallographic orientations, thus we propose to treat the effect of the crystalline and amorphous phases individually as following:

I) Amorphous phase in the resistance *B*: the stress-strain relationship in the amorphous phase during the strain hardening stage can be described using the same resistance in BSL constitutive model in Section **I.1.1.2**.

(II) Crystalline phase in the resistance *B*: during the strain hardening stage, the crystalline domains involve several elementary microstructural deformation mechanisms, which are complex to model. Considering the crystalline phase stiffness as a first-order factor in the microstructure alignment resistance, a simple Neo-Hookean formulation is used to represent the Cauchy stress in the crystalline phase:

$$\mathbf{T}_{Bc} = J_{Bc}^{-1} 2C_c \mathbf{B}_c \tag{2.33}$$

in which J_{Bc} is crystal network volume change, C_c is a constant and $\mathbf{B}_c$ is the crystal left Cauchy-Green tensor: $\mathbf{B}_c = \mathbf{F}_{Bc}\mathbf{F}_{Bc}^T$. The fragmentation process having an effect on the crystalline domain perfection, the crystal stiffness is expected to be degraded and the C_c value to be lower than the crystal elastic modulus value in the intermolecular resistance.

The effects of both phases are summed to determine the network Cauchy stress $\mathbf{T}_B$:

$$\mathbf{T}_B = \left(\chi_{cv}\right)^{\beta_N} \mathbf{T}_{Bc} + \left(1-\chi_{cv}\right)^{\beta_N} \mathbf{T}_{Ba} \tag{2.34}$$

where χ_{cv} is again the crystal volume fraction and β_N is introduced to take into account the network mechanical interactions between the two phases.

II.2. Numerical identification of parameters

Numerical approach, based on evolutionary optimization, detailed in the Section **I.3**, it found to be very satisfying to identify the constitutive model parameters, thus identification of constitutive model parameters has been then performed using the same numerical tool approach. Thus the same formulation of the optimization problem has been used unless the objectives function. The

objective function (involves finding the best set of parameters, which are matching the experimental data to numerical constitutive model results) is found to be as following:

$$X = \{E_a, E_c, \Delta G_a, \Delta G_c, s_a, s_c, C, N, C_a, C_c\} \tag{2.35}$$

II.3. MBSL2 constitutive model results vs. experimental data

The sensitivity to the crystallinity effects of the constitutive model proposed in this part has been then evaluated. In that way, the identification of the model parameters has been treated considering the mechanical behavior dominated either by the crystalline, or by the amorphous phase: HDPE and ULDPE materials, respectively. This optimization problem, achieved using the numerical tool illustrated in **Fig. 2.9**, is thus based on the ten experimental stress-strain curves depicted in **Fig. 2.15-a** and **Fig. 2.15-c**. The elastic properties of the crystalline and amorphous phases are prescribed; the values are those given in Section **I.2.2**. In addition, the interaction parameters β_I and β_N have been identified for the HDPE and ULDPE materials using the same numerical optimization tool. The model parameter values obtained by identification are listed in **Table 2.9**, and the corresponding interaction parameters are detailed in **Table 2.10**. The corresponding stress-strain curves deduced from the proposed constitutive model are depicted in **Fig. 2.15-a** and **Fig. 2.15-c** for the five true axial strain rates. It is interesting to note that the proposed two-phase model is able to accurately reproduce the ULDPE and HDPE mechanical responses using the parameter set reported in **Table 2.9** and the interaction parameters detailed in **Table 2.10**. As can be seen in **Fig. 2.15-a** and **Fig. 2.15-c**, the numerical and experimental curves are in good agreements. Such results confirm the relevance of both the proposed two-phase model and the identification approach.

ΔG_c (J)	ΔG_a (J)	s_a (MPa)	s_c (MPa)	C_r (MPa)	C (MPa.s)$^{-1}$	N_r	C_c (MPa)
1.29×10^{-19}	2.62×10^{-19}	6.88	190.73	1.7	1.2996×10^{-7}	202	239.13

Table 2.9. Identified crystalline and amorphous MBSL2 model parameters.

	$\chi_{cv} = 0.72$	$\chi_{cv} = 0.3$	$\chi_{cv} = 0.15$
β_I	5.8	2.9	2.8
β_N	14.1	3.9	3.7

Table 2.10. Identified intermolecular (β_I) and network (β_N) mechanical interaction parameters.

Subsequently, the optimized parameters depicted in **Table 2.9** have been used as input data in the proposed two-phase model to predict the LDPE stress-strain response. For this material, the interaction parameters were the outcome of a standard fitting procedure based on the minimization of differences between model results and experimental data. The obtained values are given in **Table 2.10**. The numerical corresponding stress-strain curves are shown in **Fig. 2.15-c** in comparison with the experimental data for the five true axial strain rates. The numerical results match the experimental data in a reasonable extent.

As can be noteced in **Fig. 2.16**, the evolutions of both interaction parameters β_I and β_N are monotonic. The proposed two-phase model (MBSL2) supposes that the crystalline and amorphous domains mechanically behave in the same manner whatever the crystal content; only the mechanical interactions between the two phases change. This is the key assumption of any micromechanical modeling. It is found that the mechanical interaction parameters, in the plastic yielding (intermolecular) and molecular stretching/orientation (network) regions, follow an exponential law with the crystal content.

The proposed constitutive model (MBSL2) can be used to estimate the large-

strain mechanical response of any semi-crystalline polymer material with a crystal fraction included in the investigated range.

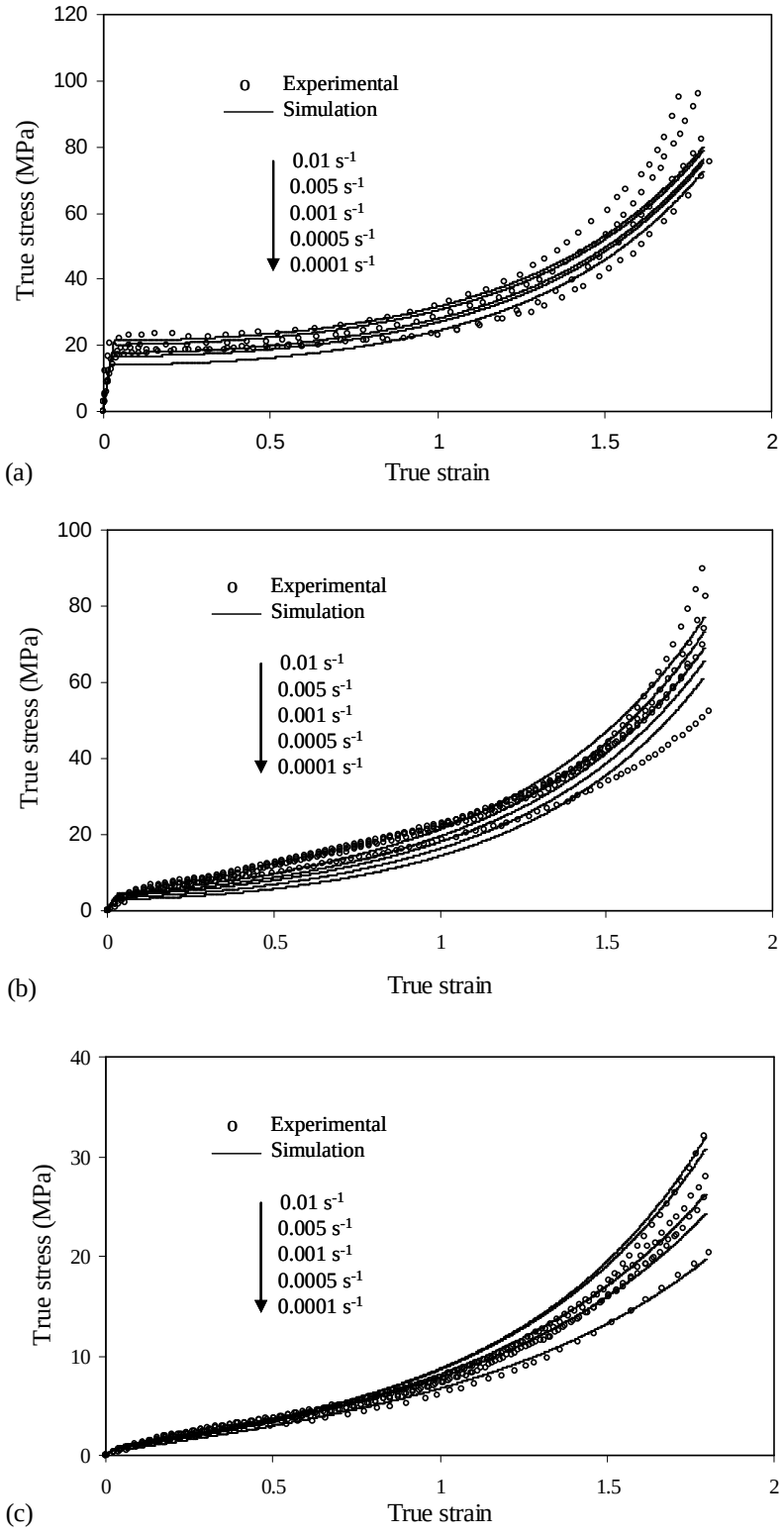

Fig. 2.15. Stress-strain curves of the MBSL2 constitutive model following the GA identification parameter results for different crystal volume fractions: (a) HDPE, (b) LDPE, (c) ULDPE.

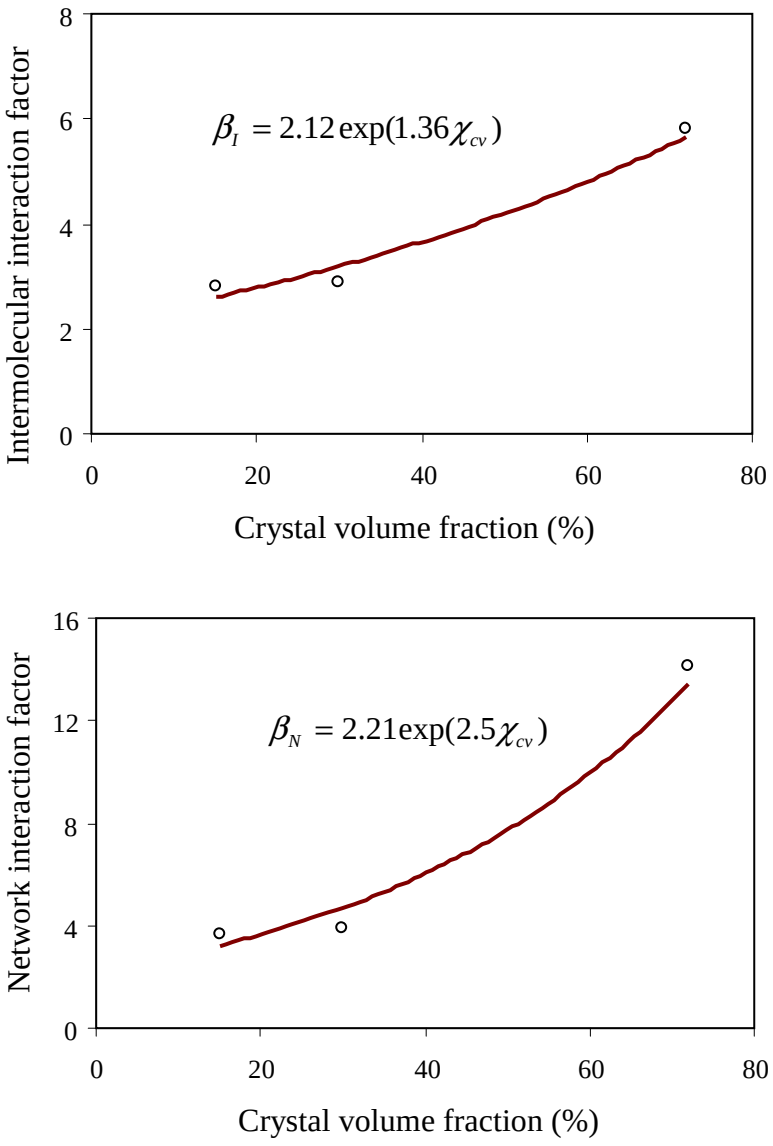

Fig. 2.16. Evolution of mechanical interaction parameters according to crystal rate.

II.4. Partial conclusions

An extention of the two-phase hyperelastic–viscoplastic constitutive model referred to MBSL2 was developed to simulate the finite deformation mechanical response of semi-crystalline polymers. This model is basically decomposed into intermolecular resistance and microstructure alignment resistance, by considering explicitly the contribution of the crystalline and amorphous phases. The model parameters were deduced using the numerical identification tool described in Section **I.3**. This approach was employed to examine the three

grades of polyethylene materials exhibiting a wide variety of crystal rate. The obtained results demonstrated the significance and the accuracy of the MBSL2 constitutive model. It could be underlined that the number of constitutive model parameters reduced significantly compared to the MBSL1 constitutive model and enables to simulation of the general trends of the polyethylene mechanical response of the studied polyethylene grades.

REFERENCES:

Abdul-Hameed, H., Messager, T., Zaïri, F., Naït-Abdelaziz, M., 2014. Large-strain viscoelastic-viscoplastic constitutive modeling of semi-crystalline polymers and model identification by deterministic/evolutionary approach. Computational Materials Science. 90, 241-252.

Ahzi, S., Makradi, A., Gregory, R.V., Edie, D.D., 2003. Modelingof deformation behavior and strain induced crystallizationin poly(ethyleneterephthalate) above the glass transition temperature. Mechanics of Materials. 35, 1139-1148.

Andrade-Campos, A., Thuillier, S., Pilvin, P., Teixeira-Dias, F., 2007. On the determination of material parameters for interval thermoelastic-viscoplastic constitutive models. International Journal of Plasticity. 23, 1349-1379.

Arruda, E.M., Boyce, M.C., 1993. Athree-dimensionalconstitutive model for the large stretch behavior of rubber elastic materials. Journal of the Mechanics and Physics of Solids. 41, 389-412.

Anand, L., Gurtin, M.E., 2003. A theory of amorphous solids undergoing large deformations, with application to polymeric glasses. International Journal of Solids and Structures. 40, 1465-1487.

Anand, L., Ames, N.M., 2006. On modeling the micro-indentation response of an amorphous polymer. International Journal of Plasticity. 22, 1123-1170.

Ayoub, G., Zaïri, F., Naït-Abdelaziz, M., Gloaguen, J.M., 2010. Modelling large deformation behaviour under loading- unloading of semicristalline polymers: application to a high density polyethylene. International Journal of Plasticity. 26, 329-347.

Ayoub, G., Zaïri, F., Fréderix, C., Gloaguen, J.M., Naït-Abdelaziz, M., Seguela, R., Lefebvre, J.M., 2011. Effects of crystal content on the mechanical behaviour of polyethylene under finite strins: experiments and constitutive modelling. International Journal of Plasticity. 27, 492-511.

Ayoub, G., Naït-Abdelaziz, M., Zaïri, F., Gloaguen, J.M., Charrier, P., 2012. Fatigue life prediction of rubber-like materials under multiaxial loading using a continuum damage mechanics approach: Effects of two-blocks loading and R ratio. Mechanics of Materials. 52, 87-102.

Ayoub, G., Zaïri, F., Naït-Abdelaziz, M., Gloaguen, J.M., Kridli, G., 2014. A visco-hyperelastic damage model for cyclic stress-softening, hysteresis and permanent set in rubber using the network alteration theory. International Journal of Plasticity. 54, 19-33.

Bartczak, Z, Kozanecki, M., 2005. Influence of molecular parameters on high-strain deformation of polyethylene in the plane-strain compression.Part I. Stress-strain behavior. Polymer. 46, 8210-21.

Bartczak, Z., 2005. Influence of molecular parameters on high-strain deformation of polyethylene in the plane-strain compression. Part II. Strain recovery. Polymer. 46, 10339-10354.

Bardenhagen, S.G., Stout, M.G., Gray, G.T., 1997. Three-dimensional, finite deformation, viscoplastic constitutive models for polymeric materials. Mechanics of Materials. 25, 235-253.

Belbachir, S., Zaïri, F., Ayoub, G., Maschke, U., Naït-Abdelaziz, M., Gloaguen, J.M., Benguediab, M., Lefebvre, J.M., 2010. Modelling of photodegradation effect on elastic-viscoplastic behaviour of amorphous polylactic acid films. Journal of the Mechanics and Physics of Solids. 58, 241-255.

Ben Hadj Hamouda, H., Laiarinandrasana, L., Piques, R., 2007. Viscoplastic behaviour of a medium density polyethylene (MDPE): constitutive equations based on double nonlinear deformation model. International Journal of Plasticity. 23, 1307-1327.

Botto, PA., Duckett, RA., Ward, IM., 1987. The yield and thermoelastic properties of oriented poly (methyl methacrylate). Polymer. 28, 257-62.

Boyce, M.C., Parks, D.M., Argon, A.S., 1988. Large inelastic deformation of glassy polymers. Part I: Rate dependent constitutive model. Mechanics of Materials. 7, 15-33.

Boyce, M. C., Socrate, S., Llana, P. G., 2000. Constitutive model for the finite deformation stress-strain behavior of poly(ethylene terephthalate) above the glass transition. Polymer. 41, 2183-2201.

Buckley, C.P., Jones, D.C., 1995. Glass-rubber constitutive model for amorphous polymers near the glass transition. Polymer. 36, 3301-3312.

Chaparro, B. M., Thuillier, S., Menezes, L.F., Manach, P.Y., Fernandes, J. V., 2008. Material parameters identification: gradient-based, genetic and hybrid optimization algorithms. Computational Materials Science. 44,339-346.

Colak, O.U., 2005. Modeling deformation behavior of polymers with viscoplasticity theory based on overstress. International Journal of Plasticity. 21, 145-160.

Dargazany, R., Khiêm, V.N., Itskov, M., 2014. A generalized network decomposition model for the quasi-static inelastic behavior of filled elastomers. International Journal of Plasticity. 63, 94-109.

Drozdov, A. D., 2009. Mullins' effect in semicrystalline polymers. International Journal of Solids and Structures. 46, 3336-3345.

Drozdov, A. D., 2011. Multi-cycle viscoplastic deformation of polypropylene. Computational Materials Science. 50, 1991-2000.

Drozdov, A.D., Klitkou, R., Christiansen, J.de C., 2013. Cyclic viscoplasticity of semicrystalline polymers with finite deformations. Mechanics of Materials. 56, 53-64.

Dusunceli, N., and Colak, O. U., 2008. Modelling effects of degree of crystallinity on mechanical behavior of semicrystalline polymers. International Journal of Plasticity. 24, 1224-1242.

Dupaix, R.B., Krishnan, D., 2006. A constitutive model for strain-induced crystallization in poly(ethylene terephthalate) (PET) during finite strain load-hold simulations. Journal of Engineering Materials and Technology. 128, 28-33.

Frank, G.J., Brockman, R.A., 2001. A viscoelastic-viscoplastic constitutive model for glassy polymers. International Journal of Solids and Structures. 38, 5149-5164.

Franulovic, M., Basana, R., Prebil I., 2009. Genetic algorithm in material model parameters' identification for low-cycle fatigue. Computational Materials Science. 45, 505-510.

Franulovic, M., Basana, R., Robert Kunc, Prebil I., 2010. Automation of LCF material model parameters' identification. Computational Materials Science. 48, 529-536.

Gen, M., Cheng, R., 2000. Genetic Algorithms and Engineering Optimization. John Wiley.

G'Sell, C., Dahoun, A., Royer, F.X., Philippe, M.J., 1999. The influence of the amorphous matrix on the plastic hardening at large strain of semicrystalline polymers. Modelling and Simulation in Materials Science and Engineering. 7, 817-828.

Goldberg, D.E., 1989. Genetic Algorithms in Search, Optimization, and Machine Learning, 1st Ed. Addison-Wesley, Indiana.

Harth, T., Schwan, S., Lehn, J., Kollmann, F.G., 2004. Identification of material parameters for inelastic constitutive models: statistical analysis and design of experiments. International Journal of Plasticity. 20, 1403-1440.

Haward, R.N., Thackray, G., 1968. The use of a mathematical model to describe isothermal stress-strain curves in glassy thermoplastics. Proceedings of the Royal Society of London. 302, 453-472.

Lee, E.H., 1969. Elastic-plastic deformation at finite strains. Journal of Applied Mechanics. 36, 1-6.

Lee, B.J., Parks, D.M., Ahzi, S., 1993a. Micromechanical modeling of large plastic deformation and texture evolution in semi-crystalline polymers. Journal of the Mechanics and Physics of Solids. 41, 1651-1687.

Lee, B.J., Argon, A.S., Parks, D.M., Ahzi, S., Bartczak, Z., 1993b. Simulation of large strain plastic deformation and texture evolution in high density polyethylene. Polymer. 34, 3555-3575.

Machado, G., Chagnon, G., Favier, D., 2012. Induced anisotropy by the Mullins effect in filled silicone rubber. Mechanics of Materials. 50, 70-80.

Mahmoudi, A. H., Pezeshki-Najafabadi, S. M., Badnava, H., 2011. Parameter determination of Chaboche kinematic hardening model using a multi objective Genetic Algorithm. Computational Materials Science. 50, 1114-1122.

Makradi, A., Ahzi, S., Gregory, R.V., Edie, D.D., 2005. A two-phase self-consistent model for the deformation and phase transformation behavior of polymers above the glass transition temperature: application to PET. International Journal of Plasticity. 21, 741-758.

Melanie, M., 1999. An Introduction to Genetic Algorithms, 5th Ed. Massachusetts Institute of Technology, Cambridge, Massachusetts, London.

Michalewicz, Z., 1999. Genetic Algorithms + Data Structures= Evolution Programs. Springer.

Miettinen, K., Neittaanmaki, P., Makela, M. M., Périaux, J., 1999. Evolutionary Algorithms in Engineering and Computer Science. John Wiley.

Nikolov, S., Lebensohn, R.A., Raabe, D., 2006. Self-consistent modeling of large plastic deformation, texture and morphology evolution in semi-crystalline polymers. Journal of the Mechanics and Physics of Solids. 54, 1350-1375.

Pyrz, M., Zaïri, F., 2007. Identification of viscoplastic parameters of phenomenological constitutive equations for polymers by deterministic and evolutionary approach. Modelling and Simulation in Materials Science and Engineering. 15, 85-103.

Regrain, C., Laiarinandrasana, L., Toillon, S., Saı, K., 2009. Multi- mechanism models for semi-crystalline polymer: constitutive relations and finite element implementation. International Journal of Plasticity. 25, 1253-1279.

Richeton, J., Ahzi, S., Vecchio, K.S., Jiang, F.C., Makradi, A., 2007. Modeling and validation of the large deformation inelastic response of amorphous polymers over a wide range of temperatures and strain rates. International Journal of Solids and Structures. 44, 7938-7954.

Rozanski, A., Galeski, A., 2013. Plastic yielding of semicrystalline polymers affected by amorphous phase. International Journal of Plasticity. 41, 14-29.

Tervoort, T.A., Smit, R.J.M., Brekelmans, W.A.M., Govaert, L.E., 1997. A constitutive equation for the elasto-viscoplastic deformation of glassy polymers. Mechanics of Time-Dependent Materials. 1, 269-291.

Tomita, Y., Tanaka, S., 1995. Prediction of deformation behavior of glassy polymers based on molecular chain network model. International Journal of Solids and Structures. 32, 342-3434.

Tomita, Y., Nakata, S., Honma, T, Yashiro K., 2013. Deformation behavior of silica-filled rubber with coupling agents under monotonic and cyclic straining. International Journal of Mechanical Sciences. 86, 7-17 .

van Dommelen, J.A.W., Parks, D.M., Boyce, M.C., Brekelmans, W.A.M., Baaijens, F.P.T., 2003. Micromechanical modeling of the elasto-viscoplastic behavior of semi crystalline polymers. Journal of the Mechanics and Physics of Solids. 51, 519-541.

Wu, P.D., van der Giessen, E., 1995. On neck propagation in amorphous glassy polymers under plane strain tension. International Journal of Plasticity. 11, 211-235.

Yashiro, K. , Naito, M., Ueno, S., Jie, F., 2010. Molecular dynamics simulation of polyethylene under cyclic loading: Effect of loading condition and chain length. International Journal of Mechanical Sciences. 52, 136-145.

Zaïri, F., Naït-Abdelaziz, M., Woznica, K., Gloaguen, J.M., 2005. Constitutive equations for the viscoplastic-damage behaviour of a rubber-modified polymer. European Journal of Mechanics A/Solids. 24, 169-182

Zaïri, F., Aour, B., Gloaguen, J.M., Naït-Abdelaziz, M., Lefebvre, J.M., 2006. Numerical modelling of elastic-viscoplasticequal channel angular extrusion process of a polymer. Computational Materials Science. 38, 202-216.

Zaïri, F., Naït-Abdelaziz, M., Gloaguen, J.M., Lefebvre, J.M., 2010. Constitutive modelling of the large inelastic deformation behaviour of rubber-toughened poly(methyl methacrylate): effects of strain rate, temperature and rubber-phase volume fraction. Modelling and Simulation in Materials Science and Engineering. 18, 1-22.

Chapter three

FINITE ELEMENT SIMULATIONS: APPLICATIONS TO MULTI-LAYERED POLYETHYLENE SPECIMENS

This chapter is divided into four parts. Part I focuses on the finite element (FE) implementation of the MBSL1 constitutive model. The FE implementation is performed mainly to dispose a tool to investigate multi-layered polyethylene specimens.

In part II, FE calculations are performed on the three polyethylene specimens (HDPE, LDPE, and ULDPE), studied in chapter two. The simulation results are compared to experimental data in terms of load-displacement curves and neck evolution.

In two next parts, multi-layered polyethylene specimens, made of polyethylene with different crystal fraction are examined. In part III, bi-layered polyethylene specimens (a HDPE layer stratified with a LDPE layer or a ULDPE layer) are simulated and compared to experimental results. The effect of the HDPE proportion in the necking development is studied.

In part IV, multi-layered polyethylene notched round bars with different curvature radii are simulated to investigate the stress triaxiality ratio effect.

I. Finite element implementation

In this part, the implementation into a finite element of the large-strain viscoelastic-viscoplastic constitutive modelling is presented. The MBSL1 constitutive model developed in chapter two (with its identified parameters by means of GA) is used to illustrate the method. The commercial FE software MSC.Marc® is provided with a significant number of standard procedures, i.e. user subroutines, for the implementation of user-proposed models. Besides, making a choice between

subroutines depends strongly on the problem to be analysed and on the way the mechanical model is formulated (Smith, 1994). In our case, a viscoplasticity and generalized plasticity user subroutine UVSCPL subroutine was employed. This subroutine allows the implementation of an elasto-viscoplastic model by computing of the inelastic strain increment. Moreover, the user must define the inelastic strain and the stress increment. Note that this routine allows very general material constitutive laws to be selected. Thus, the subroutine allows the encoding of the proposed constitutive model for semi-crystalline polymers and the prediction of the large-strain viscoelastic–viscoplastic behavior of semi-crystalline polymers. Furthermore, the subroutine allows handling the mechanical behavior of polyethylene materials with a variable crystal volume fraction, as used in this work.

On the other hand, adding a parallel user subroutine INTCRD that makes the integration point coordinates in the reference configuration available at each increment, the multilayer simulation has been developed. The MBSL1 constitutive model was implemented into a user subroutine. A summary of the main steps of the FE subroutine, in form of a flow chart, is depicted in **Fig. 3.1**.

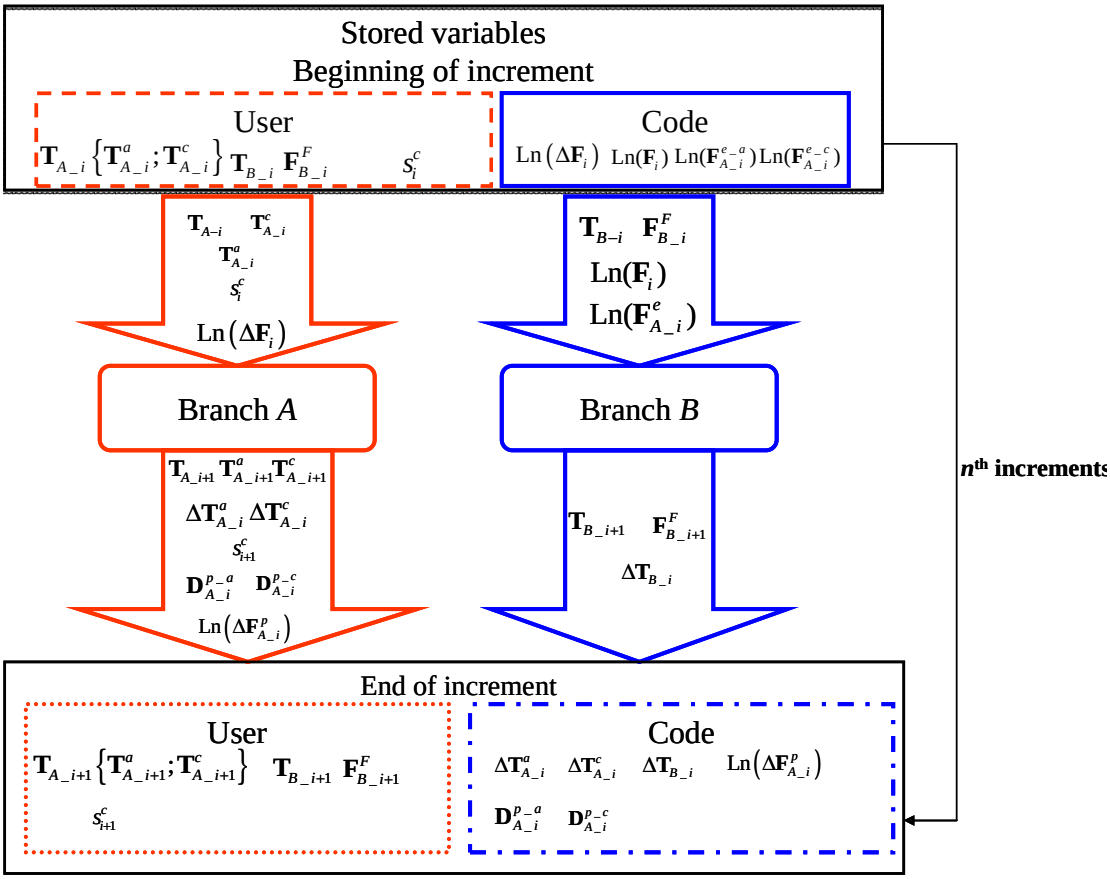

Fig. 3.1. FE subroutine flow chart of the MBSL1 constitutive model algorthim.

In this chart, the subscripts i and $i + 1$ denote the variable values at the start and at the end of the time step at the nth increment, respectively. A significant number of variables can be called at the beginning of the increment, indicated in blue bold line ($\mathrm{Ln}(\Delta\mathbf{F}_i)$, $\mathrm{Ln}\mathbf{F}_i$, $\mathrm{Ln}\mathbf{F}_{A\_i}^{e-a}$ and $\mathrm{Ln}\mathbf{F}_{A\_i}^{e-c}$), whereas at the end of the same increment the code requests the writing of exit variables by the user, indicated in blue dot-dashed line. In our case, the required exit variables must be written in an incremental or time-rate manner, i.e. $\Delta\mathbf{T}_{A\_i}^{c}$, $\Delta\mathbf{T}_{A\_i}^{a}$, $\Delta\mathbf{T}_{B\_i}$, $\mathrm{Ln}\left(\Delta\mathbf{F}_{A\_i}^{p}\right)$, $\mathbf{D}_{A\_i}^{p-c}$ and $\mathbf{D}_{A\_i}^{p-a}$. In addition to the stored variables by the FE code, some additional variables need to be stored by the user (the number of variables depend on the constitutive model). Regarding the evolution of the constitutive model intrinsic variables and the incremental character of the numerical code exit variables, the stored set of variables at the end of each increment ($\mathbf{T}_{A\_i+1}\left\{\mathbf{T}_{A\_i+1}^{a};\mathbf{T}_{A\_i+1}^{c}\right\}$, $\mathbf{T}_{B\_i+1}$, $\mathbf{F}_{B\_i+1}^{F}$, and s_{i+1}^{c}) which will

be called at the beginning of the next increment ($\mathbf{T}_{A\_i}\left\{\mathbf{T}^{a}_{A\_i};\mathbf{T}^{c}_{A\_i}\right\}, \mathbf{T}_{B\_i}$, $\mathbf{F}^{F}_{B\_i}$, s^{c}_{i}) are indicated in red dot line and dashed line, respectively. These user variables have been stored on a [*m*, *nn*, *t*] matrix where *m* is the element number, *nn* is the node and *t* is the tensor direction number. In order to calculate the total Cauchy stress $\mathbf{T} = \mathbf{T}_A + \mathbf{T}_B$, it needs to calculate the Cauchy stress of both branches *A* and *B*. The main steps concerning the numerical calculation of the Cauchy stress for both branches *A* and *B* are presented in **Fig. 3.2**.

The Cauchy stress of branch *A*, consisting of an amorphous and a crystal phase, is calculated at the nth increment from Eq. (2.21). Firstly, we need to calculate the current elastic deformation gradients of both amorphous $\mathrm{Ln}\mathbf{F}^{e-a}_{A\_i}$ and crystal $\mathrm{Ln}\mathbf{F}^{e-c}_{A\_i}$ phases. De Souza Neto et al. (2008) proposed a numerical expression to calculate the elastic deformation gradient, which can be written for the amorphous phase as:

$$\mathbf{F}^{e-a}_{A\_i} = \exp(\mathrm{Ln}(\mathbf{F}^{e-a}_{A\_i})) = \sum_{j=0}^{\infty} (1/\mathrm{j}!)\ (\mathrm{Ln}(\mathbf{F}^{e-a}_{A\_i}))^{j} \tag{3.1}$$

and for the crystal phase as:

$$\mathbf{F}^{e-c}_{A\_i} = \exp(\mathrm{Ln}(\mathbf{F}^{e-c}_{A\_i})) = \sum_{j=0}^{\infty} (1/\mathrm{j}!)\ (\mathrm{Ln}(\mathbf{F}^{e-c}_{A\_i}))^{j} \tag{3.2}$$

where $\mathrm{Ln}\mathbf{F}^{e-a}_{A\_i}$ and $\mathrm{Ln}\mathbf{F}^{e-c}_{A\_i}$ can be requested at the beginning of the increment. The current elastic deformation of branch *B* can be calculated from the expression $\mathbf{F}^{N}_{B\_i} = \mathbf{F}_i\ (\mathbf{F}^{F}_{B\_i})^{-1}$, where $\mathbf{F}_i$ is the total deformation gradient that can be requested from the numerical code at the beginning of the increment and $\mathbf{F}^{F}_{B\_i}$ is the plastic deformation gradient of the branch *B* that was stored at the end of the last increment and that can be called at the beginning of the current one. The equation to update $\mathbf{F}^{F}_{B\_i+1}$ is given by:

$$\mathbf{F}^{F}_{B\_i+1} = (\mathbf{D}^{F}_{B\_i+1}\mathbf{F}^{F}_{B\_i})\Delta t + \mathbf{F}^{F}_{B\_i} \tag{3.3}$$

where $\mathbf{D}^{F}_{B\_i+1}$ is the plastic stretching rate at the end of the increment and Δt is the time increment.

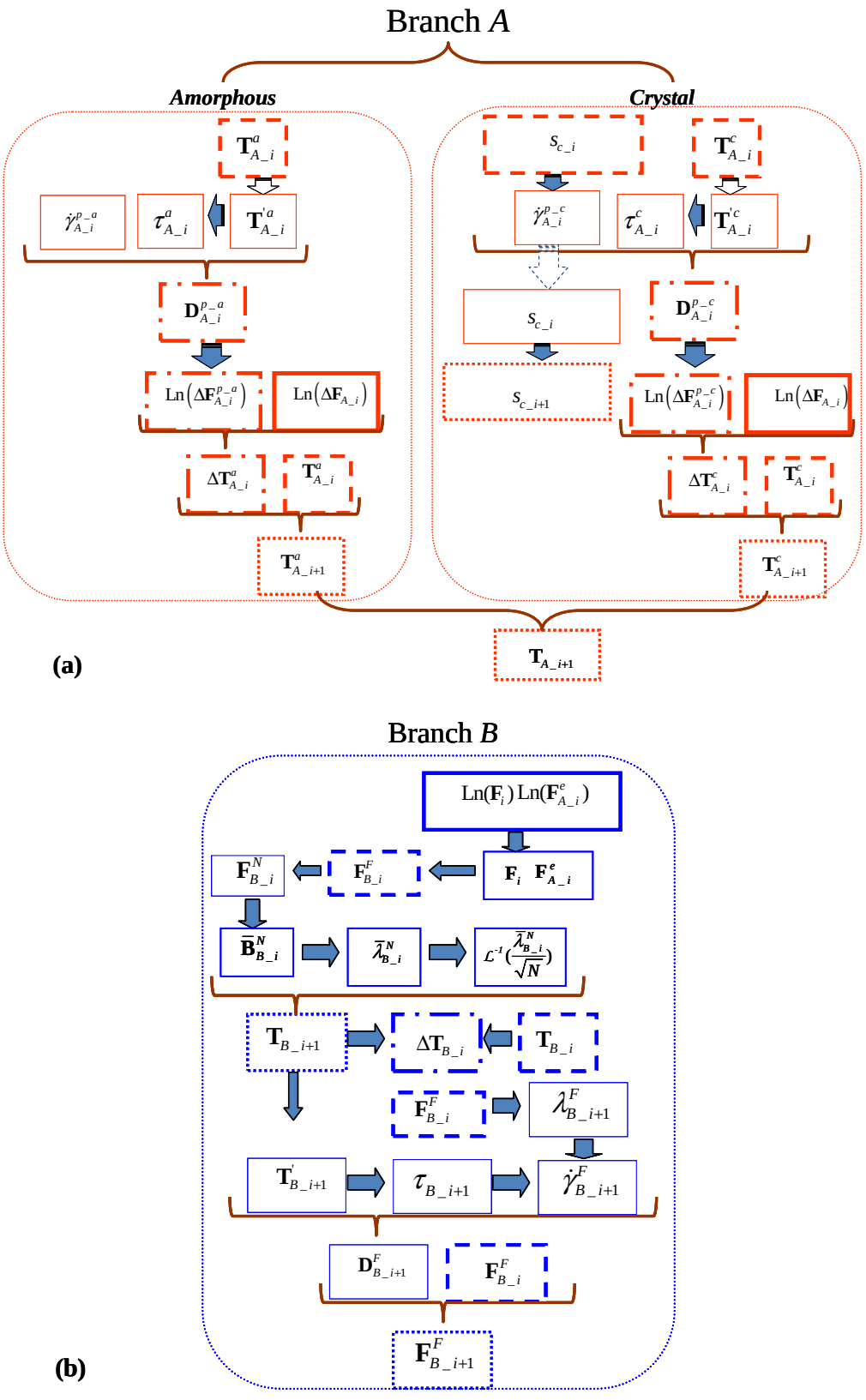

Fig. 3.2. Subroutine flow chart of FE algorithm, (a) branch *A*, (b) branch *B*.

In aforementioned MBSL1 constitutive model, the crystal and amorphous shears stresses s_c and s_a respectively, are supposed to be constant. To capture the strain softening (induced by neck instability in HDPE), only the crystal shear stress is assumed to evolve with plastic straining according to the following equation:

$$\dot{s}_c = h(1 - s_c / ss_c)\dot{\gamma}^{p-c} \tag{3.4}$$

in which h is the rate of yield drop with respect to plastic strain, ss_c is the saturation value of s_c, and $\dot{\gamma}^{p-c}$ is the plastic shear strain rate.

The equation to update s_{c_i+1} is required only for HDPE and multi-layered polyethylene, and is given by:

$$s_{c\_i+1} = \dot{s}_{c\_i}\Delta t + s_{c\_i} \tag{3.5}$$

where $\dot{s}_{c\_i}$ is the shear strength rate of the current time step. Note that, s_{c_i} was saved at the end of the last increment.

II. Finite element analysis of polyethylene

Simulations have been calculated to analyze the global-local behavior of the polyethylene materials. The constitutive model parameters for polyethyelene materials, used as input data in the subroutine, were identified in chapter two by the GA optimization tool. For convenience, the constitutive model parameters are reminded in **Table 3.1**.

E_c (MPa)	E_a (MPa)	ΔG_c (J)	ΔG_a (J)	s_c (MPa)	s_a (MPa)	C (MPa.s)$^{-1}$	C_r (MPa)	N_r
4500	4.5	1.51×10^{-19}	3.59×10^{-19}	84.45	0.5	1.88×10^{-08}	2	20

Table 3.1. Constitutive model parameters used as input data for simulations.

II.1. Simulation model

The tensile tests conducted and presented in **Fig. 1.6** (see chapter one) for the three polyethylene materials (HDPE, LDPE, and ULDPE) have been simulated. As mentioned before, HDPE is characterized by neck instability. The details about neck instability formulation will be given further. The FE model was designed according

to the dimensions and geometry of the experimental test sample using 8-node meshing elements, isoparametric and arbitrarily hexahedrics, see **Fig. 3.3**. The strains are constant throughout the meshing elements due to tri-linear interpolation functions which tend to offer a poor representation of the shear behavior. The eight-point Gaussian integration, appropriate to model an incompressible plasticity behavior, is used to formulate the stiffness. A fine mesh consisting of 2256 quadrilateral elements was used to compose the FE model. The advantage of fine meshing consists on providing narrow shear bands along the boundaries of the element and offers a greater freedom for local deformation (Tvergaard et al., 1981; Wu and van der Giessen, 1995). Furthermore, in order to reduce the computational processing time, the gauge ends have been reduced in the simulation model. Note that, the origin of the Cartesian coordinate system is fixed at the center of the model (Wu and van der Giessen, 1995).

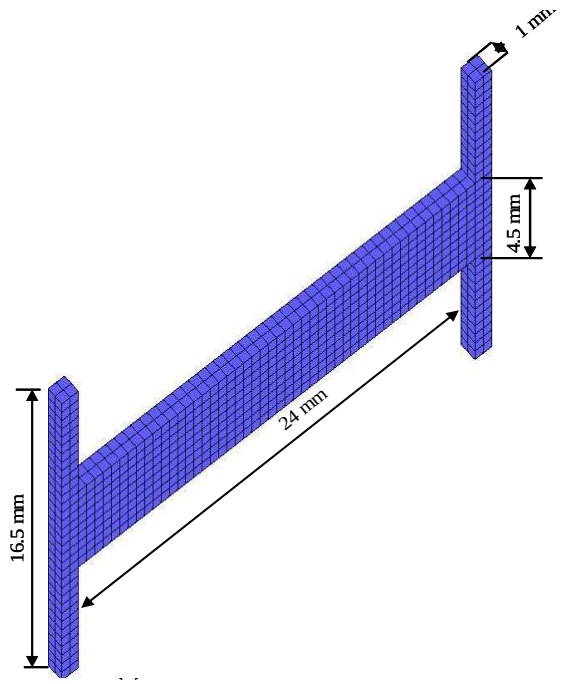

Fig. 3.3. Geometry and meshing of the sample.

II.2. Formulation of neck initiation and propagation

Many authors proposed an initial geometry defect in numerical simulation in order to activate the neck initiation (G'sell and Jonas, 1979; Neale and Tugcu, 1985;

Tugcu and Neale 1987a; 1987b; Smith, 1994; Wu and van der Giessen, 1994; Van Melick, 2003; Kown and Jar, 2008). Wu and van Der Giessen (1995) proposed to introduce an initial mechanical imperfection of the initial shear strength s_o by means of:

$$\Delta s_o = \zeta s_o \cos(\frac{\pi x}{L_o}) \tag{3.6}$$

where ζ is the intensity of the imperfection, L_o is the half length of the sample and the actual initial strength is $s_o - \Delta s_o$. The imperfection is activated in the centre of the specimen i.e at $x = 0$. In this work, we have employed this method to initiate necking. The corresponding values for HDPE have been determined using standard optimization: $ss_c = 125$ MPa, $\zeta = 0.05$ and $h = 1800$ MPa.

II.3. Results and discussion

In this section, the results obtained by FE simulations for the three polyethylene specimens (HDPE, LDPE, and ULDPE) are compared to experimental data.

II.3.1. HPDE material

The experiments and numerical load-displacement curves are ploted in **Fig. 3.4.** The FE response is quite different of the experimental data, that the general trends are captured. This is essentially due to the necking modeling which is not well reproduced by the approach we used. Indeed, the peak corresponding to the necking initiation is overestimated. Moreover the severity of the necking is underestimated; the FE drop off during the propagation is slower than that observed experimentally. This indicates that this phenomenon still remains difficult to capture.

Fig. 3.5 provides FE images of stress distribution along specimen surface during different stages of deformation, indicated by numbers from 1 to 5. The numbers are matching to the numbers appear in **Fig. 3.4** along force-displacement simulation curve. The left-side images of **Fig. 3.5** (**T**A indicated under the images) are

corresponding to intermolecular stress distribution along specimen at different stages of deformation; the initiation and propagation of neck can be clearly observed. The right-side images of **Fig. 3.5** (T_B indicated under the images) are corresponding to molecular network stress. Through FE, images it can be observed that the stress distribution along specimen is not homogenous, especially after neck initiation due to neck propagation throughout specimen.

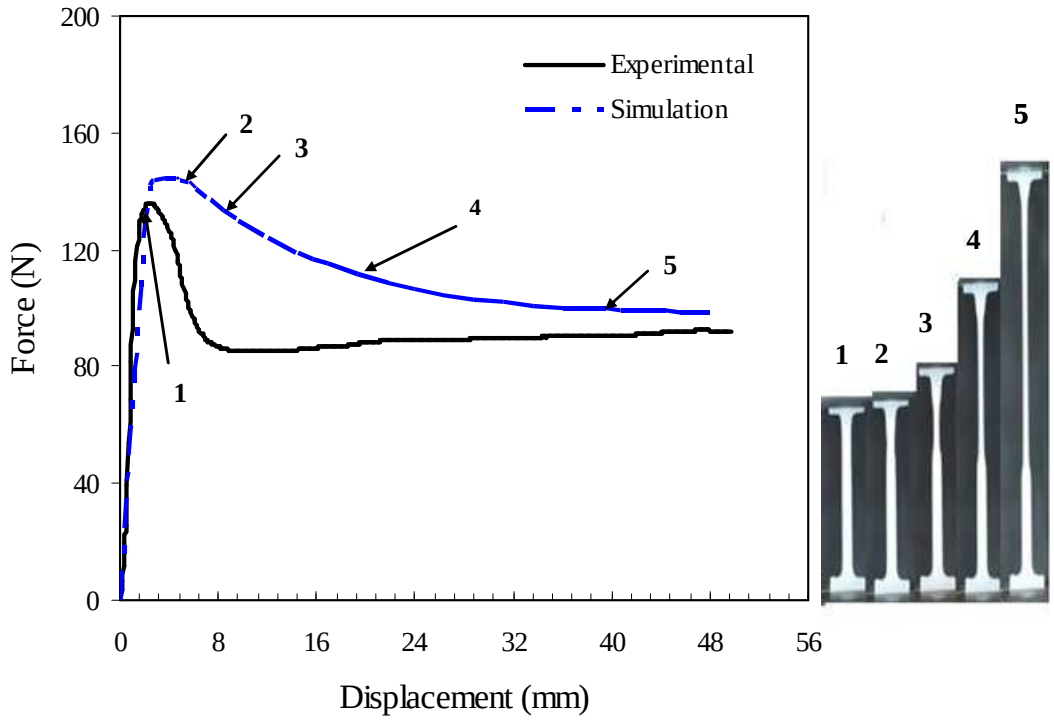

Fig. 3.4. FE simulation vs. experimental data for HDPE, with picture of specimen at different stages of deformation.

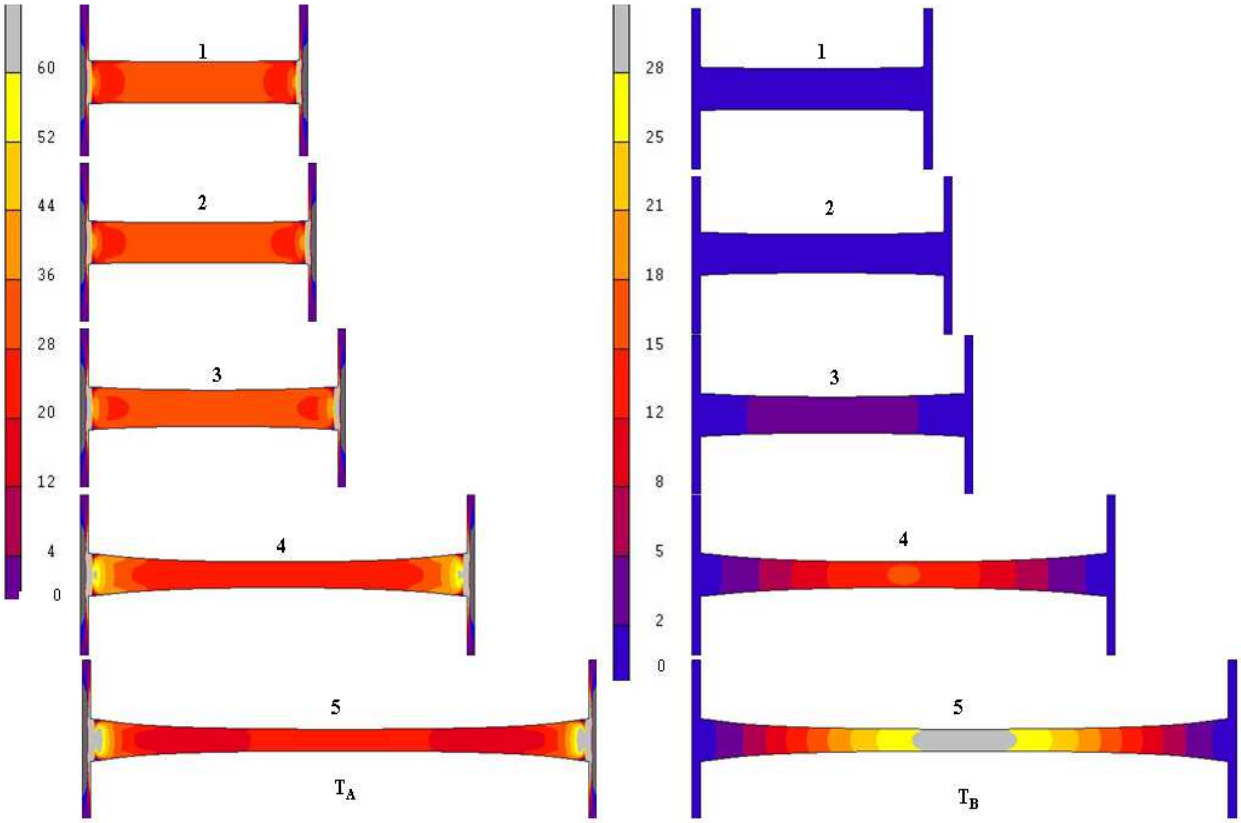

Fig. 3.5. FE images of stress distribution during deformation along HDPE specimen for intermolecular stress ($\mathbf{T_A}$) and molecular network stress ($\mathbf{T_B}$).

II.3.2. LPDE material

Fig. 3.6 provides experimental and FE force-displacement curves for LDPE. The experiments demonstrate that there is no neaking for LDPE. Therefore, in the FE subroutine the implementation of Eqs. (3.4) and (3.6) was switched off in order to avoid the shear stress evolution and the mechanical imperfection during simulation. The FE results exhibits in this case a good agreement with the experimental data as shown in **Fig. 3.6.** The numerated pictures are corresponding to the different stages of deformation indicated on the force-displacement curve. In the LDPE material, the strain-softening after yield point does not appear, the applied force continues to grow up. In addition, the strain localization in specific area was not observed at any stage of deformation as observed in the specimen surface pictures in **Fig. 3.6**.

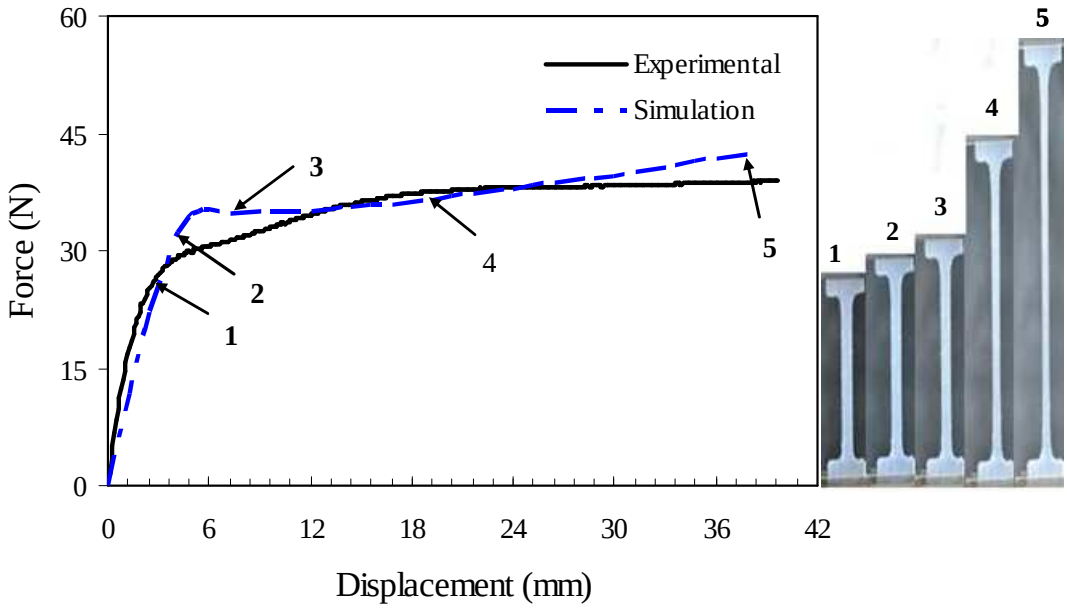

Fig. 3.6. FE simulation vs. experimental data for LDPE, with pictures of specimen at different stages of deformation.

The FE images of stress distribution along specimen surface are depicted in **Fig. 3.7**. The images numerated in **Fig. 3.7** are corresponding to the different stages of deformation numerated and depicted in **Fig. 3.6**. The left-side images of **Fig. 3.7** are corresponding to intermolecular stress distribution. The right-side images of **Fig. 3.7** are corresponding to molecular network stress distribution. It can be noticed that the stress distribution along the specimen gauge section is quite homogenous during all the deformation process.

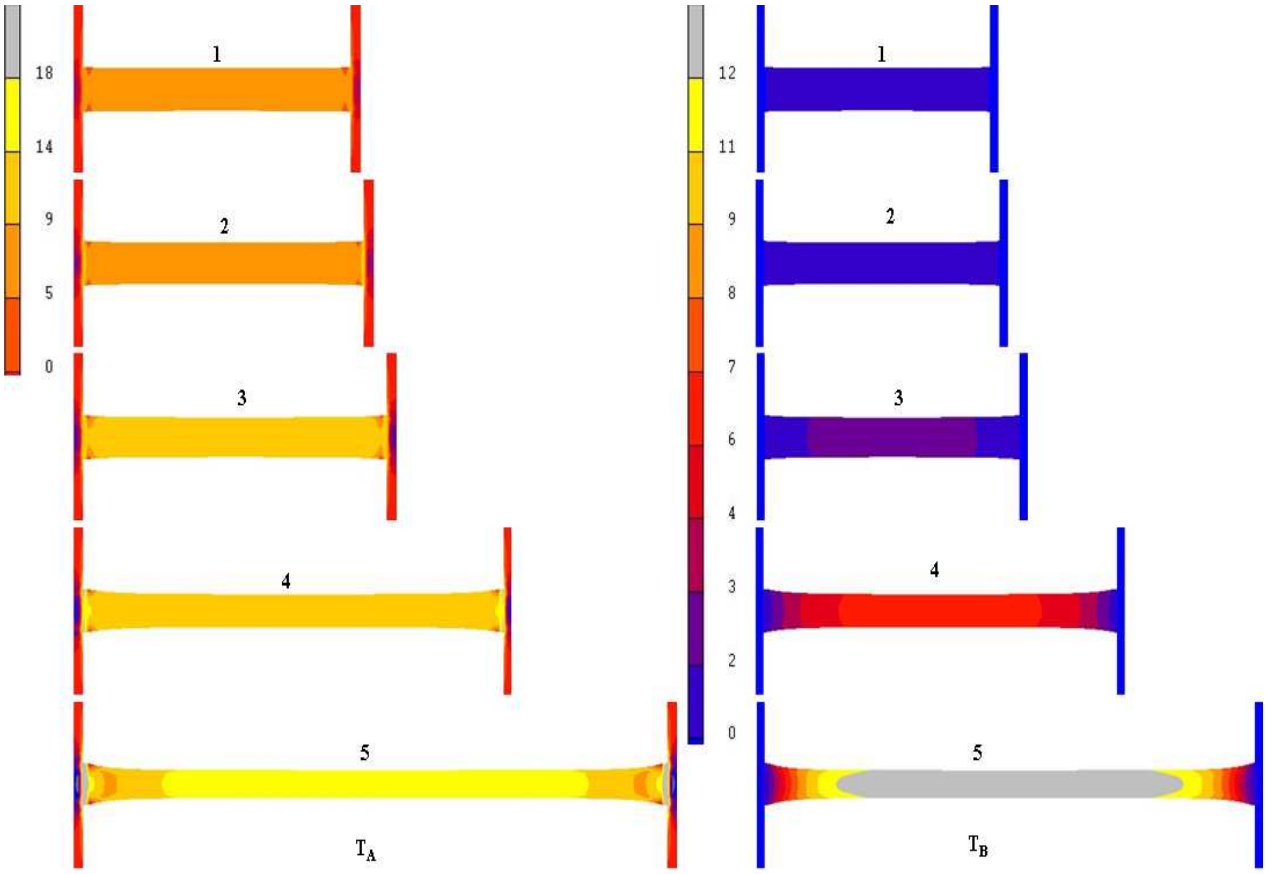

Fig. 3.7. FE images of stress distribution during deformation along LDPE specimen for intermolecular stress (T_A) and molecular network stress (T_B).

II.3.3. ULDPE material

The simulated force-displacement behavior is in a very good agreement with the experimental data as depicted in **Fig. 3.8**. The corresponding pictures at different stages of deformation have illustrated the stability of ULDPE plastic deformatio. The simulated and experimental data of ULDPE (**Fig. 3.8**) do not exhibit post-yield strain softening as in case of LDPE.

The **Fig. 3.9** provides FE images of stress distribution along specimen for both intermolecular resistances (T_A) in left-side of **Fig. 3.9** and molecular network resistances (T_B) in right-side of **Fig. 3.9**. Each number corresponds to the different stages of deformation labelled in **Fig. 3.8**. Through FE image colour bands, we can observe the homogeneous stress distribution along the specimen gauge section.

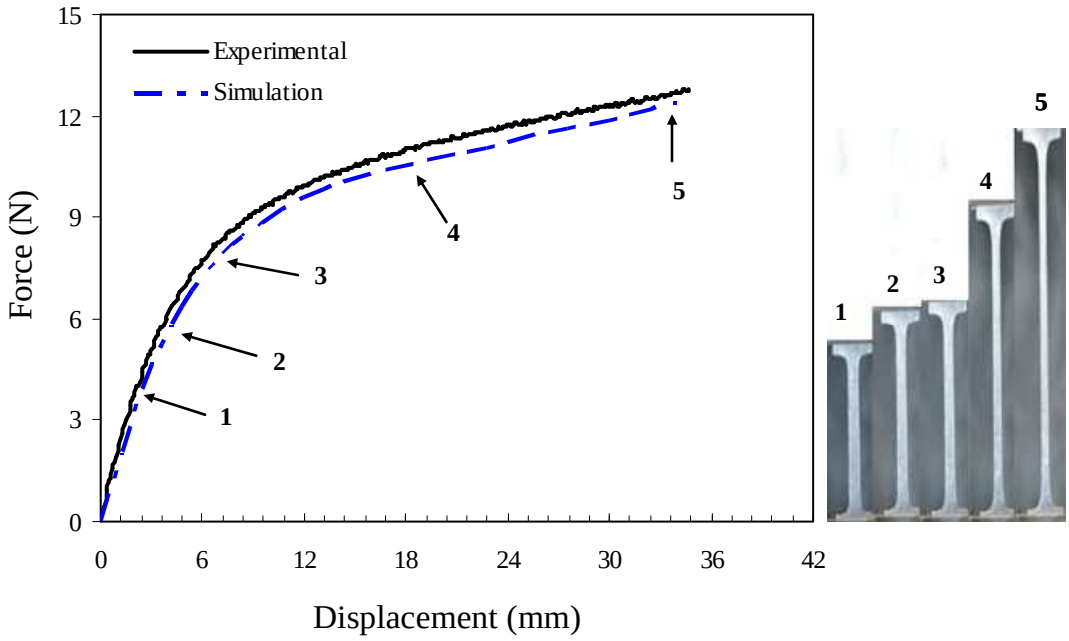

Fig. 3.8. FE simulation vs. experimental data for ULDPE, with pictures of specimen at different stages of deformation.

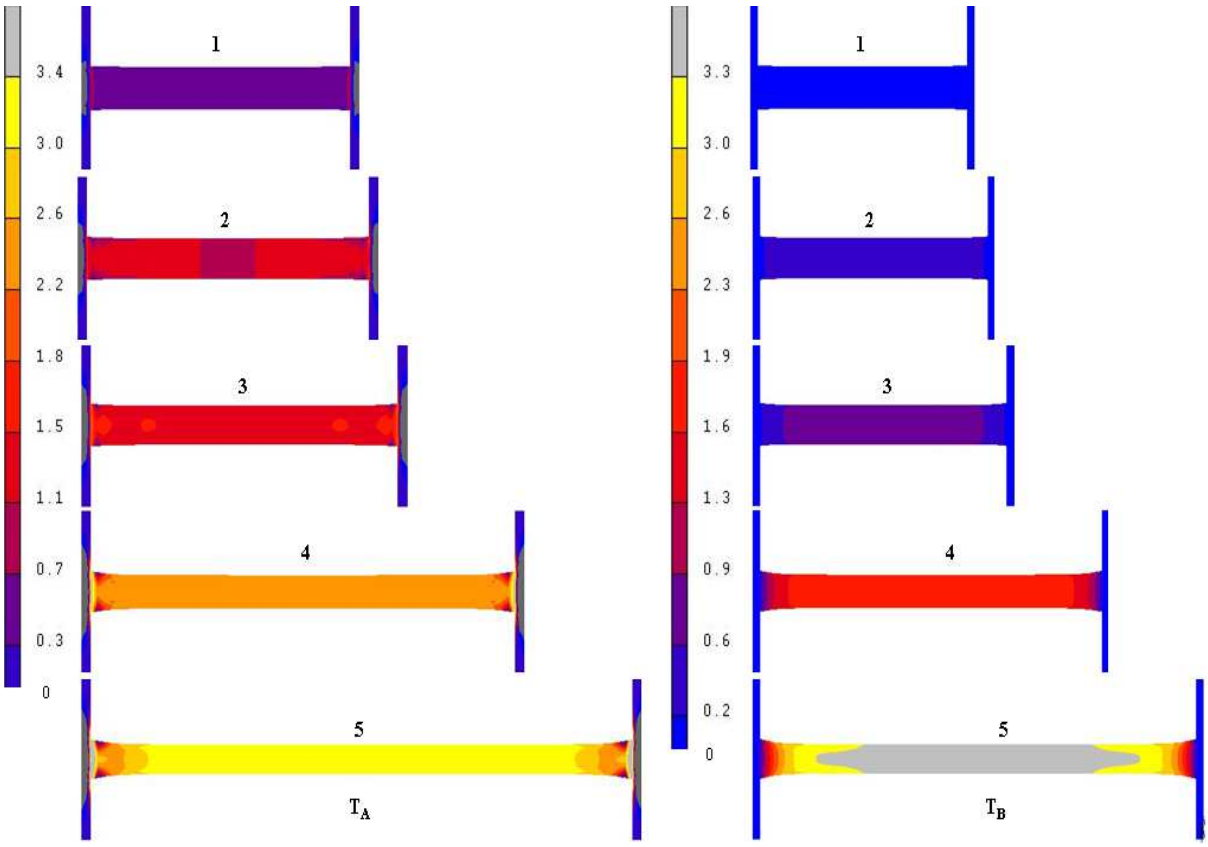

Fig. 3.9. FE images of stress distribution during deformation along ULDPE specimen for intermolecular stress ($\mathbf{T_A}$) and molecular network stress ($\mathbf{T_B}$).

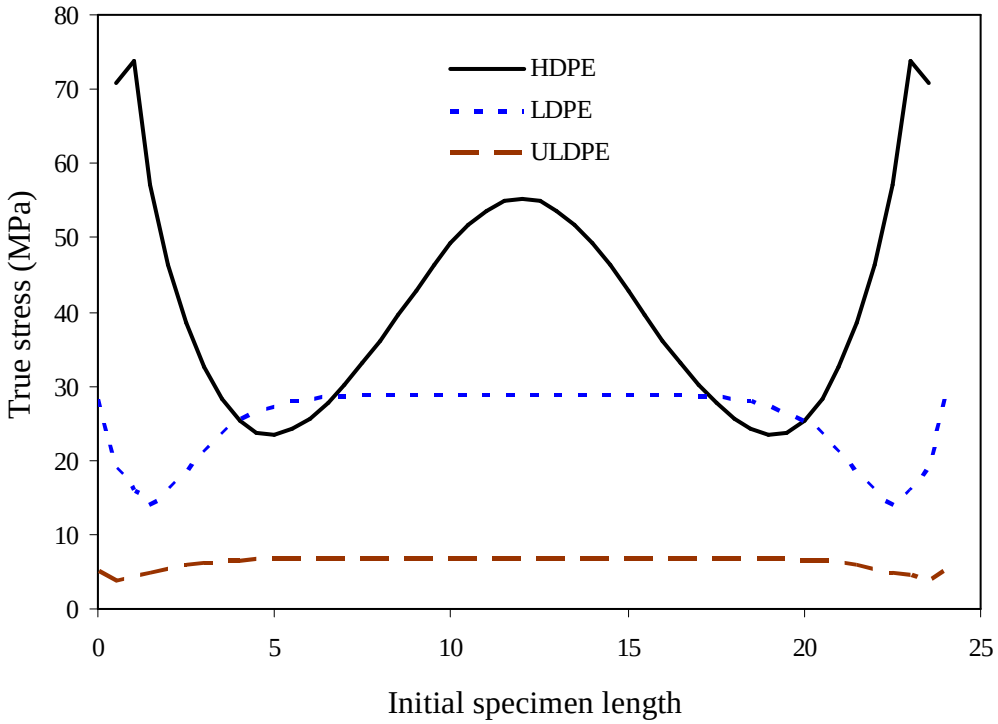

Fig. 3.10. Axial trus stress distribution along specimen surface for HDPE, LDPE, and ULDPE at 160 % deformation of specimen initial length.

II.4. Partial conclusions

The MBSL1 constitutive model developed in chapter two was implemented in a FE code. The mechanical responses of polyethylene materials (HDPE, LDPE, and ULDPE) have been individually analysed. It was found that the FE simulations successfully captured the main features of the experimental observation for polyethylene materials. Therefore, the crystal fraction dependence on the locad fields (as shown on an example in **Fig. 3.10**) can be predicted. In particular, the crystal fraction effect on the unstable post-yield deformation can be reproduced by the proposed tool.

III. Multi-layered polyethylene laminates

In this part, multi-layered polyethylene laminates have been experimentally analysed. The multi-layered specimens have been desgined by Fréderix (2009). The designed materials are consisting in bilayered composites which the thickness is 1

mm per layer. In this work, two combinations have been tested HDPE/LDPE and HDPE/LDPE.

III.1. Bi-layered HDPE/LDPE laminate

As mentioned before, LDPE has a stable plastic deformation and HDPE exhibits unstable plastic deformation through post-yield strain-softening; a combination of both plastic deformation behaviors is presented in **Fig. 3.11.** The experimental response of the bi-layered material exhibits post-yield strain-softening

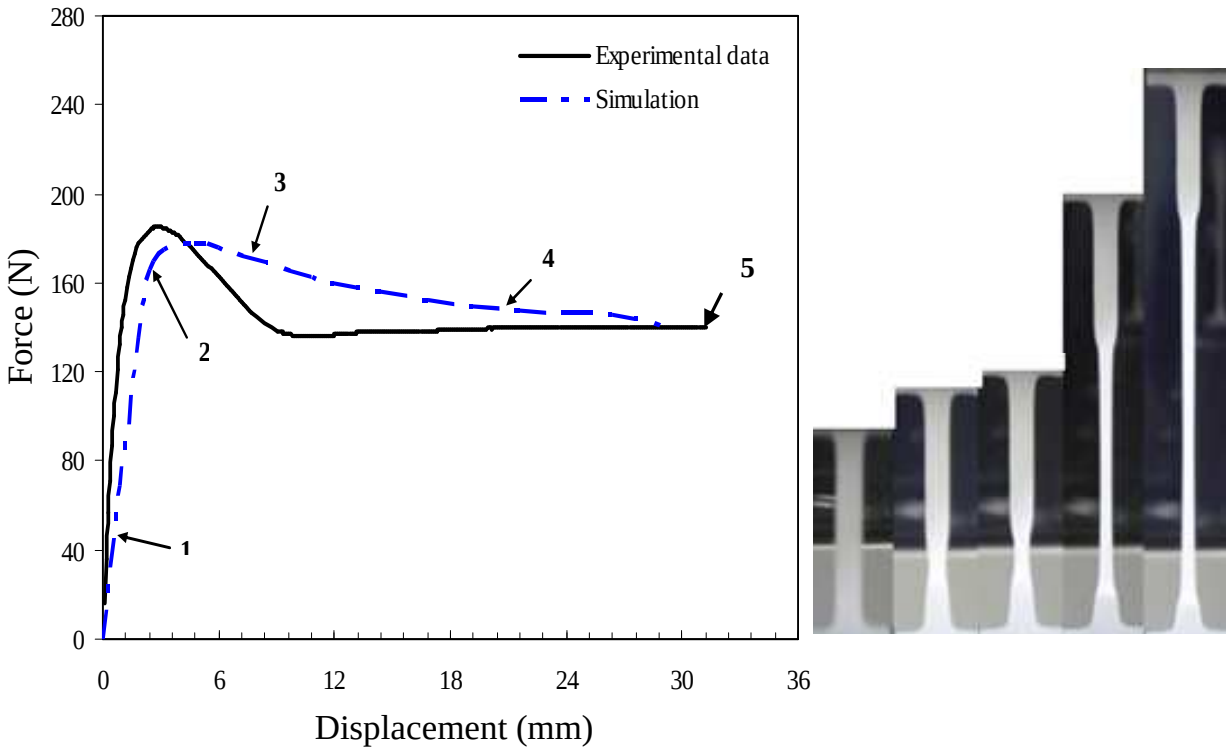

Fig. 3.11. FE simulation vs. experimental data for bi-layered HDPE/LDPE specimen (50 % HDPE and 50 % LDPE) with pictures of specimen at different stages of deformation.

Fig. 3.12 shows FE results in terms of stress distribution of both intermolecular and molecular network resistances at different stages of deformation; the images are numerated in correspondence with **Fig. 3.11**. The FE images are exposed in 3D colour band (**Fig. 3.12**) in order to illustrate the amount of stress withstanding by different layers along the specimen. The front face depicts stress sustained by LDPE layer and

back face depicts the stress sustained by HDPE layer. It is obvious that each layer exhbits different amount of stress due to their different mechanical behavior.

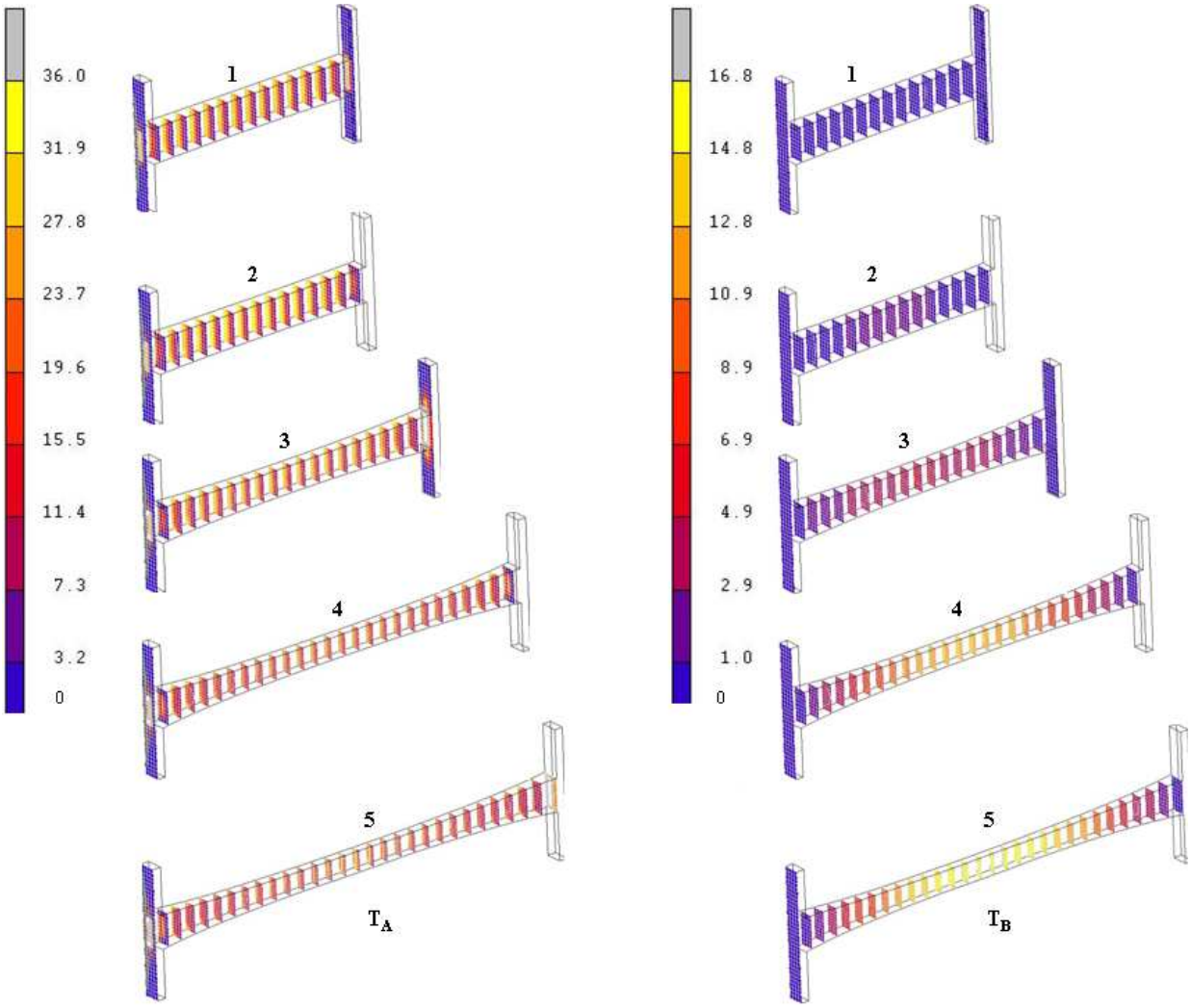

Fig. 3.12. FE images of stress distribution during deformation along bi-layered HDPE/LDPE specimen, for intermolecular stress ($\mathbf{T}_A$) and molecular network stress ($\mathbf{T}_B$).

The axial true stress distributions along both sides of specimens have also been studied. The results are depicted in **Fig. 3.13** for bi-layered HDPE/LDPE specimen but with increasing content of LDPE**.** As can be seen in **Fig. 3.13-a**, the stress distribution on both sides of specimen (HDPE in left side and LDPE in right side) shows the different responses under the same rate of deformation. Furthermore, LDPE changes the behavior of neck initiation and propagation at different stages of deformation.

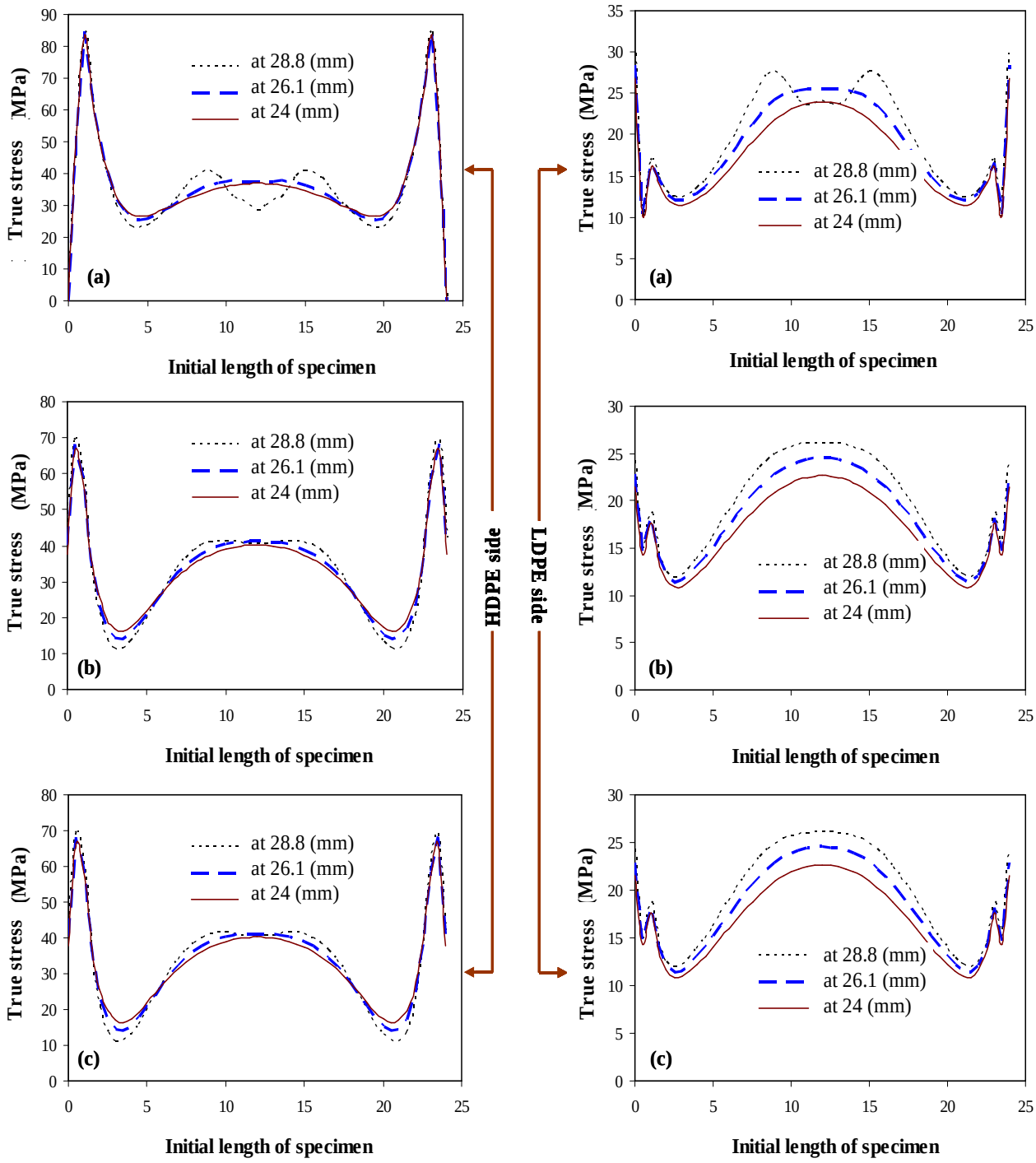

Fig. 3.13. Axial true stress distribution along specimens surfaces of bi-layer HDPE/LDPE specimen: (a) 50% HDPE+50% LDPE, (b) 30% HDPE+70% LDPE, (c) 22.5% HDPE+77.5% LDPE.

In early stages of deformation, the necking propagates in a stable way, while at higher deformation level corresponding to 28.8 mm of displacement, the neck behavior changes and unstable necking is observed. Instead of one peak of stress in

the middle of specimen as it used to be. Two smaller peaks of stress appeared around the centre in both sides of specimen. However, even a multi-peak appeared when deformation increases, it is not enough to initiate macroscopically a multi-necking, as shown in pictures **Fig. 3.11**.

Besides, the HDPE proportion has been modifided and the simulation results are reported in Figs**. 3.13-b** and **3.13-c.** we can observe that the peak of stress is in the middle of the specimen, while at the HDPE side, the peak exisits but it is less pronounced. Thus, stabilization of necking in these materials could be achieved by changing the thickness of the HPDE layer.

III.2. Bi-layered HDPE/ULDPE laminate

The experimental data shown in **Fig. 3.14** illustrates the behavior of this material; once the load reaches its maximum, enhanced plastic flow occurs associated with a load drop. This indicates the initiation of necking due to the presence of HDPE layer. As previously observed for pure HDPE, the necking process still remains different to capture by FE simulation. The initiation of necking and its propagation can be observed along specimen as shown in pictures depicted in **Fig. 3.14**. Strain localization in two different places can be observed. This is probably due to stress interaction between the necking end and the specimen end when a stress concentration is pointed out.

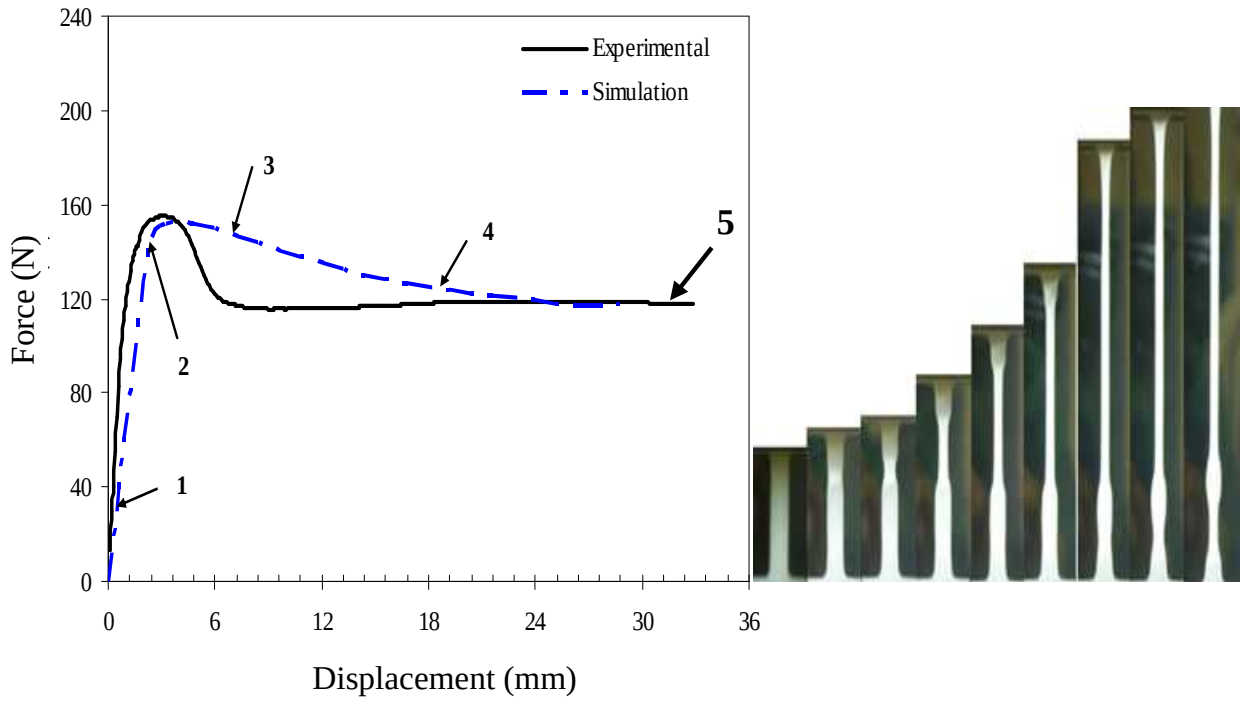

Fig. 3.14. FE simulation vs. experimental data for bi-layer HDPE/ULDPE specimen (50% HDPE and 50% of ULDPE) with pictures of specimen at different stages of deformation.

The FE images in **Fig. 3.15** present the stress distribution along multi-layered material, in term of the contribution of intermolecular (T_A) and molecular network (T_B) resistances in correspondence with **Fig. 3.14**.

Fig. 3.16 provides total stress distribution along bi-layered HDPE/ULDPE specimen. The effect of ULDPE (*which exhibit stable plastic deformation*) on the HDPE (*which exhibits necking*) has been examined. As it can be seen in **Fig. 3.16-a** that the stress distribution on both sides of specimen (HDPE in left side and ULDPE in right side) shows different responses under the same rate of deformation.

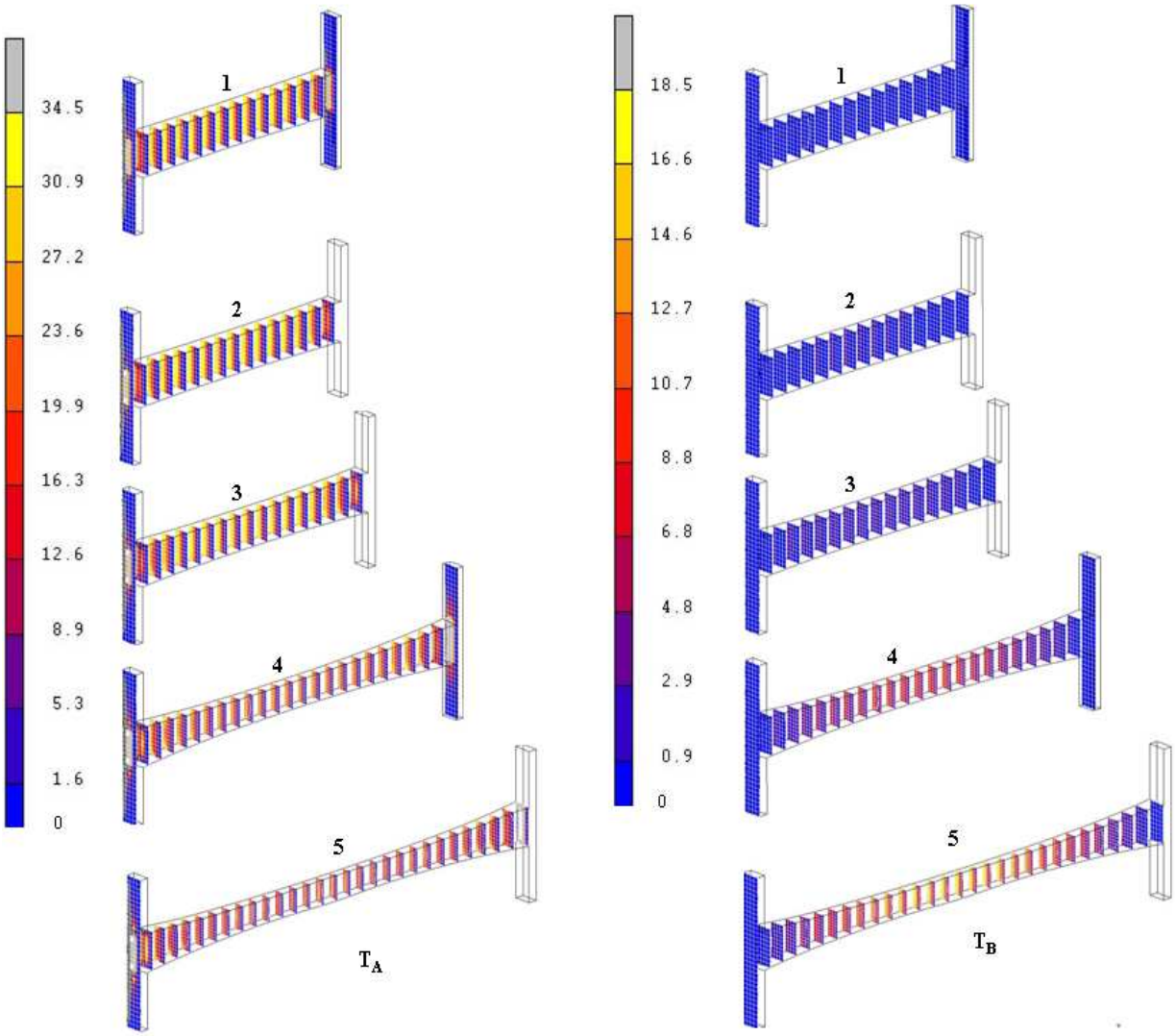

Fig. 3.15. FE images of stress distribution during deformation along bi-layered HDPE/ULDPE specimen (50% HDPE and 50% of ULDPE) for intermolecular stress ($\mathbf{T_A}$) and molecular network stress ($\mathbf{T_B}$).

Moreover, the initiation of necking and its propagation at different stages of deformation are under combination effects of both layers. At advanced stage of deformation (28.8 mm of displacement), the stress distribution in both sides of the specimen is very unstable and fluctuating around the specimen centre, as shown in **Fig. 3.16-a** (*as mentioned previously the necking forced to initiate in the centre of specimen*). A multi-peak phenomenon is clearly observed. This behavior indicates highly unstable plastic deformation and multi-neck initiation.

In addition, two other thickness ratios have been examined by FE simulation: 30% HDPE with 70% ULDPE and 22.5% HDPE with 77.5% ULDPE as shown in **Fig. 3.13-b** and **Fig. 3.13-c,** respectively. By increasing the thickness of ULDPE layer, the fluctuation previously observed progressively vanishes, as shown in **Fig. 3.16-b** and **Fig. 3.16-c**. No neck significant changes are observed when considering the HDPE side.

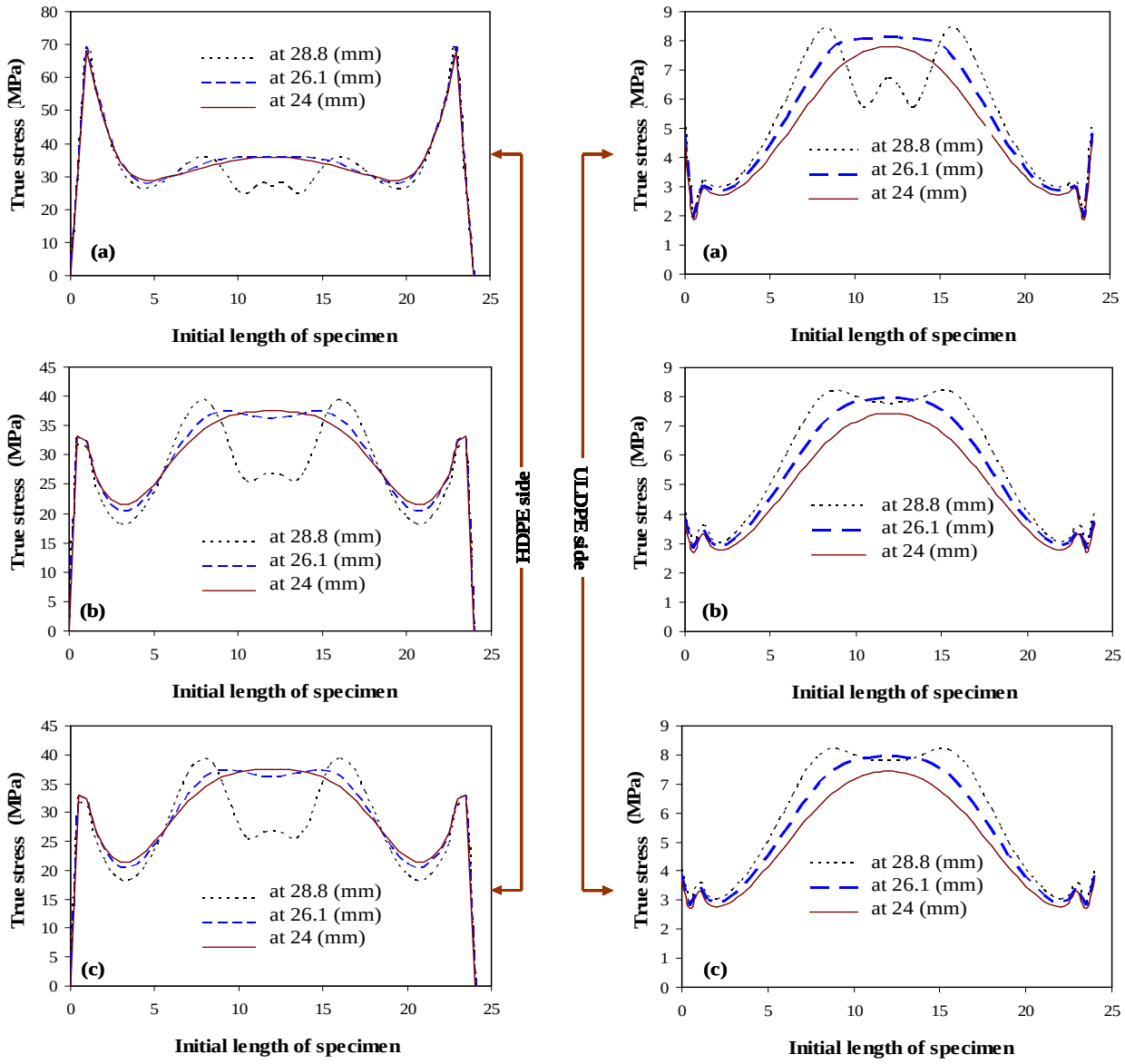

Fig. 3.16. Axial true stress distribution along bi-layer of HDPE/ULDPE specimen: (a) 50% HDPE+50% ULDPE, (b) 30% HDPE+70% ULDPE, (c) 22.5% HDPE+77.5% ULDPE.

III.3. Partial conclusions

In this part, bi-layered polyethylene laminates were experimentally tested. Numerical simulations were also performed using the same subroutine described in **section I.1**. Different HDPE thicknesses materials were used in bi-layered materials, and their mechanical responses were predicted numerically in order to observe their post-yield deformation behavior.

IV. Stress triaxiality effects

In order to estimate the stress triaxiality effects of thes on the mechanical response of pure and multi-layered polyethylene materials, FE simulation have been performed, using round notched bar specimen. The stress triaxiality is varied by varying the curvature radius of the notch.

IV.1. Stress triaxiality state of notched round bars

Notched round bar specimens with different curvature radii were modelled in FE code, see **Fig. 3.17**. The specimens are referred to as R_x where x is the value of curvature radius in mm (R80, R10 and R4). The curvature radius was chosen in order to obtain different stress triaxiality states in the median cross-section.

The triaxiality ratio η is defined as the ratio of the hydrostatic mean stress T_h to the von Mises equivalent stress T_{eq}:

$$\eta = \frac{T_h}{T_{eq}} \tag{3.7}$$

where T_h and T_{eq} are expressed in the principal directions by:

$$\begin{aligned} T_h &= \frac{1}{3}(T_1 + T_2 + T_3) \\ T_{eq} &= \frac{1}{\sqrt{2}}((T_1 - T_2)^2 + (T_1 - T_3)^2 + (T_3 - T_2)^2)^{1/2} \end{aligned} \tag{3.8}$$

in which T_1, T_2 and T_3 are the principal true stresses.

According to Bridgman formula (Bridgman, 1944), the triaxiality ratio can be approached by:

$$\eta = \frac{1}{3} + ln(1 + \frac{r}{2R_x}) \tag{3.9}$$

where R_x is the curvature radius and r is the minimum radius (2.5 mm) was chosen for the three specimens. According Bridgman equation, the initial stress triaxiality ratio is equal to 0.33, 0.44 and 0.6 for R80, R10 and R4 specimens, respectively.

IV.2. Simulation model

The FE model was designed according to the dimensions and geometry of the experimental test sample employed by Hachour et al. (2014) using 8-node meshing elements, isoparametric and arbitrarily hexahedrics, the dimension of specimens are indicated in **Fig. 3.17**. In order to reduce the computational processing time, the axisymmetric assumption (geometric property) has been used. To avoid geometry defect and obtain regular mesh, the rouled surface has been employed in curvature surface of specimens, and quad surface has been used in rectangular surface, resulting in the regular mesh obtained, in **Figs. 3.18** and **3.19**. The cartesian coordinate system is fixed in the centre as mentioned before. **Fig. 3.18** shows the meshing used to simulate the polyethylene materials, while **Figs. 3.19** show that used to simulate multi-layered materials. These later are designed from three different polyethylene materials with different crystal volume fraction (HDPE, LDPE, ULDPE), each specimen consisting in three layers of equal radial thickness (*materials are numerated as 1, 2 and 3*). The same curvature radii for each layer have been adopted to ensure the same initial stress triaxiality state. Two configurations have been considered to the graded proportion: (a) core in HDPE and shell in ULDPE and (b) core in ULDPE and shell in HDPE. In both case, a LDPE layer is between the core and the shell. All the simulations have been performed under constant strain rate of 0.001 s^{-1}.

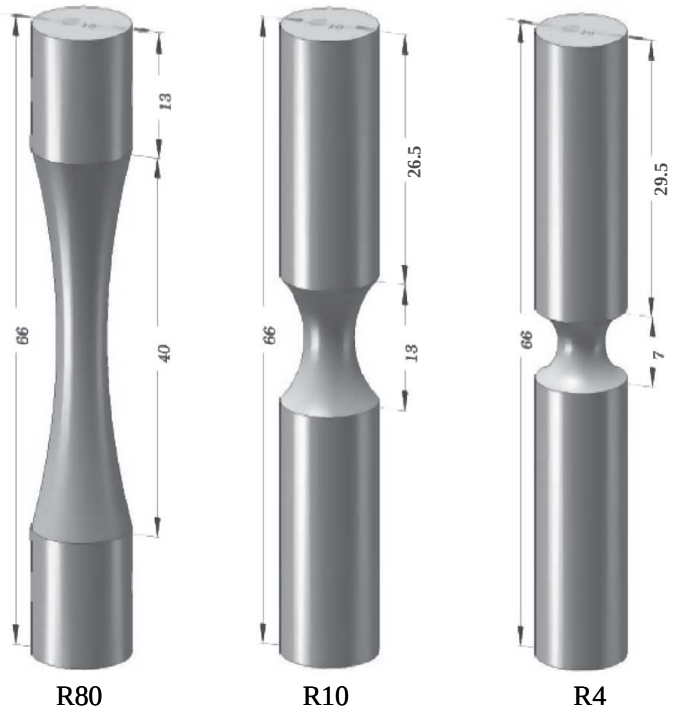

Fig. 3.17. Geometry of specimens (Hachour et al., 2014).

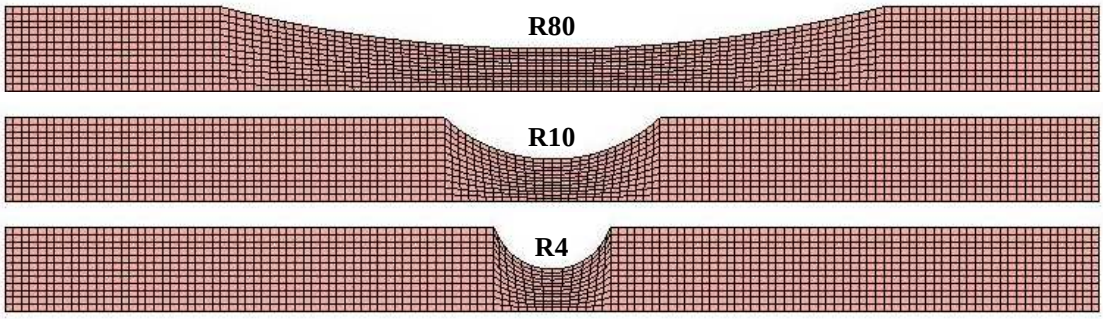

Fig. 3.18. FE meshing for pure polyethylene materials.

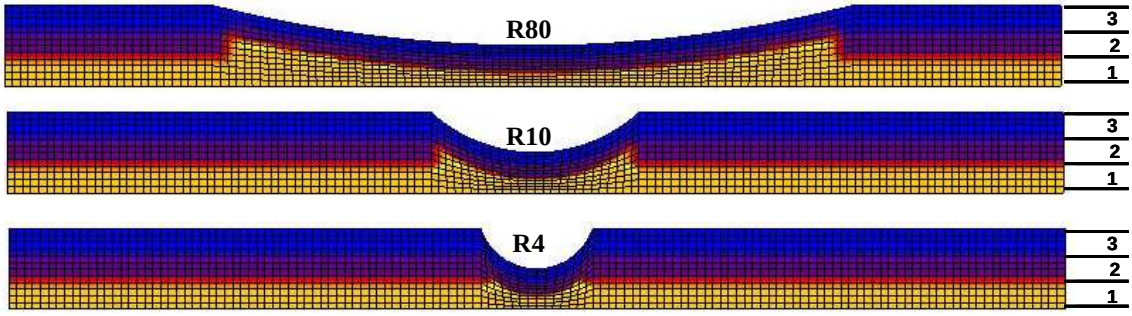

Fig. 3.19. FE meshing for multi-layered materials.

IV.3. Results and discussion

The FE results are presented in two manners: the total stress and strain as a function of the reduction of median cross-section radius, and the triaxiality distribution among specimens and through the median cross-section for each material and specimen geometry.

IV.3.1. Stress-strain results of notched round specimens

The results obtained from the specimens with different curvature radii for polyethylene (HDPE, LDPE and ULDPE) materials are presented in **Fig. 3.20**. This figure shows the of net stress (F/A_o) as a function of evolution of nominal diameter strain ($\Delta r/r_o$), in which F is defined as the load, A_o is the initial median cross-section area, Δr is are the reduction of median cross-section radius, and r_o the initial median cross-section radius. The effect of the initial stress triaxiality state on the overall behavior can be clearly observed in terms of maximum net stress and maximum nominal diameter strain. The initial elastic stiffness is observed to exhibit a negligible dependence on stress triaxiality for HDPE. Hachour et al. (2014) experimentally obtained similar results for HDPE, while for LDPE and ULDPE, the initial elastic stiffness depends on stress triaxiality ratio. However, the stress triaxiality affects both the initial flow stress and the maximum net stress response; it increases with an increase in stress triaxiality. Furthermore, the influence of stress triaxiality can be also observed on nominal diameter strain. Indeed, increasing the stress triaxiality ratio leads to a decrease of the the maximum nominal diameter strain.

Fig 3.21 presents the results of multi-layered materials for both configurations; configuration (a) (core in *HDPE*) and configuration (b) (core in *ULDPE*).

The axial strain distribution over the specimens for both configurations (a and b), with different curvature radii (R80, R10, R4) and at different nominal diameter strains ($\Delta r/r_o$) are presented in **Figs. 3.22, 3.23, and 3.24**. It can be observed that the local deformation to attend the same nominal diameter strain for different configurations with the same curvature radius is different. It needs to be highlighted

that, with the configuration (b) (see **Figs. 3.22-b, 3.23-b,** and **3.24-b**) the negative zones (compression strain) appear just behind the shoulders of gauge section even the specimens is under tension.

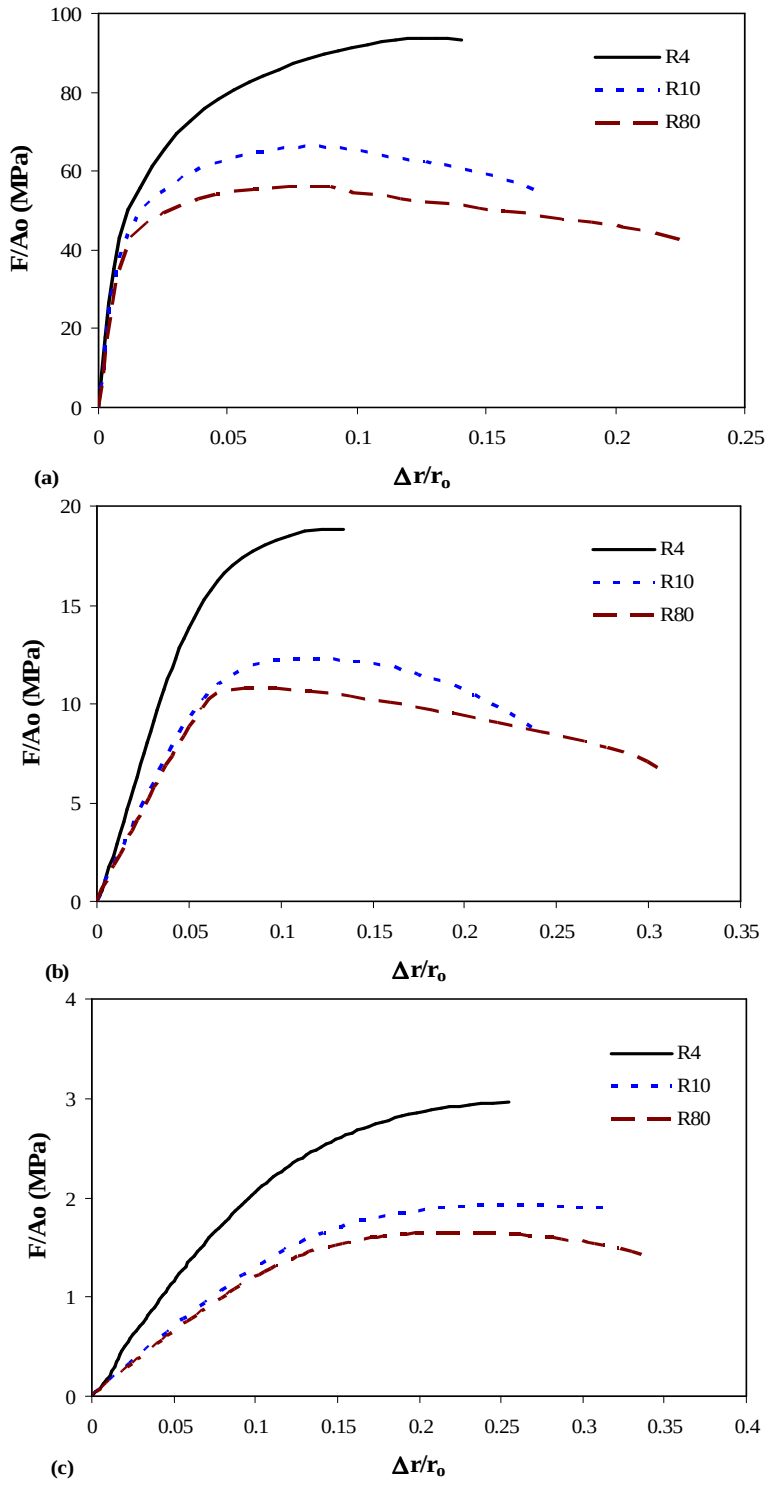

Fig. 3.20. Net stress (F/A_o) vs. nominal diameter strain($\Delta r/r_o$): (a) HDPE, (b) LDPE and (c) ULDPE.

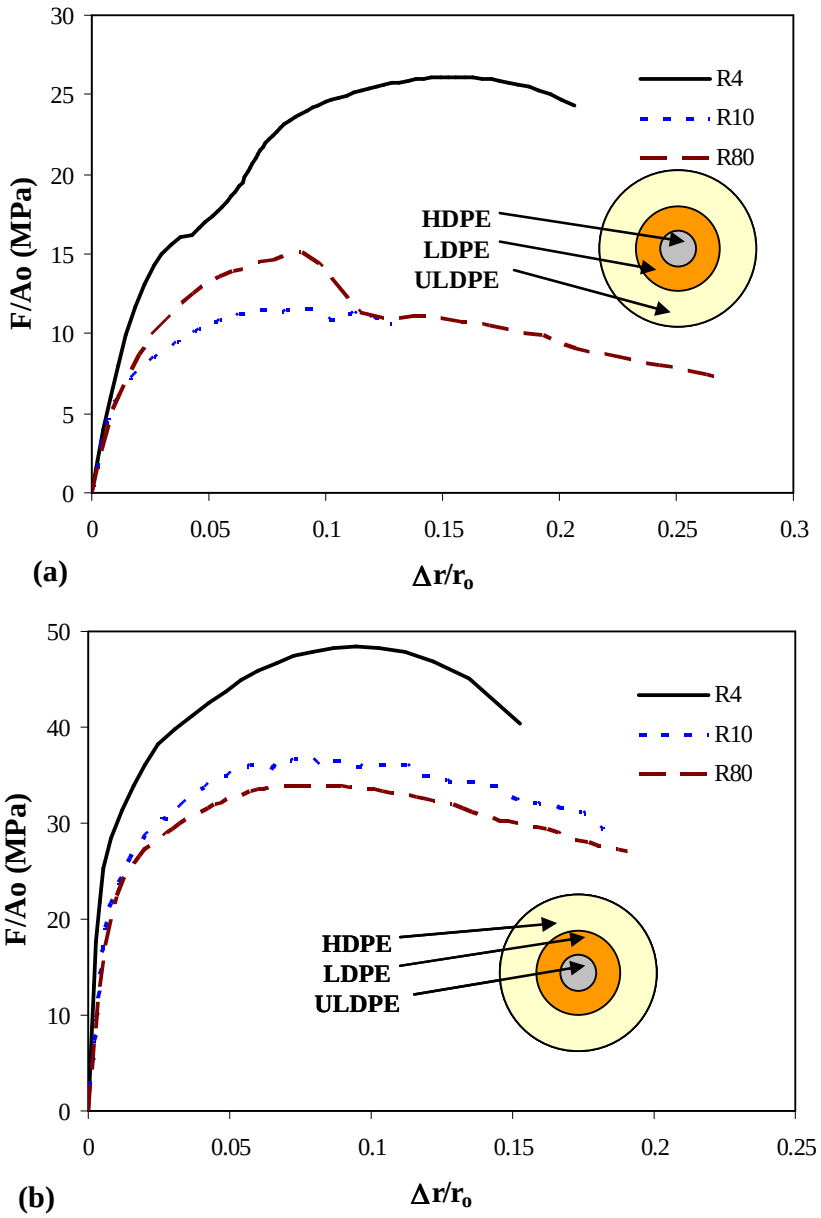

Fig. 3.21. Net stress (F/A_o) vs. nominal diameter strain($\Delta r/r_o$), (a) core inHDPE, (b) core in ULDPE.

It can be mentioned that, the strain concentration in gauge section of curvature radius R4 (**Fig. 3.24**) is not only in the median cross-section, it appers rather in three different locations, at median cross-section near to the specimen surface of, and in both side of median cross-section near to symmetry axis. This fact may be due to the combination of initial stress triaxiality state and plastic deformation instability of HDPE. Keeping in mined the HDPE exhibits neck phenomenon, it may introduce extra stress triaxiality different than the one designed and controlled by notch radius.

Figs. 3.22, 3.23, and 3.24 illustrate the axial stress distribution over the specimens at different nominal diameter strains ($\Delta r/r_o$) with different curvature radii (R80, R10, R4) respectively, for both configurations (a and b). As expected, the axial tensile stress focuses on the layer which consists of HDPE more than other layers. We also observed that, the compression stress arise in gauge section layers unless in HDPE layer, as shown in **Figs. 3.25-a, 3.26-a,** and **3.27-a**. While with the configuration (b) (see **Figs. 3.27-b, 3.28-b,** and **3.27-b**) the compression stress appears at the shoulders of gauge section. The transverse compressive stress develope through gauge section and gauge shoulders are due to different stress triaxiality state arising through specimens.

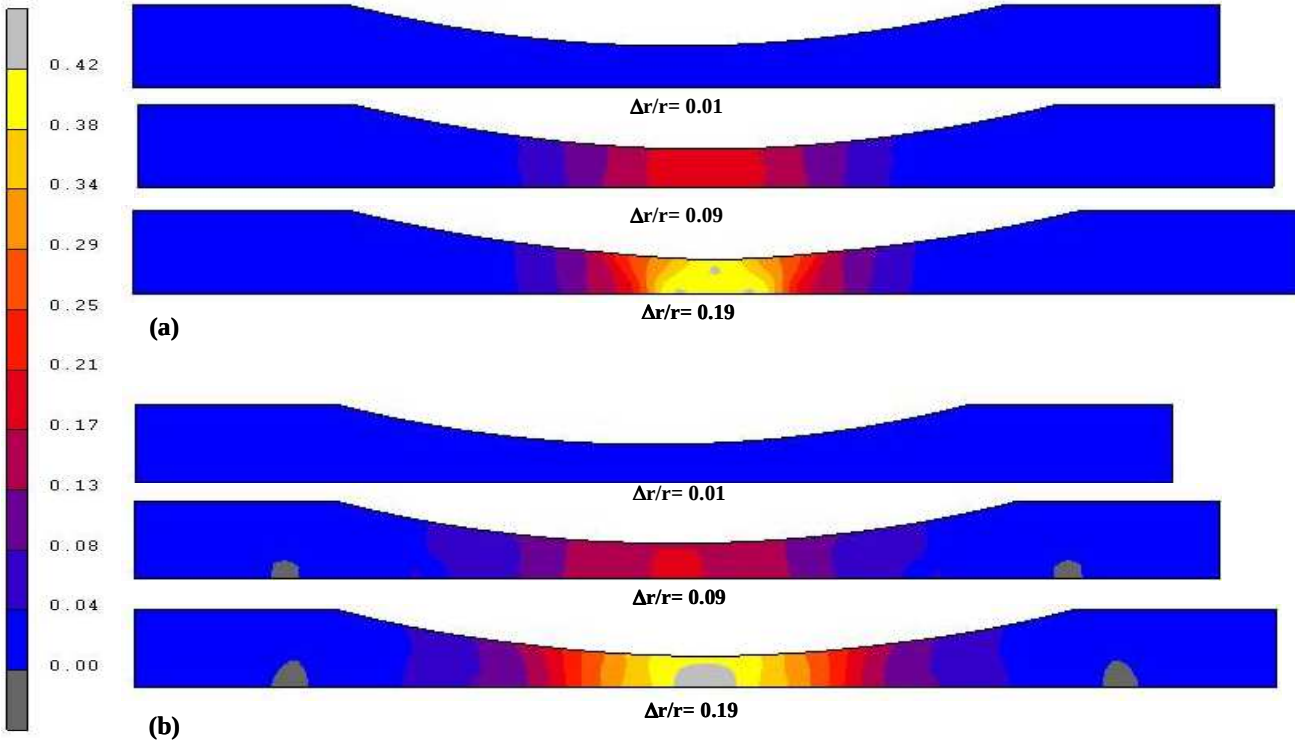

Fig. 3.22. FE axial strain distribution for R80 specimen at different nominal diameter strains ($\Delta r/r_o$): (a) core in ULDPE, (b) core in HDPE.

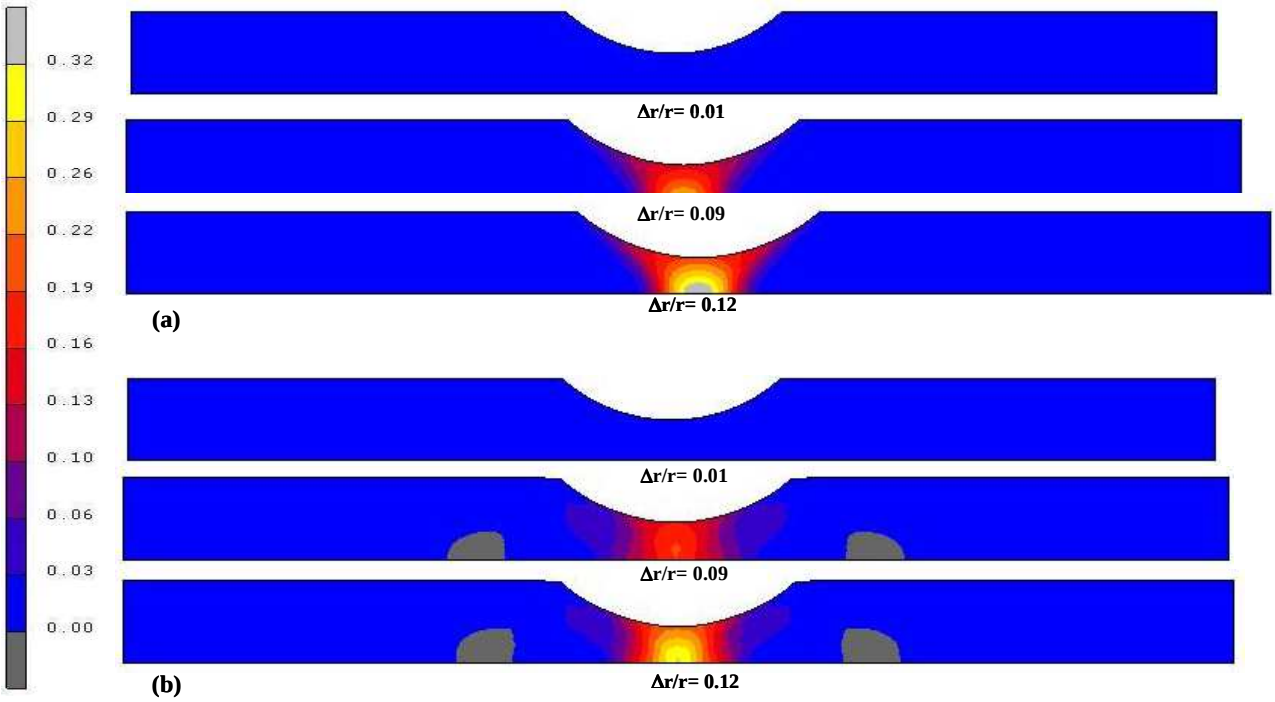

Fig. 3.23. FE axial strain distribution for R10 specimen at different nominal diameter strains ($\Delta r/r_o$): (a) core in ULDPE, (b) core in HDPE.

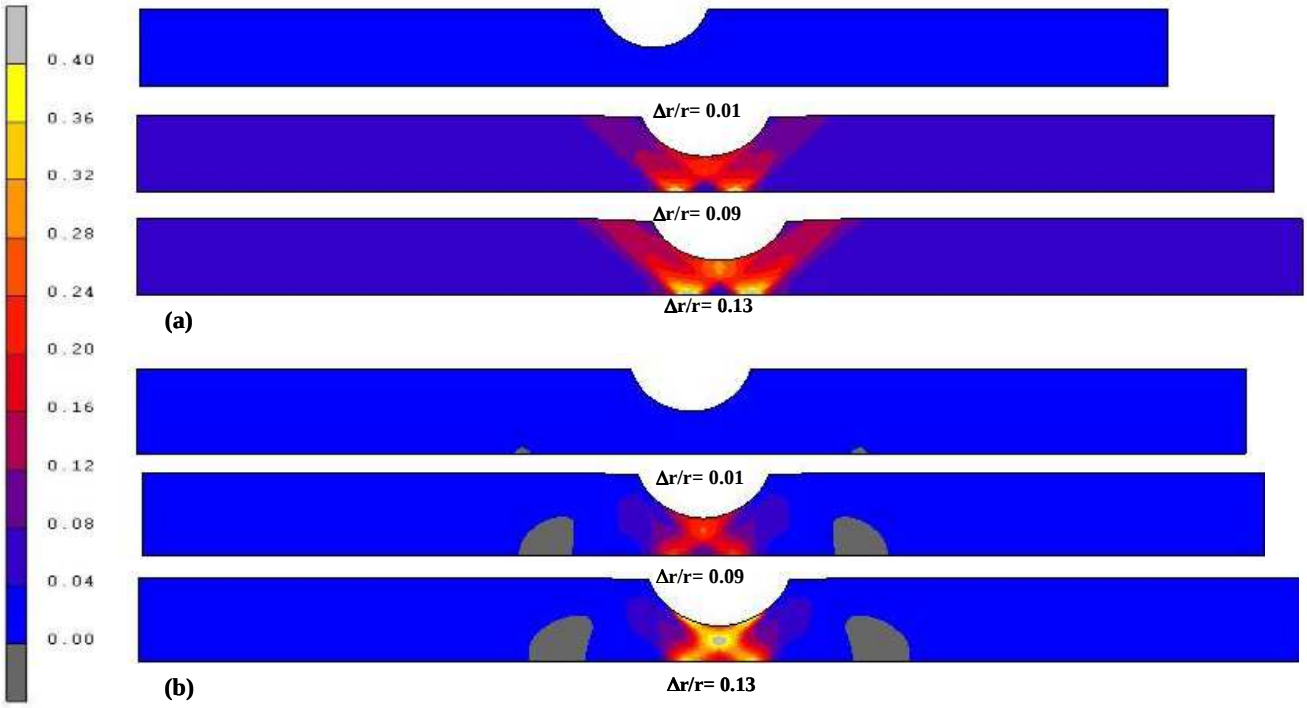

Fig. 3.24. FE axial strain distribution for R4 specimen at different nominal diameter strains ($\Delta r/r_o$): (a) core in ULDPE, (b) core in HDPE.

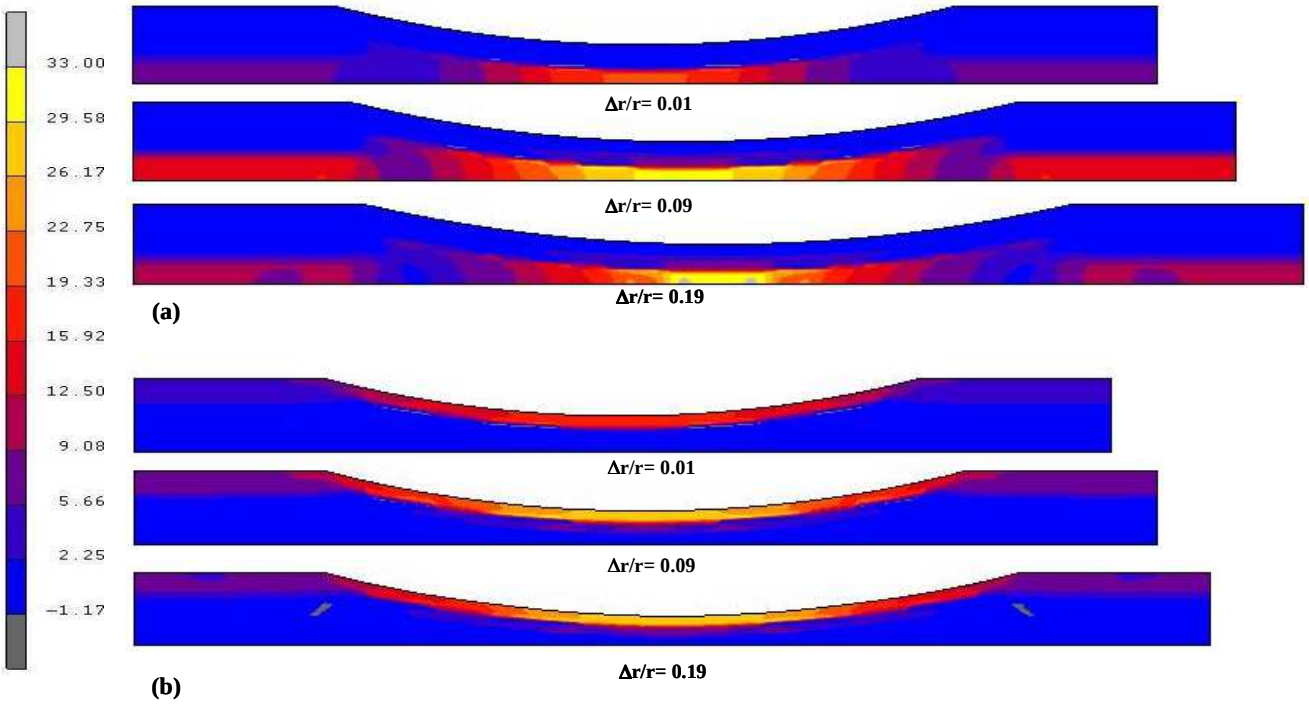

Fig. 3.25. FE axial stress distribution for R80 specimen at different nominal diameter strains ($\Delta r/r_o$): (a) core in ULDPE, (b) core in HDPE.

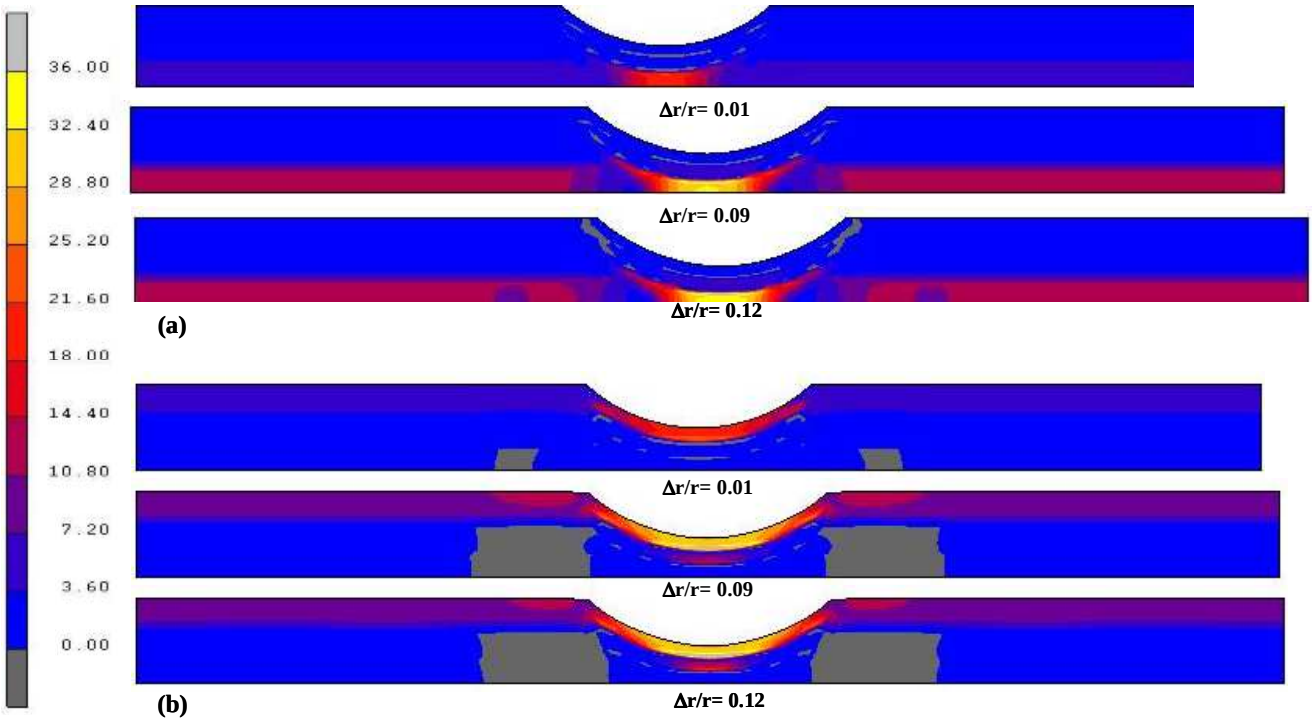

Fig. 3.26. FE axial stress distribution for R10 specimen at different nominal diameter strains ($\Delta r/r_o$): (a) core in ULDPE, (b) core in HDPE.

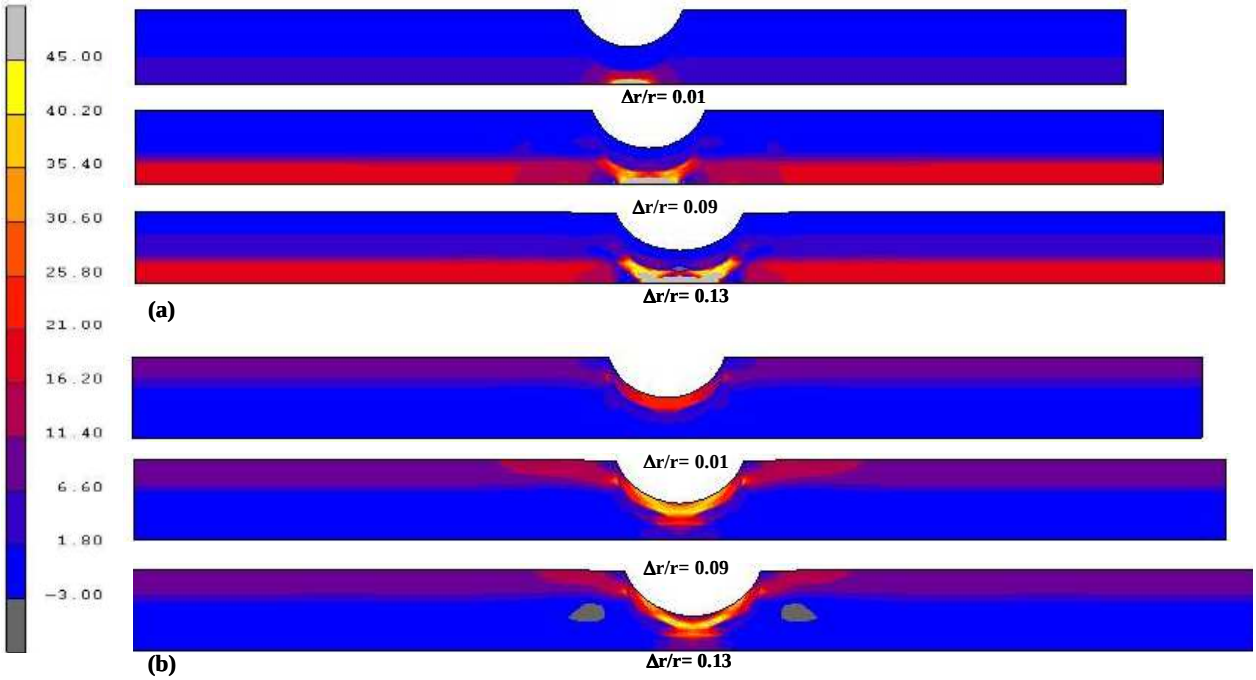

Fig. 3.27. FE axial stress distribution for R4 specimen at different nominal diameter strains ($\Delta r/r_o$): (a) core in ULDPE, (b) core in HDPE.

IV.3.2. Stress triaxiality ratio of notched round specimens

IV.3.2.1. Stress triaxiality ratio at median cross-section

The stress triaxiality ratios for specimens with notch radius R80, R10, and R4 at median cross-section and at nominal diameter strain ($\Delta r/r_o$=0.09) have been examined and presented in **Figs. 3.28-a, 3.28-b, and 3.28-c,** respectively. It can be clearly observed that for all polyethylene materials the stress triaxialty ratio decreases gradually from the centre to the surface. Relatively, higher level of stress triaxiality ratio are observed for higher crystal volume fractions **Figs. 3.28-a, 3.28-b, and 3.28-c** also presents the stress triaxialty ratio for two multi-layered materials with configrations (configuration (a) core in HDPE, and (b) core in ULDPE). It is worth to mention that the stress triaxiality at the middle layer evolving is non-monotonic. The triaxialty ratio attends different levels at the centre of specimens for different curvature radii due to intial triaxiality stress state.

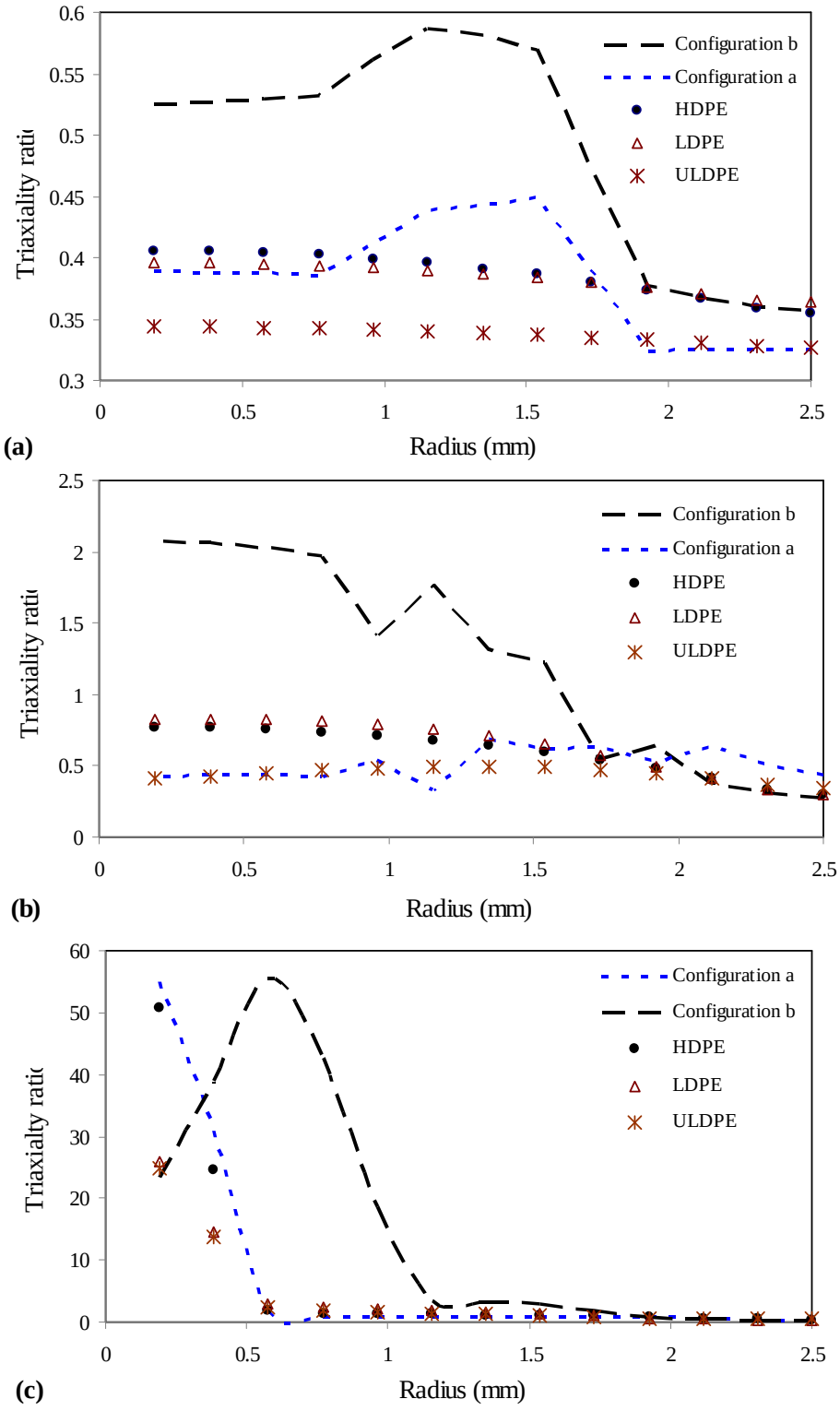

Fig. 3.28. Stress triaxiality ratio distribution along the specimen radius at median cross section and at $\Delta r/r_o$=0.09: (a) R80, (b) R10, (c) R4.

IV.3.2.2. Stress triaxiality ratio distribution for R80 specimen

Fig. 3.29 illustrates the stress triaxiality ratio distribution through the specimens at different nominal diameter strains. The effect of crystal, volume fraction

of polyethylene materials on local stress triaxiality ratio is highlighted. The stress triaxiality distributions are quite irregular; it can be divied into three regions, median cross-section zone, gauge shoulder zone and the zone between gauge shoulder and median cross-section, each region exhibiting similar stress triaxiality distrbution. **Fig. 3.30** exhibits the stress triaxiality distribution for multi-layered materials for both configurations. The stress triaxiality ratio distributions through specimens are more irregular than that observed for polyethylene materials. For configuration a, the negative stress triaxiality arise inside gauge shoulders, while outside the shoulders, high positive stress triaxiality zone appears. The configuration b, exhibit very irregular stress triaxiality especially at the HDPE layer; it may be due to the instable plastic deformation of HDPE.

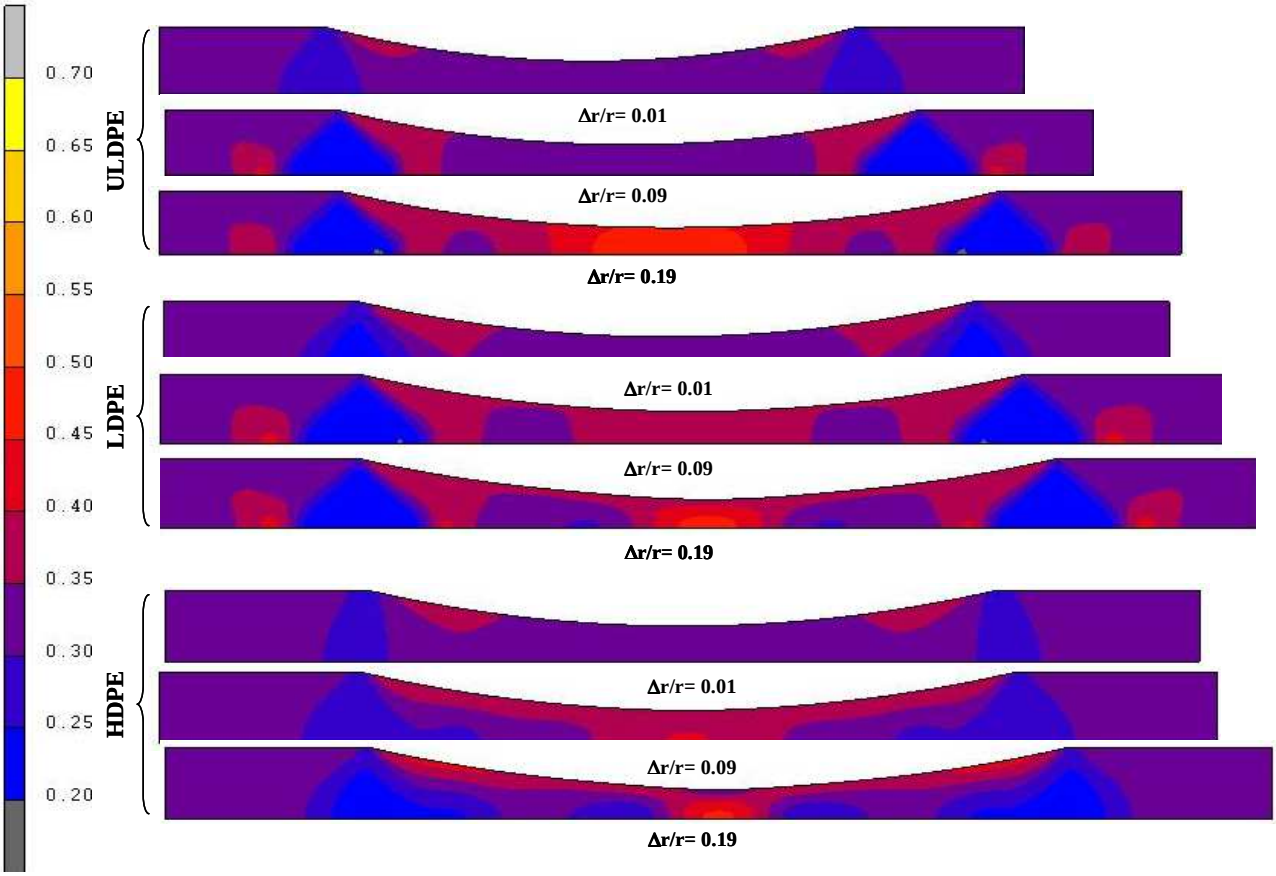

Fig. 3.29. Stress triaxiality ratio distribution through R80 specimen of, for polyethylene materials at different nominal diameter strains ($\Delta r/r_o$).

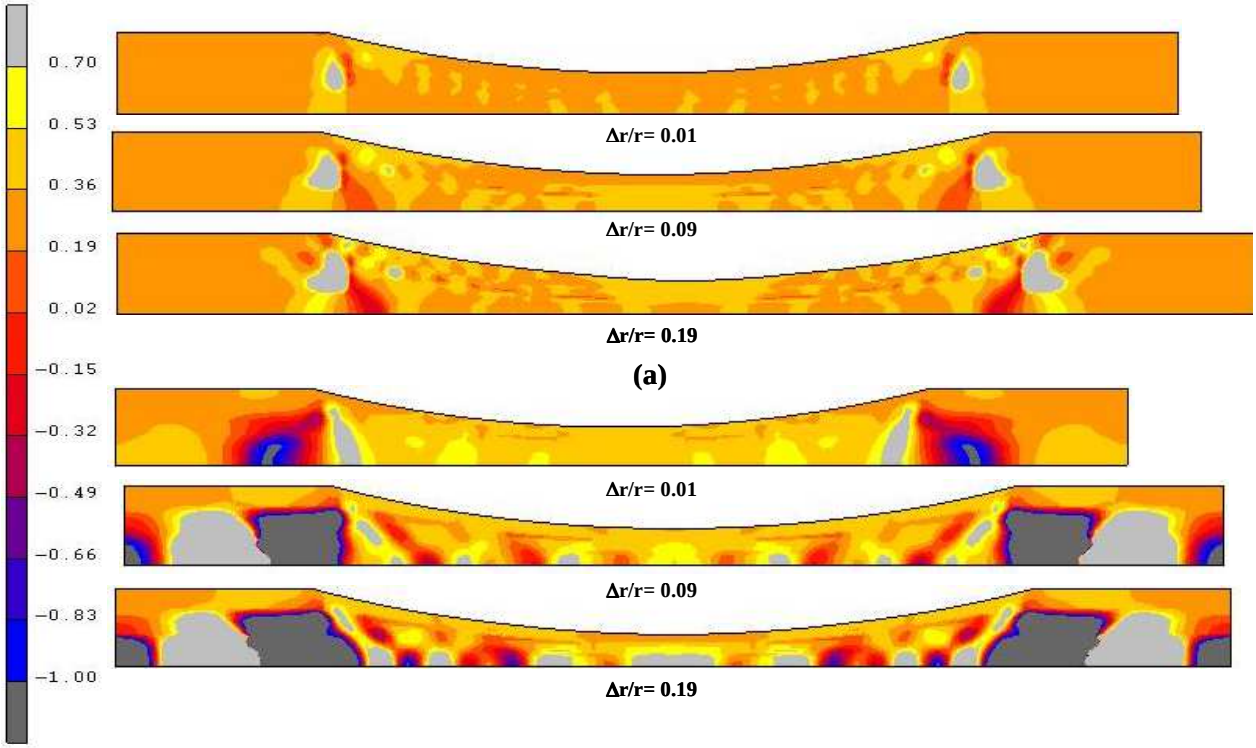

Fig. 3.30. Stress triaxiality ratio distribution through R80 specimens at different nominal diameter strains ($\Delta r/r_o$): (a) core in ULDPE, (b) core in HDPE.

IV.3.2.3. Stress triaxiality ratio distribution for R10 specimen

Fig. 3.31 shows the stress triaxiality ratio distribution through the specimens at different nominal diameter strains for polyethylene materials. The effect of crystal volume fraction is evident on stress triaxiality ratio; high positive stress triaxiality appears near the symetry axis at median cross-section for HDPE and LDPE, whereas for ULDPE, the high positive stress triaxiality emerges in the neighboring zone of median cross-section. However, high positive stress triaxiality arises near the surface at the specimen shoulders.

The stress triaxiality ratio for multi-layered materials is presented in **Fig. 3.32**, which shows different stress triaxiality. The configuration b exhibits more heterogeneous distribution than configuration a.

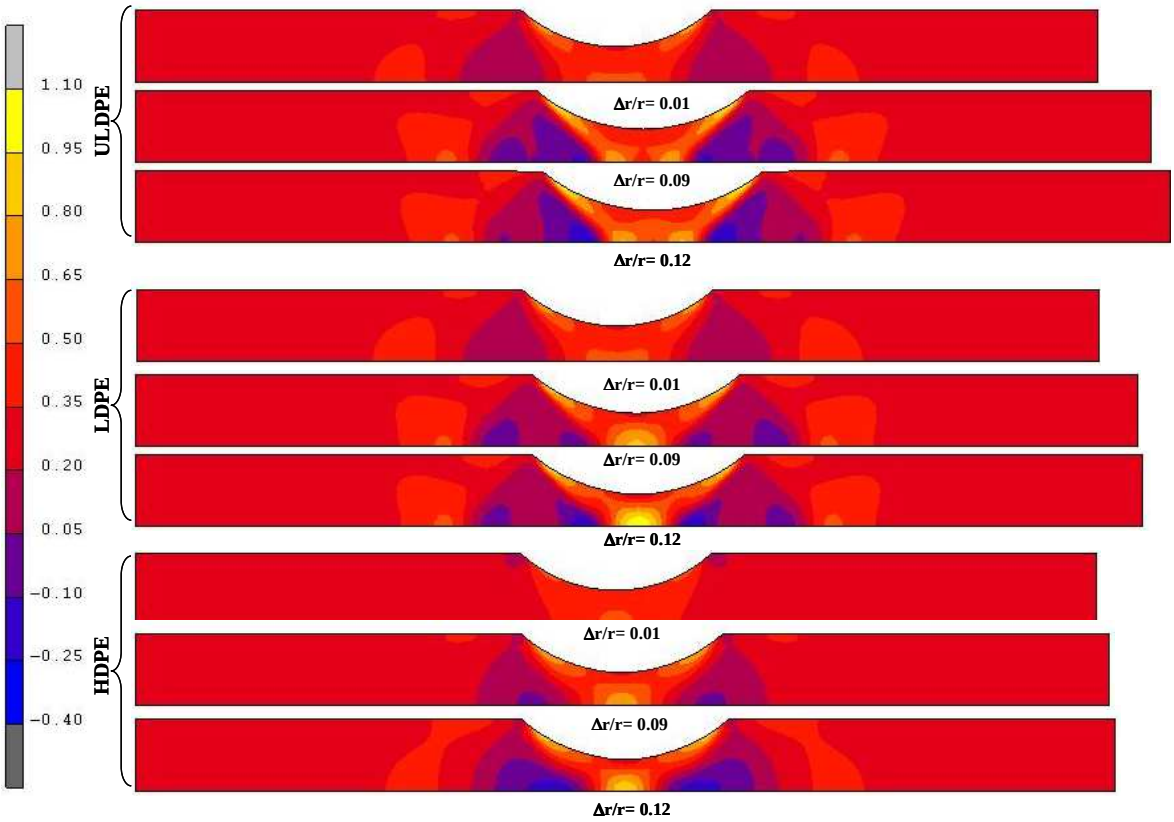

Fig. 3.31. Stress triaxiality ratio distribution through R10 specimen for polyethylene materials at different nominal diameter strains ($\Delta r/r_o$).

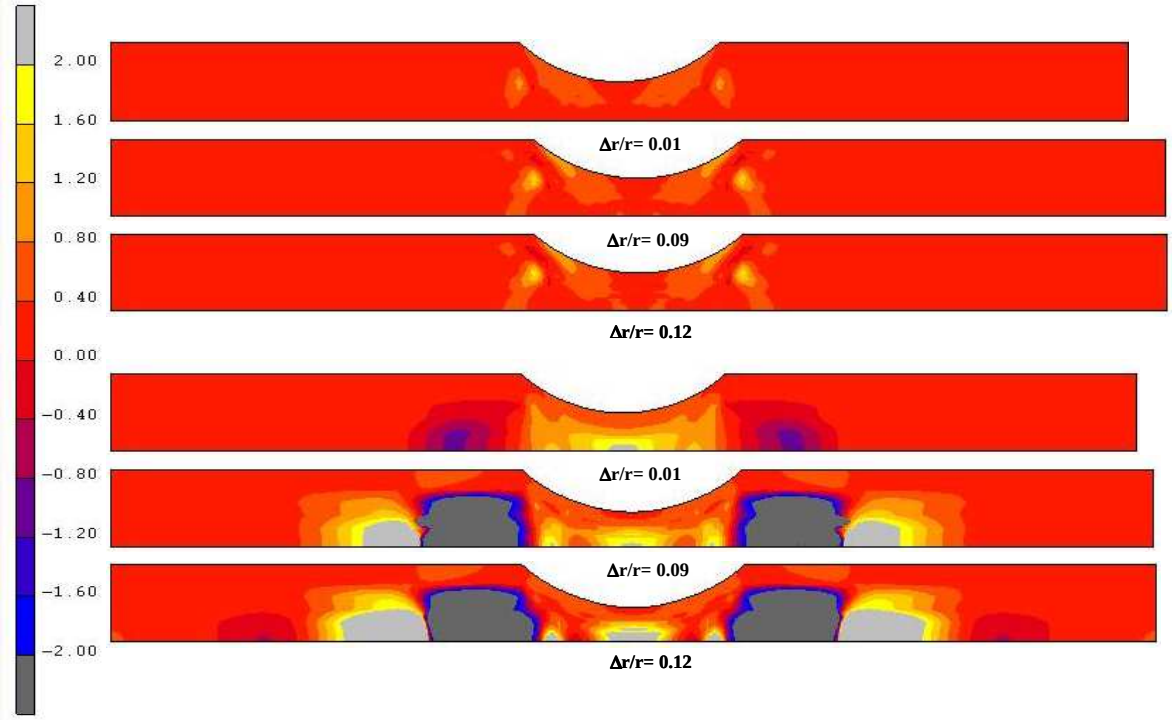

Fig. 3.32. Stress triaxiality ratio distribution through R10 specimen at different nominal diameter strains ($\Delta r/r_o$): (a) core in ULDPE, (b) core in HDPE.

IV.3.2.4. Stress triaxiality ratio distribution for R4 specimen

The stress triaxiality ratio distribution through the R4 specimen for polyethylene materials different nominal diameter strains is shown in **Fig. 3.33** shows. The effect of crystal volume fraction is less obvious due to high level of initial stress triaxiality. The responses are quite similar in terms of stress triaxiality state.

Fig. 3.34 illustrates stress triaxiality ratio distribution for multi-layered materials. Very different response to stress triaxiality can be observed between the two different configurations. These specimens exhibit a more heterogeneous distribution than that observed for R80 and R10 specimens.

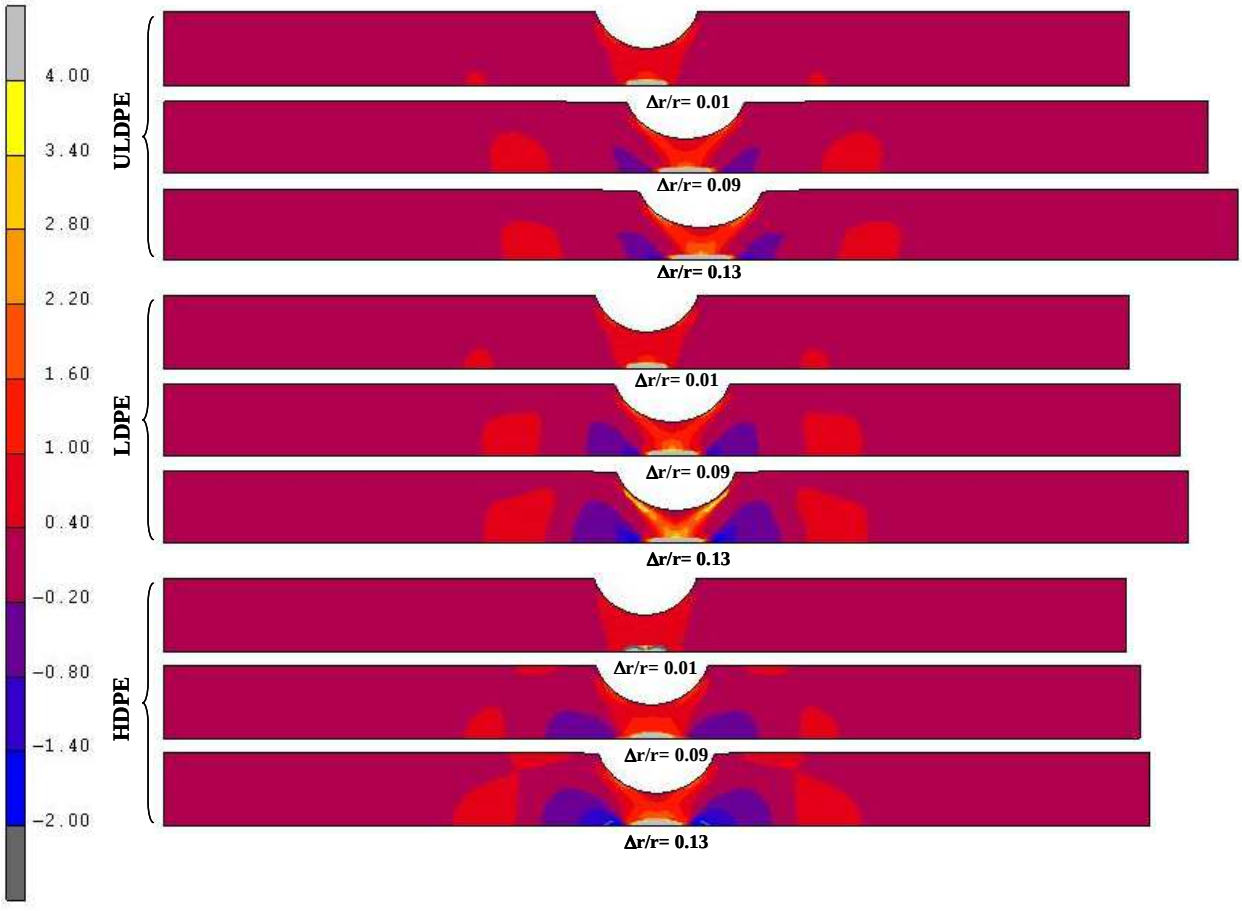

Fig. 3.33. Stress triaxiality ratio distribution through R4 specimens for polyethylene materials at different nominal diameter strain ($\Delta r/r_o$).

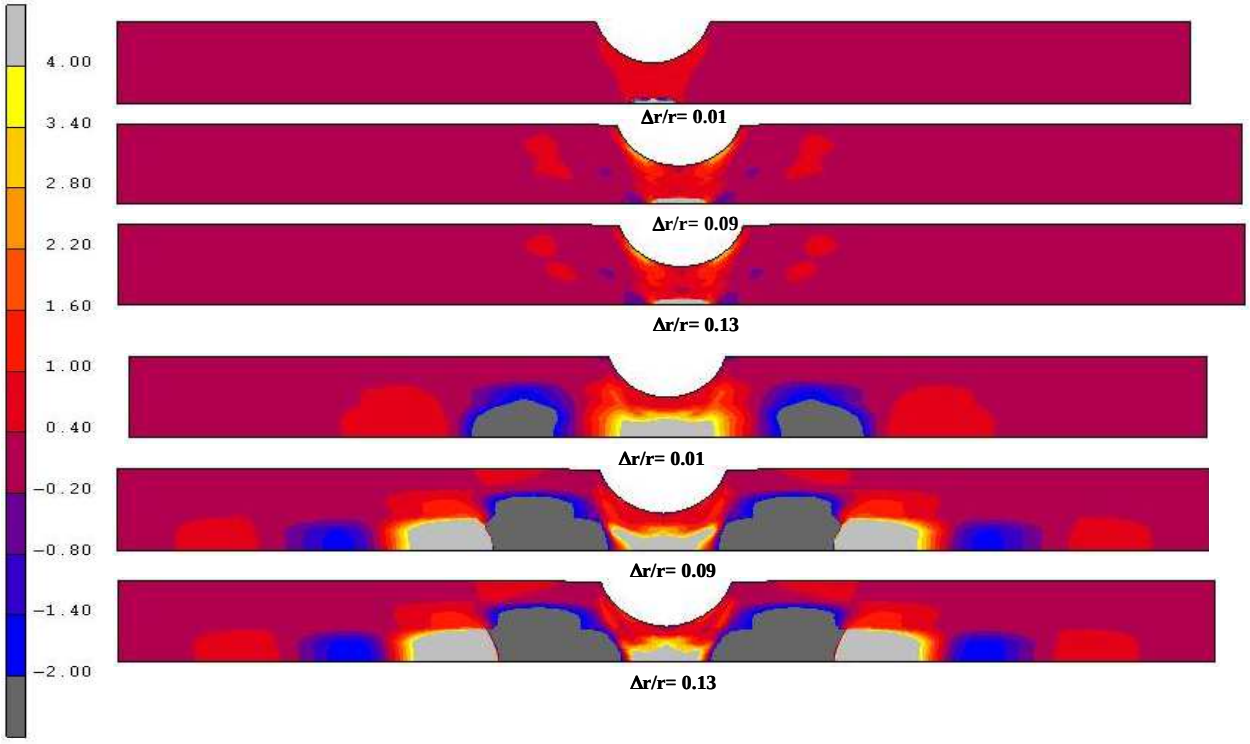

Fig. 3.34. Stress triaxiality ratio distribution maps through R4 specimens at different nominal diameter strains ($\Delta r/r_o$): (a) core in ULDPE, (b) core in HDPE.

IV.4. Partial conclusions

The experimental data and FE simulation results obtained in two previous sections allowed extending this work further, in order to investigate the effect of stress triaxiality ratio in the polyethylene materials (HDPE, LDPE, ULDPE) behavior. Three different notched round bars have been examined with different curvature radii (R80, R10 and R4). The effects of crystal volume fraction and curvature radius are clearly observed on initial stiffness, maximum net stress, nominal diameter strain and stress triaxiality distribution.

Beside polyethylene materials, the multi-layered materials have been also examined. Two different configurations have been investigated; configuration (a), core in with ULDPE/ shell in HDPE and (b) core in HDPE/ shell in ULDPE. It is worth noting that, when changing the configuration, the multi-layered materials behave differently as observed in terms of initial stiffness, yield point, maximum net stress, nominal diameter strain and stress triaxiality distribution.

REFERENCES:

Bao, Y., Wierzbicki, T., 2005. On the cut-off value of negative triaxiality for fracture Engineering Fracture Mechanics. 72, 1049-1069.

Bridgman, P.W., 1944. The stress distribution at the neck of a tension specimen. Transactions ASME. 32, 553-574.

Boyce, M.C., Parks, D.M., Argon, A.S., 1988. Large inelastic deformation of glassy polymers, Part I: rate-dependent constitutive model. Mechanics of Materials. 7, 15-33.

De Souza, Neto, E. A., Peric, D., Owen, D.R.J., 2008. Computational Methods for Plasticity: Theory and Applications, John Wiley and Sons Publication.

Hachour, K., Zaïri, F., Naït-Abdelaziz, M., Gloaguen, J.M., Aberkane, M., Lefebvre, J.M., 2014. Experiments and modeling of high-crystalline polyethylene yielding under different stress states. International Journal of Plasticity. 54, 1-18.

G'Sell, C., Jonas, J.J., 1979. Determination of the plastic behaviour of solid polymers at constant true strain rate. Journal of Materials Science. 14, 583-591.

G'Sell, C., Aly-Helal, N.A., 1983. Effect of stress trixiality on neck propagation during the tensile stretching of solid polymers. Journal of Materials Science. 18, 1731-1742.

G'Sell, C., Hiver, J.M., Dahoun, A., Souahi, A., 1992. Video-controlled tensile testing of polymers and metals beyond the necking point. Journal of Materials Science. 27, 5031-5039.

Fréderix, C., 2009. Etude de mélanges de polyéthléne couvrant une large gamme de taux de cristallinité dans la prespective d'élaboration de matériaux à gradient de propriétés mécaniques.Thesis. Université Lille 1 Sciences et Technologies.

Kwon, H.J., Jar, P.-Y.B., 2008. On the application of FEM to deformation of high-density polyethylene. International Journal of Solids and Structures. 45, 3521-3543.

Neale, K.W., Tugcu, P., 1985. Analysis of necking and neck propagation in polymeric materials. Journal of the Mechanics and Physics of Solids. 33, 323-337.

Smit, R.J.M., 1994. Numerical simulation of localization phenomena in polymer glasses. Report from Faculty of Mechanical Engineering. Eindhoven University of Technology. Report No. WFW 94. 046

Tugcu, P., Neale, K.W., 1987a. Analysis of plane-strain neck propagation in viscoplastic polymeric films. International Journal of Mechanical Sciences. 29, 793-805.

Tugcu, P., Neale, K.W., 1987b. Necking and neck propagation in polymeric materials under plane-strain tension. International Journal of Solids and Structures. 23, 1063-1085.

Tvergaard, V., Needleman, A., Lo, K.K., 1981.Flow localization in the plane strain tensile test. Journal of Mechanics and Physics of Solids. 29, 115-142.

van Melick, H.G.H., Govaert, L.E., Meijer H.E.H., 2003. Localisation phenomena in glassy polymers: influence of thermal and mechanical history. Polymer. 44, 3579-3591

Wu, P.D., van der Giessen, E., 1995. Neck propagation in amorphous glassy polymers under plane strain tension. International Journal of Plasticity. 11, 211-235.

Wu, P.D., van der Giessen, E.,1994. Analysis of shear band propagation in amorphous glassy polymers. International Journal of Solids and Structures. 31, 1493-1517.

General conclusions

This PhD dissertation is a contribution to the study of the polyethylene viscoelastic-viscoplastic response under large deformation. Experimental observations, constitutive modeling and simulations were undertaken.

Experimental observations, reported in chapter one, highlighted the time-dependent mechanical characteristics of polyethylene. The effect of the crystallinity has been quantified on the rate-dependent yield strength and strain hardening, the cyclic stress-softening, the hysteresis, the remaining strain and the stress relaxation.

The large-strain viscoelastic-viscoplastic framework was used, in chapter two, to capture the thermoplastic/elastomeric transition in the polyethylene mechanical response. Two modeling strategies were used. In the first one, the semi-crystalline material was considered as a homogeneous medium, and a set of model parameters were associated at each crystal fraction. In the second one, a two-phase representation of the semi-crystalline material was considered by distinguishing amorphous and crystalline domains, and only one set of model parameters was required. The model parameters were identified by providing two strategies: (i) an analytical deterministic method, proceeding by "step-by-step" parameter analysis; (ii) a numerical identification tool, enabling to directly identify the whole parameter sets following an evolutionary optimization approach. For the two constitutive models, the identified parameter sets obtained led to stress-strain evolutions correctly matching the experimental data. The numerical identification tool developed appears to be a useful, simple and reliable technique. Indeed, the process allowed us to directly obtain the whole parameter sets, in contrast to the

deterministic one, which processes "step-by-step" to determine successively the different parameters. Moreover, the numerical identification approach appears to be predictive: The mechanical response of polyethylene with different crystallinities can be deducted from the parameters identification of only one crystal fraction. An extension of the constitutive model was then proposed in the aim to model the transition from thermoplastic-like to elastomeric-like mechanical response with a minimum of parameters. This improvement also provided insight into the role of crystalline and amorphous phases on macro-behavior of material deformation resistance, i.e. intermolecular and network resistances.

The constitutive model was then implemented into a finite element code. Monolitic specimens in polyethylene were then simulated. The predictions were found in a satisfactory agreement with the experimental observations, both for LDPE and ULDPE, exhibiting homogeneous plastic deformations, and for HDPE, exhibiting an unstable plastic deformation by necking. Bi-layered polyethylene specimens (HDPE stratified with LDPE or with ULDPE) were simulated to examine the model capabilities. The main features, in particular the necking development, were well reproduced by the simulations. The last applications were dedicated to (monolitic and multi-layered) notched round bar specimens, with different curvature radii, in order to predict the stress triaxiality effects on the main characteristics of the local-global mechanical response.

Résumé

Ce travail de thèse est une contribution à l'étude de la réponse mécanique en grandes transformations du polyéthylène.

Dans une première partie, des observations expérimentales sont données sur la réponse mécanique dépendante du temps de polyéthylènes contenant une large gamme de fractions cristallines.

Dans une seconde partie, un modèle de comportement viscoélastique-viscoplastique est développé pour reproduire, lorsque le taux de cristallinité évolue, la transition progressive entre la réponse mécanique typique des thermoplastiques et celle plus typique des élastomères. Afin d'identifier les paramètres du modèle, une méthode déterministe analytique et une méthode numérique, basée sur un algorithme génétique, sont développées.

Dans une troisième partie, le modèle de comportement proposé est implanté dans un code de calculs par éléments finis et utilisé pour prédire la réponse d'échantillons multi-couches de polyéthylènes à différentes fractions cristallines. Des comparaisons entre les simulations et les données expérimentales (en termes de réponse mécanique et d'évolution de la striction) mettent en évidence les capacités prédictives du modèle proposé.

Abstract

This PhD dissertation deals with the large-strain mechanical response of polyethylene.

In a first part, experimental observations are reported on the time-dependent mechanical response of polyethylene materials containing a wide range of crystal fractions.

In a second part, a large-strain viscoelastic-viscoplastic constitutive model is developed to capture the progressive transition from thermoplastic-like to elastomeric-like mechanical response of polyethylene materials, as the crystal content changes. In order to identify the model parameters, an analytical deterministic scheme and a practical, "engineering-like", numerical tool, based on a genetic algorithm are developed.

In a third part, the proposed constitutive model is implemented into a finite element code and used to predict the response of multi-layered polyethylene specimens with different crystal fractions. Comparisons between the simulations and the experimental data (in terms of mechanical response and necking evolution) point out the model predictive capabilities.